

# Femtosecond quantum control studies on vibrational quantum information processing

Caroline Gollub



2008



Dissertation zur Erlangung des Doktorgrades der Fakultät  
für Chemie und Pharmazie der  
Ludwig-Maximilians-Universität München

**Femtosecond quantum control  
studies on vibrational quantum  
information processing**

Caroline Gollub  
aus Mannheim

Dezember 2008

## Erklärung

Diese Dissertation wurde im Sinne von § 13 Abs. 3 der Promotionsordnung vom 29. Januar 1998 von Frau Prof. R. de Vivie-Riedle betreut.

## Ehrenwörtliche Versicherung

Diese Dissertation wurde selbständig, ohne unerlaubte Hilfe erarbeitet.  
München, am 08. Dezember 2008

1. Gutachterin: Prof. Dr. R. de Vivie-Riedle
2. Gutachter: Prof. Dr. J. von Delft

Dissertation eingereicht am 08. Dezember 2008

Mündliche Prüfung am 27. Januar 2009

# Kurzfassung

Diese Dissertation befasst sich mit der Quantenkontrolle von Schwingungsprozessen im Hinblick auf molekulares Quantencomputing. Der Ansatz des Quantencomputing Konzepts basiert auf Schwingungsfreiheitsgraden von polyatomaren Molekülen. Die logischen Werte der Qubits 0 oder 1 werden jeweils durch einen bestimmten Anregungsgrad einer Normalmode kodiert und die logischen Quantenoperationen werden durch speziell geformte, ultrakurze Laserpulse implementiert. Diese Laserfelder lassen sich mit Hilfe der sogenannten Optimalen Kontrolltheorie ermitteln.

Das Konzept des molekularen Quantencomputings, das ursprünglich auf Quantengattern basierte, die einen IR Anregungsprozess im Molekül bewirken, wird im ersten Teil der Dissertation auf Raman aktive Normalmoden übertragen. Daraus ergibt sich der Vorteil, dass nun auch andere Frequenzbereiche, z.B. der Bereich um 800 nm, für die Realisierung der Quantenoperationen im Experiment zur Verfügung steht. Im nahen IR und UV/VIS Bereich existieren schon seit längerer Zeit ausgereifte Techniken des Pulsformens.

Mittels verschiedener ab-initio Untersuchungen konnte das Molekül Butylamin und speziell dessen Raman aktive C-H Streckschwingungen, als ein geeignetes Qubit System zur ersten theoretischen Demonstration dieser Idee, ermittelt werden. Ein universeller Satz von Quantengatter, bestehend aus kurzen und einfach strukturierten Laserpulsen konnte mit sehr hohen Effizienzen optimiert werden. Zur Berechnung der nichtresonanten Laserfelder, die den Schwingungsprozess induzieren, der den logischen Operationen zu Grunde liegt, musste das bisher in der Optimalen Kontrolltheorie verwendete Kontrollfunktional modifiziert werden. Die Erweiterung um Frequenzfilteroperationen erlaubt nun zum ersten Mal die Kontrolle von nichtresonanten Zweifarben-Prozessen und die gleichzeitige Berechnung der beiden an dem Prozess beteiligten Laserfelder. Dieses neu entwickelte, kontrolltheoretische Verfahren stellt eine universelle Methode dar und lässt sich leicht auf verschiedene Prozesse

---

übertragen in denen entsprechende Filteroperationen hilfreich oder sogar essentiell sind.

Nachdem gegenwärtig die ersten erfolgreichen Demonstrationen von geformten, ultrakurzen Laserpulsen auch im mittleren IR Bereich vorgestellt werden, ist es interessant die Übereinstimmung der jeweilig gefundenen Ergebnisse von theoretischen und experimentellen Kontrollstudien zu vergleichen. Die experimentelle Herangehensweise basiert auf Optimierungen mit Rückkopplungsschleifen, deren zentrale Elemente ein evolutionärer Algorithmus, ein Pulsformer und ein Rückkopplungssignal, das auf die Effizienz des Prozesses schließen lässt, sind. Die experimentellen Ergebnisse für die optimalen Laserpulse können sehr komplex und auch ungünstigerweise sehr lang ausfallen. In der vorliegenden Arbeit wurden verschiedene Strategien entwickelt um dies zu umgehen. Untersucht wurden in diesem Zusammenhang zwei verschiedene Ansätze der Phasenmodulation, eine Einschränkung der Variationsbreite der Phase, sowie die spektrale Breite der Eingangspulse. Als Ergebnis konnte gezeigt werden, dass eine parametrisierte, sinusförmige Phasenmodulation, die oft im Experiment Verwendung findet um die Komplexität der Felder zu reduzieren, zu unflexibel ist für eine effiziente Implementierung von Quantengattern. Dagegen bieten sich gepixelte Maskenfunktionen in Kombination mit einer geeigneten Wahl der Eingangspuls- und Optimierungsparameter an.

Alternativ zu dem bisher verwendeten evolutionären Algorithmus wurden neue Optimierungsmethoden vorgeschlagen, die auf einem "multi-objective" genetischen Algorithmus und einem natürlichen Algorithmus, dem sogenannten Ameisenalgorithmus, beruhen. Diese Methoden führen leicht zu den gewünschten Ergebnissen, ohne Verlust der hohen Quanteneffizienz und lassen sich direkt auf die experimentelle Herangehensweise übertragen. Diese Studien erlauben eine Optimierung direkt im Suchraum des Experiments und lassen von daher verlässliche Vorhersagen zu, bei denen alle experimentellen Rahmenbedingungen konsequent eingehalten werden können. Aussagen zur experimentell maximal erreichbaren Effizienz mit den zur Verfügung stehenden Eingangspulsen können getroffen werden, aber auch eine Benennung der geeignetsten Startbedingungen wird möglich.

Zusätzlich wurden Quantenkontrollstudien von Schwingungsprozessen in offenen Systemen durchgeführt, d.h. dissipative Effekte wurden direkt in die theoretischen Untersuchungen miteinbezogen. Aus den Resultaten lässt sich ableiten, dass möglichst kurze Pulsdauern essentiell für hohe Quantenausbeuten

---

sind und genau dies lässt sich mit den in der Dissertation entwickelten und vorgestellten Kontrollverfahren erreichen.

Einen Schritt über einzelne Qubit Systeme hinaus, wurde durch die Konstruktion eines ersten, kleinen Quantennetzwerkes gemacht. Hierbei wurden zwei molekulare Qubit Einheiten durch eine lineare Molekülkette miteinander verknüpft. Diese Idee stellt ein erstes Konzept in Richtung der Skalierbarkeit des Quantencomputing Ansatzes dar. Ein Modellsystem wurde aufgesetzt und ein Laser-getriebener Schwingungsenergie transfer über das Kettenmolekül von der einen Qubit Seite auf die andere Seite optimiert. Dies lässt sich als eine Kommunikation zwischen benachbarten Qubit Einheiten verstehen und könnte so zur Konstruktion von Quantenregistern oder einer entsprechenden Wechselwirkung mit molekularen Speichereinheiten führen.



# Publications

- B. F. Straub and C. Gollub  
*Mechanism of Reppe's Nickel-Catalyzed Ethyne Tetramerization to Cyclooctatetraene: A DFT Study*  
Chem. Eur. J. **10** (2004) 3081-3090.
- C. Gollub, U. Troppmann and R. de Vivie-Riedle  
*The role of anharmonicity and coupling in quantum computing based on vibrational qubits*  
New J. Phys. **8** (2006) 48.
- U. Troppmann, C. Gollub and R. de Vivie-Riedle  
*The role of phases and their interplay in molecular vibrational quantum computing with multiple qubits*  
New J. Phys. **8** (2006) 100.
- C. Gollub, B. M. R. Korff, K. L. Kompa and R. de Vivie-Riedle  
*Chirp-driven vibrational distribution in transition metal carbonyl complexes*  
Phys. Chem. Chem. Phys. **9** (2007) 369-376.
- B. M. R. Schneider, C. Gollub, K. L. Kompa and R. de Vivie-Riedle  
*Robustness of quantum gates operating on the high frequency modes of  $MnBr(CO)_5$*   
Chem. Phys. **338** (2007) 291-298 .
- C. Gollub and R. de Vivie-Riedle  
*Comment on "Anharmonic properties of the vibrational quantum computer" [J. Chem. Phys. 126, 204102 (2007)]*  
J. Chem. Phys. **128** (2008) 167101.

- 
- C. Gollub, M. Kowalewski and R. de Vivie-Riedle  
*Monotonic convergent optimal control theory with strict limitations on the spectrum of optimized laser fields*  
Phys. Rev. Lett. **101** (2008) 073002.
  - C. Gollub and R. de Vivie-Riedle  
*Theoretical optimization and prediction in the experimental search space for vibrational quantum processes*  
Phys. Rev. A **78** (2008) 033424.
  - C. Gollub and R. de Vivie-Riedle  
*Multi-objective genetic algorithm optimization of 2D- and 3D-Pareto fronts for vibrational quantum processes*  
New J. Phys. (2008), accepted.
  - C. Gollub and R. de Vivie-Riedle  
*A modified Ant Colony Optimization algorithm as an alternative to genetic algorithms*  
submitted.

in preparation:

- C. Gollub and R. de Vivie-Riedle  
*Dissipative effects on vibrational quantum gate operations*
- C. Gollub and R. de Vivie-Riedle  
*Quantum networks and information transfer through molecular chains*
- D. B. Strasfeld, C. Gollub, M. T. Zanni and R. de Vivie-Riedle  
invited paper, New J. Phys. (2009)

# List of abbreviations

ACO	ant colony optimization
CEP	carrier-envelope phase
DFT	density functional theory
el	electronic
FIR	finite impulse response
FL	Fourier-limited
FROG	frequency resolved optical gating
FWHM	full width at half maximum
GA	genetic algorithm
HF	Hartree-Fock
IR	infrared
IVR	intramolecular vibrational redistribution
MOGA	multi-objective genetic algorithm
mol	molecular
MTOCT	multi-target optimal control theory
NMR	nuclear magnetic resonance
NSGA-II	elitist non-dominated sorting genetic algorithm II
nuc	nuclear
OCT	optimal control theory
OCE	optimal control experiments
QFT	quantum Fourier transform
qubit	quantum bit
SLM	spatial light modulator
SPIDER	spectral phase interferometry for direct electric field reconstruction
SPO	split operator
UV/VIS	ultraviolet/visible



# Contents

<b>Introduction</b>	<b>1</b>
<b>1 Fundamentals of quantum dynamics, information and control</b>	<b>5</b>
1.1 Quantum dynamics . . . . .	5
1.1.1 Schrödinger equation . . . . .	6
1.1.2 Propagation . . . . .	8
1.1.3 Eigenfunctions . . . . .	10
1.1.4 Dissipative dynamics . . . . .	10
1.2 Quantum computing . . . . .	13
1.2.1 Universal quantum computing . . . . .	14
1.2.2 Implementation of quantum information processing . . . . .	16
1.2.3 Molecular quantum computing . . . . .	16
1.3 Quantum control . . . . .	17
1.3.1 Ultrashort laser pulses . . . . .	18
1.3.2 Coherent control with genetic algorithms . . . . .	21
1.3.3 Optimal control theory . . . . .	24
<b>2 Molecular quantum computing based on the stimulated, non-resonant Raman effect</b>	<b>29</b>
2.1 Stimulated, non-resonant Raman quantum computing . . . . .	29
2.2 MTOCT with frequency filters . . . . .	32
2.3 Molecular candidate and Raman quantum gates . . . . .	38
2.4 Application prospects of bandwidth-limited OCT . . . . .	41
2.5 Conclusion . . . . .	42
<b>3 Control of vibrational quantum processes with genetic algorithms</b>	<b>45</b>
3.1 Model systems and computational details . . . . .	46
3.2 Results and discussion . . . . .	50
3.2.1 NOT gate: $T_{1u}$ mode of $W(\text{CO})_6$ . . . . .	50

3.2.2	Objective with a cost function . . . . .	52
3.2.3	Phase modulation in analytic form . . . . .	54
3.2.4	Prediction of quantum gates for $\text{MnBr}(\text{CO})_5$ . . . . .	63
3.3	Conclusion . . . . .	67
<b>4</b>	<b>Optimization with multi-objective genetic algorithms</b>	<b>69</b>
4.1	Multi-objective genetic algorithm and application . . . . .	70
4.2	Results and discussion . . . . .	72
4.2.1	2D Pareto fronts for state-to-state transitions . . . . .	72
4.2.2	3D Pareto front for a unitary transformation . . . . .	82
4.3	Conclusion . . . . .	85
<b>5</b>	<b>Laser field optimization with a modified ant colony algorithm</b>	<b>87</b>
5.1	Basics of ACO . . . . .	88
5.2	ACO application to quantum control . . . . .	90
5.3	Conclusion . . . . .	98
<b>6</b>	<b>Vibrational quantum gates under the influence of dissipation</b>	<b>101</b>
6.1	Optimization under the influence of dissipation . . . . .	101
6.1.1	Optimization with OCT . . . . .	101
6.1.2	Optimization with genetic algorithms . . . . .	103
6.2	Results and discussion . . . . .	104
6.2.1	Robustness of quantum gates against dissipation . . . . .	105
6.2.2	Quantum gate optimization in a dissipative environment	110
6.2.3	Precompiled quantum computing . . . . .	115
6.3	Conclusion . . . . .	118
<b>7</b>	<b>Molecular chains for vibrational quantum information processing</b>	<b>119</b>
7.1	Approach for quantum information processing with vibrational qubits . . . . .	120
7.2	State transfer and quantum channels . . . . .	124
7.3	Investigation of dissipative influence . . . . .	131
7.4	Conclusion . . . . .	132
	<b>Summary</b>	<b>135</b>
	<b>Bibliography</b>	<b>139</b>

# Introduction

As femtosecond laser pulses are a key technology of this century, their usage makes advances to new application fields. Recent practical implementations of ultrashort pulses can be found in information and life science or in industrial fabrication, e.g. in high-precision micro-machining.

The ultrafast pulses operate on time scales, in which molecular vibrations and chemical reactions occur, and they also represent a tool for time-resolved observations of quantum dynamical processes in molecules. In 1999, the Nobel Prize in chemistry was awarded to A. Zewail for his pioneering work on the analysis of transition states in chemical reactions with the help of femtosecond laser spectroscopy [1, 2]. At the same time, the first ideas on the usage of such ultrafast events for the control of molecular quantum dynamics emerged. The goal is to employ the coherent laser light for the control of quantum phenomena in atoms and molecules in a desired way [3]. The ultrashort laser source can be used for the coherent manipulation of laser-induced wave packet dynamics. The electric laser fields, which couple to the quantum systems, have to be modulated appropriately by shaping the phase and the amplitude of the incident laser pulses to gain the desired control over the quantum processes. R. S. Judson and H. Rabitz proposed the idea of quantum control experiments based on a closed loop setup [4]. The structures of the laser fields are optimized with the help of evolutionary algorithms, which allow for adaptive improvements of the efficiency related to the desired quantum processes. Feedback signals determining the quantum yields of the experimental outcome are necessary for the adaptive setup.

In theory, a similar technique has been proposed based on optimal control theory [5, 6]. Instead of the experimental feedback signal, here the explicit knowledge of the Hamiltonian is required. The strategy proved to be a successful tool in many theoretical studies as it allows for the identification of possible control mechanisms and pathways as well as for the theoretical demonstration of new application possibilities. Quantum control theory plays a central role for

the prediction of laser field shapes for the experiment and for assessing their experimental outcomes.

Many applications of coherent control with shaped femtosecond laser pulses have been presented so far in theory and experiment, where the fields of research reach from biology to chemistry and physics. An application, which requires precise control of quantum systems is quantum information processing. Particularly, when the quantum computing scheme is based on molecular degrees of freedoms, these sophisticated control strategies are essential. A molecular quantum computing concept has been proposed [7], where the quantum bits (qubits) are coded by vibrational eigenstates of IR active normal modes. In this scheme, the quantum logic operations are implemented by specially shaped, electric laser fields in the mid-IR regime, and they are optimized with optimal control theory.

The focus of this thesis is on quantum control strategies in the context of molecular quantum computing with vibrational qubits. The concept is transferred to the 800 nm regime, by using Raman active modes for the coding of the qubit states. The laser source in this frequency regime is easily accessible and pulse shaping techniques are well established. For the calculation of the Raman quantum gates, new modifications of the optimal control theory functional have to be developed.

Additionally, the experimental control strategies based on closed loop techniques from the experiment will be adapted to theory. This will allow for an insight into the differences, which arise from quantum control performed in the time domain with optimal control theory and in the frequency domain with evolutionary algorithms. The experimental search spaces can be investigated and predictions of new search strategies in the experiment will become possible. Routes towards preferably simple, robust and short laser pulse solutions, driving the desired quantum processes, can be revealed.

New control algorithms are developed and explored in the context of molecular quantum computing, but the advantages of their application will also be transferrable to a large variety of control tasks in different research areas. The theoretical results will benefit related control experiments and they demonstrate the decisive role of theory in coherent control. Vibrational relaxation effects are incorporated in the quantum gate calculations to allow for the most precise simulation of future experiments and for reliable predictions.

A first approach towards the scalability of the molecular quantum computing concept is investigated and will be presented in the last part of the thesis based

---

on the connection of the vibrational qubit systems with linear chain molecules. Across the molecular bridges, a laser-driven vibrational energy transfer is optimized, which facilitates the communication between individual qubit systems.



# 1 Fundamentals of quantum dynamics, information and control

The control prospects of vibrational quantum processes, such as state-to-state transitions, unitary transformations and vibrational energy transfer through molecular chains are investigated in this thesis. In all cases, the driving forces are external, electric laser fields inducing the wave packet dynamics. The fundamental tool for the description and simulation of these processes is the solution of the time-dependent Schrödinger equation. The basic quantum dynamical considerations with respect to the Schrödinger equation, numerical propagation methods, the evaluation of eigenfunctions and the description of dissipative effects will be introduced. Additionally, an overview of the idea of quantum computers, quantum information processing and in particular on the concept of molecular quantum computing with vibrational qubits will be given. Besides the pure detection of quantum processes, also experimental and theoretical efforts are made to control these processes in an optimal way. The fundamental control concepts in theory, optimal control theory (OCT) and in experiment, closed loop techniques are introduced and the basics of ultrashort laser pulses are presented.

## 1.1 Quantum dynamics

Quantum processes can be studied by solving the time-dependent Schrödinger equation, where usually numerical propagation schemes are applied. The calculations can be performed, based either on a grid or on an eigenstate representation. For the latter case, the eigenfunctions and eigenvalues have to be known and their evaluation will be briefly addressed. Both approaches differ in the choice of the basis functions and can easily be transferred into each other.

Generally, a quantum system cannot be regarded as completely isolated and different intra- and intermolecular effects may play a role in the dynamics. For the investigation of induced dissipative effects, the wave function description is transferred to the density matrix representation, where effects such as energy relaxation can be incorporated in the quantum dynamical calculation. The fundamental considerations of the density matrix formalism and the corresponding propagation schemes are presented.

### 1.1.1 Schrödinger equation

The quantum dynamics of a molecular system with the Hamiltonian  $\hat{H}_{\text{mol}}$  is governed by the time-dependent Schrödinger equation:

$$i \frac{\partial}{\partial t} \Psi_{\text{mol}}(t) = \hat{H}_{\text{mol}} \Psi_{\text{mol}}(t), \quad (1.1)$$

(all equations are given in atomic units [au]). The stationary, molecular wave function  $\Psi_{\text{mol}}$  depends on the nuclear coordinates  $R$  and on the electronic coordinates  $r$ . It can be separated according to:

$$\Psi_{\text{mol}}(R, r) = \Psi_{\text{nuc}}(R) \Psi_{\text{el}}(r; R), \quad (1.2)$$

into a nuclear wave function  $\Psi_{\text{nuc}}(R)$ , depending on the nuclei coordinates  $R$  only, and an electronic part  $\Psi_{\text{el}}(r; R)$ , with a parametric dependence on the nuclear arrangement. For the quantum dynamical calculations, the treatment of the electrons and nuclei can be separated, according to the Born-Oppenheimer approximation, due to dynamical time scales, differing by magnitude.

The molecular Schrödinger equation Eq. 1.1 can be separated, since the influence of the nuclear, kinetic operator on the electronic wave function is negligible in the investigated cases. The stationary, electronic Schrödinger equation with the electronic Hamiltonian  $\hat{H}_{\text{el}}$  is obtained:

$$\hat{H}_{\text{el}} \Psi_{\text{el}}(r; R) = E_{\text{el}}(R) \Psi_{\text{el}}(r; R). \quad (1.3)$$

The electronic Hamiltonian includes the kinetic energy operator  $\hat{T}_{\text{el}}$ , the electron-electron interaction operator  $\hat{V}_{\text{el,el}}$ , the interaction operator with the nuclei  $\hat{V}_{\text{el,nuc}}$  and the nuclei-nuclei interaction part  $\hat{V}_{\text{nuc,nuc}}$ :

$$\hat{H}_{\text{el}} = \hat{T}_{\text{el}} + \hat{V}_{\text{el,el}} + \hat{V}_{\text{el,nuc}} + \hat{V}_{\text{nuc,nuc}}. \quad (1.4)$$

The solution of Eq. 1.3 for different molecular arrangements leads to potential energy curves  $E_{\text{el}}(R)$  or potential energy surfaces  $E_{\text{el}}(R_i)$ , in higher dimensional cases, and is commonly performed with ab-initio quantum chemical methods.

The fundamental quantum chemical approach is Hartree-Fock (HF) theory based on a mean field approximation of the electrons. Post-HF methods, such as perturbation theory and configuration interaction methods, were developed to improve the description of the averaged electronic correlation of the HF theory. A comprehensive review on quantum chemistry can be found in [8]. A different approach is pursued in case of density functional theory (DFT) [9], where the many-body electronic wave function is replaced by the electronic density as the basic quantity. The fundamental principles are the Hohenberg-Kohn theorems, stating that the ground state density minimizes the total energy of the system and can be used to calculate the molecular ground state properties. Throughout this thesis, DFT is applied for the quantum chemical calculation of the potential energy surfaces  $E(R_i)$  and the corresponding molecular properties.

The intramolecular motion of the nuclei is described by the quantum dynamics of the nuclear wave function  $\Psi_{\text{nuc}}(R)$  on the calculated potential energy surfaces  $E(R_i) \equiv \hat{V}_{\text{nuc}}$ . As from now, the label  $_{\text{nuc}}$  is omitted for the nuclear wave function  $\Psi_{\text{nuc}}$ , and it will be denoted by  $\Psi$ . In case of the Hamiltonian, the label  $_0$  indicates that it is time-independent. The time evolution of the nuclear wavefunction  $\Psi$  is governed by the time-dependent, nuclear Schrödinger equation:

$$i \frac{\partial}{\partial t} \Psi(t) = \hat{H}_0 \Psi(t). \quad (1.5)$$

The nuclear, time-independent Hamiltonian  $\hat{H}_0$  includes the kinetic energy  $\hat{T}_{\text{nuc}}$  of the nuclei and the potential energy  $\hat{V}_{\text{nuc}}$ . Integrating the time-dependent, nuclear Schrödinger equation (Eq. 1.5) determines the equations of motion as the action of the propagator  $\hat{U}(t)$  on the nuclear wave function:

$$\Psi(t) = \hat{U}(t, t_0) \Psi(t_0) = e^{-i\hat{H}_0(t-t_0)} \Psi(t_0), \quad (1.6)$$

where the propagator of the time-independent Hamiltonian  $\hat{H}_0$  is  $\hat{U}(t, t_0)$ . The nuclear wave function evolves in the time interval  $\Delta t = t_j - t_i$  according to:

$$\Psi(t_j) = e^{-i\hat{H}_0 \Delta t} \Psi(t_i). \quad (1.7)$$

An additional, time-dependent perturbation of the Hamiltonian, might be due to an external, electric field  $\varepsilon(t)$ , interacting with the molecular system (Eq. 1.8).

The interaction is mediated by the molecular dipole moment  $\mu$  (the corresponding operator is  $\hat{\mu}$ ).

$$\hat{H}(t) = \hat{H}_0 - \hat{\mu}\varepsilon(t) \quad (1.8)$$

In this case, the Hamiltonian  $\hat{H}(t)$  is time-dependent and the propagation has to be performed in sufficiently small time steps, so the perturbation can be regarded as constant during the time interval  $\Delta t = t_j - t_i$ . The corresponding propagation equation is given by:

$$\Psi(t_j) = e^{-i(\hat{H}_0 - \hat{\mu}\varepsilon(t_i))\Delta t} \Psi(t_i). \quad (1.9)$$

### 1.1.2 Propagation

The wave function in the quantum dynamical calculations can either be formulated by a grid based method, e.g. in the discrete variable representation [10] or can be represented in the eigenstate basis. In all dynamical calculations of this thesis, the latter case is applied. The basis vectors correspond to the vibrational eigenfunctions  $\Psi_n$ . The wave function is represented by a  $n$ -dimensional vector  $\mathbf{c}(t)$  with the complex, time-dependent elements  $c_n(t)$ , derived from the projection:

$$c_n(t) = \langle \Psi_n | \Psi(t) \rangle. \quad (1.10)$$

The matrix representation  $\mathbf{H}_0$  of the time-independent Hamiltonian  $\hat{H}_0$  is diagonal, where the elements  $H_{0(nn)}$  are given by the eigenenergies  $E_n$ .

$$H_{0(nn)} = \langle \Psi_n(R) | \hat{H}_0(R) | \Psi_n(R) \rangle = E_n, \quad H_{0(nm)} = 0 \quad (1.11)$$

For the laser-molecule interaction, the dipole matrix elements  $\mu_{nm}$  of the matrix  $\boldsymbol{\mu}$  have to be evaluated according to:

$$\mu_{nm} = \langle \Psi_n(R) | \hat{\mu}(R) | \Psi_m(R) \rangle. \quad (1.12)$$

The temporal evolution of the wave function in the eigenstate representation is formally determined by:

$$\mathbf{c}(t_j) = e^{-i(\mathbf{H}_0 - \boldsymbol{\mu}\varepsilon(t_i))\Delta t} \mathbf{c}(t_i) = e^{-i(\mathbf{H}\Delta t)} \mathbf{c}(t_i) = \mathbf{U}(\Delta t) \mathbf{c}(t_i). \quad (1.13)$$

Different numerical approaches can be used to evaluate the propagation steps, given by the exponential equation (Eq. 1.13). Detailed reviews on quantum dynamical methods are presented in [11] and [12].

The numerical evaluation of the term  $e^{-i\mathbf{H}\Delta t} \Psi$  can be performed efficiently with different techniques, where particularly the split operator (SPO) method and the Chebychev polynomial expansion are applied and summarized briefly. If an external laser source couples to the molecular system, the Hamiltonian matrix is non-diagonal due to the transition dipole matrix elements  $\mu_{nm}$ . To evaluate a propagation step, the dipole operator matrix  $\boldsymbol{\mu}$  is diagonalized ( $\boldsymbol{\mu}^{\text{diag}}$ ) and the corresponding transformation matrices  $\mathbf{X}$  and  $\mathbf{X}^\dagger$  are used to change to the diagonal representation and back. A second order SPO propagation step is performed as follows:

$$\mathbf{c}(t_j) = e^{-i\mathbf{H}_0 \frac{\Delta t}{2}} \mathbf{X}^\dagger e^{i\boldsymbol{\mu}^{\text{diag}} \varepsilon(t_i) \Delta t} \mathbf{X} e^{-i\mathbf{H}_0 \frac{\Delta t}{2}} \mathbf{c}(t_i). \quad (1.14)$$

The propagator  $\mathbf{U}(\Delta t)$  (Eq. 1.13) is approximated here by a product of exponential functions of the Hamiltonian ( $\mathbf{H}_0$ ) and laser-molecule interaction ( $\boldsymbol{\mu}\varepsilon(t)$ ) part. Other propagation schemes are based on polynomial expansions of the time evolution operator, such as the Chebychev propagator. Here, the propagator  $\mathbf{U}(\Delta t)$  (Eq. 1.13) is approached by a Chebychev series, taking the form:

$$e^{-i\mathbf{H}t} \equiv \sum_{n=0}^N a_n(t) \Phi_n(-i\mathbf{H}), \quad (1.15)$$

where:

$$a_n(t) = 2J_n(t) \text{ and } a_0(t) = J_0(t). \quad (1.16)$$

$\Phi_n$  are complex Chebychev polynomials, depending on the Hamiltonian and obeying the recursion relation:

$$\Phi_{n+1} = -2i\mathbf{H}\Phi_n + \Phi_{n-1}. \quad (1.17)$$

The time-dependent expansion coefficients  $a_n(t)$  are determined by Bessel functions. For the implementation, the argument of  $\Phi_n$  has to be mapped onto the interval  $[-i, i]$ . The eigenvalues of  $\mathbf{H}$  are consequently shifted and scaled to the range  $[-1, 1]$ . The propagation is then performed with the normalized Hamiltonian and a shift parameter is introduced, compensating for the normalization. The order of expansion  $N$  has to be chosen large enough to ensure the convergence of the series.

### 1.1.3 Eigenfunctions

The vibrational eigenfunctions  $\Psi_n$  have to be evaluated explicitly to set up the quantum dynamical calculations in the eigenstate representation. They can be determined by solving the stationary, vibrational Schrödinger equation:

$$\hat{H}_0(R)\Psi_n(R) = (E_{\text{el}}(R) + T_{\text{nuc}}(R))\Psi_n(R) = E_n\Psi_n(R). \quad (1.18)$$

A relaxation method [13, 14] is applied, where an incident, vibrational wave packet  $\Psi(t)$  is propagated in imaginary time. The propagation methods presented in Sec. 1.1.2 can be used, but here the wave functions and operators are constructed in the grid basis.

The components of the wave packet with the highest energies are attenuated faster during the propagation period and the wave packet is basically relaxed to the vibrational ground state.

$$\tilde{\Psi}_n(R) \equiv e^{-i\hat{H}_0(R)(-i\Delta t)}\Psi(R, t) = e^{-\hat{H}_0(R)\Delta t}\Psi(R, t) \quad (1.19)$$

This procedure is applied several times, for each eigenfunction and each time the resulting, approximated vibrational eigenfunction  $\tilde{\Psi}_n$  is projected out. Afterwards, the Hamiltonian is set up in the basis of the approximated eigenfunctions and diagonalized to obtain very exact solutions of the stationary, nuclear Schrödinger equation (Eq. 1.18).

### 1.1.4 Dissipative dynamics

In principle, a molecular subsystem, such as a vibrational normal mode, can never be regarded as a completely isolated system and environmental effects have to be taken into account. Molecular collision or intramolecular vibrational redistribution can occur, changing the population of the quantum states (relaxation) or stochastically perturbing the phase (dephasing). The simulation of these effects can be incorporated in the quantum dynamical studies, using density matrix theory [15].

### Density matrix

The molecular subsystems investigated in this thesis correspond to sets of selected vibrational normal modes. They can be regarded as open quantum systems in the density matrix formalism and can interchange energy with the environment, where the environmental effects are described as distortions. The

density matrix is a statistical operator, defined as:

$$\hat{\rho} = |\Psi\rangle\langle\Psi|, \quad (1.20)$$

with the vibrational state vector  $|\Psi\rangle$ . Expressing the wave function in the basis of vibrational eigenfunctions:  $|\Psi\rangle = \sum_n a_n |\Psi_n\rangle$  and  $\langle\Psi| = \sum_m a_m^* \langle\Psi_m|$  (in general, the coefficients are time-dependent) leads to the matrix representation  $\boldsymbol{\rho}$  of the operator  $\hat{\rho}$ :

$$\boldsymbol{\rho} = \sum_{nm} a_n a_m^* |\Psi_n\rangle\langle\Psi_m|. \quad (1.21)$$

The respective matrix elements of the density operator are given by:

$$\rho_{nm} = \langle\Psi_n|\boldsymbol{\rho}|\Psi_m\rangle = a_n a_m^*. \quad (1.22)$$

The diagonal elements  $\rho_{nn} = |a_n|^2$  are equal to the probability that the system is in the state  $|\Psi_n\rangle$  and the off-diagonal elements  $\rho_{nm}$  ( $n \neq m$ ) represent the coherences of the system. Due to the orthonormality of the basis functions, the trace of the density matrix is  $\text{Tr}(\boldsymbol{\rho}) = 1$ .

### Liouville equation

The temporal evolution of a quantum system, represented by a density matrix, is governed by the Liouville equation:

$$i \frac{\partial \boldsymbol{\rho}(t)}{\partial t} = [\mathbf{H}, \boldsymbol{\rho}(t)]. \quad (1.23)$$

Eq. 1.23 is known as the non-dissipative Liouville-von Neumann equation, which can also be rewritten as:

$$\dot{\boldsymbol{\rho}}(t) = \mathcal{L}\boldsymbol{\rho}(t) = -i[\mathbf{H}, \boldsymbol{\rho}(t)], \quad (1.24)$$

with the Hamiltonian Liouvillian superoperator  $\mathcal{L}$ . When the quantum system is interacting with the environment, the dynamics can be described by the dissipative Liouville-von Neumann equation under the Markov approximation (neglecting memory effects). The explicit bath modes (environment) are not treated explicitly, but their influence on the quantum system is described according to:

$$\dot{\boldsymbol{\rho}}(t) = \mathcal{L}\boldsymbol{\rho}(t) = (\mathcal{L}_{\text{sys}} + \mathcal{L}_D)\boldsymbol{\rho}(t) = -i[\mathbf{H}, \boldsymbol{\rho}(t)] + \mathcal{L}_D(\boldsymbol{\rho}(t)). \quad (1.25)$$

The Liouvillian superoperator  $\mathcal{L}$  consists of a system part  $\mathcal{L}_{\text{sys}}$  and a dissipative part  $\mathcal{L}_D$ . The dissipative correction  $\mathcal{L}_D$  is a function of the density matrix. Here, the Lindblad approach [16, 17, 18] to the Markovian description of open quantum systems is applied with the mathematical form:

$$\mathcal{L}_D(\rho(t)) = \sum_{i=0} \left\{ \mathbf{C}_i \rho \mathbf{C}_i^\dagger - \frac{1}{2} [\mathbf{C}_i^\dagger \mathbf{C}_i, \rho]_+ \right\}, \quad (1.26)$$

and the Lindblad operators  $\mathbf{C}_i$ . They correspond to raising and lowering operators of the  $i$ -th two-level system  $|a\rangle, |b\rangle$ , which is set up for every relaxation channel:

$$\hat{C}_i = \sqrt{\Gamma_{ab}} |a\rangle\langle b| = \sqrt{\Gamma_{ab}} \begin{pmatrix} 0 & 1 \\ 0 & 0 \end{pmatrix}, \quad \hat{C}_i^\dagger = \sqrt{\Gamma_{ba}} |b\rangle\langle a| = \sqrt{\Gamma_{ba}} \begin{pmatrix} 0 & 0 \\ 1 & 0 \end{pmatrix}. \quad (1.27)$$

The energy relaxation rates are defined as  $\Gamma_{ab} = \frac{1}{T_1}$ . Additionally, pure dephasing effects can be taken into account with Lindblad operators of the type:

$$\mathbf{C}_i = \sqrt{\gamma_{ab}^*} (|b\rangle\langle b| - |a\rangle\langle a|) = \sqrt{\gamma_{ab}^*} \begin{pmatrix} -1 & 0 \\ 0 & 1 \end{pmatrix}. \quad (1.28)$$

In this case,  $\gamma_{ab}^*$  is associated with the pure dephasing time scale  $T_2^*$ :  $\gamma_{ab}^* = \frac{1}{T_2^*}$ . The total dephasing rate is given by  $\frac{1}{T_2} = \frac{1}{T_2^*} + \frac{1}{2T_1}$ . Inserting the Lindblad approach for the dissipative part (Eq. 1.26) into the Liouville-von Neumann equation (Eq. 1.25) leads to the following equations of motion for the diagonal and off-diagonal elements of the density matrix:

$$\frac{\partial \rho_{nn}}{\partial t} = \sum_p^N -i[V_{np}(t)\rho_{pn} - \rho_{np}V_{pn}(t)] + \sum_p^N (\Gamma_{pn}\rho_{pp} - \Gamma_{np}\rho_{nn}), \quad (1.29)$$

$$\frac{\partial \rho_{mn}}{\partial t} = -i[(E_m - E_n)\rho_{mn} + \sum_p^N (V_{mp}(t)\rho_{pn} - \rho_{mp}V_{pn}(t))] - \gamma_{mn}^* \rho_{mn}. \quad (1.30)$$

The matrix  $\mathbf{V}$  is the laser-molecule interaction potential, defined as  $\mathbf{V} = -\boldsymbol{\mu}\varepsilon(t)$  and  $E_i$  are the vibrational eigenenergies, i.e. the diagonal matrix elements of the molecular Hamiltonian matrix  $\mathbf{H}_0$ .

## Propagation

As numerical method to solve the Liouville-von Neumann equation (Eq. 1.25) a polynomial expansion, related to the Chebychev propagation scheme, the Faber propagator [19, 20, 21] is used. The Chebychev polynomials are a special case of the Faber polynomials. The latter can be used to approximate functions of variables, defined in the complex plane. The formal solution of Eq. 1.25 is given by:

$$\boldsymbol{\rho}(t) = e^{\mathcal{L}(t-t_0)} \boldsymbol{\rho}(t_0), \quad (1.31)$$

with the initial density matrix  $\boldsymbol{\rho}(t_0)$  at the time  $t = t_0$ , where again the matrix representation is used for the quantum dynamical calculations. The Faber polynomial method is applied to approximate the exponential of the matrix  $\mathcal{L}$ :

$$\boldsymbol{\rho}(t) \equiv \sum_{k=0}^n b_k(t) F_k(\mathcal{L}) \boldsymbol{\rho}(t_0). \quad (1.32)$$

The structure is equivalent to the corresponding Chebychev approximation (Eq. 1.15), the time-dependent coefficients  $b_k(t)$  depend on Bessel functions and the domain of the complex eigenvalues of the Liouvillian, determined by the strength of the dissipative versus the system part. The Faber polynomials can be constructed according to a recursion relation, similar to the Chebychev polynomials. Detailed discussions on the Faber propagator can be found in [20, 19].

## 1.2 Quantum computing

Quantum information, as a rather young research area comprises the fields of quantum cryptography, quantum teleportation and quantum computing. It provides the opportunity for applications of principles from quantum theory to modern technologies. In this thesis, the control prospects of molecular vibrations with ultrashort laser pulses are studied with respect to the implementation of quantum logic gates of a quantum computer. The basic principles of quantum computing will be briefly reviewed, a corresponding detailed discussion can be found in [22]. Additionally, the main ideas and achievements of the concept of molecular quantum computing with vibrational qubits will be presented.

### 1.2.1 Universal quantum computing

R. Feynman first proposed the idea of a computer, processing data, with the help of quantum phenomena [23]. The concept of a universal quantum computer was presented by D. Deutsch, suggesting that a theoretical quantum computing machine should combine principles from quantum mechanics together with the concept of a Turing machine [24].

The main difference to a classical computer establishes in the units of information, which are quantum bits (qubits), instead of classical bits. Whereas, a classical bit is always represented by either of the two states 0 and 1, a qubit can take any state of a linear, coherent superposition of both basis states  $|0\rangle$  and  $|1\rangle$  with the probability amplitudes  $\alpha$  and  $\beta$ :

$$\psi = \alpha|0\rangle + \beta|1\rangle, \quad |\alpha|^2 + |\beta|^2 = 1; \quad \alpha, \beta \in \mathbb{C}. \quad (1.33)$$

Measuring the qubit in the standard basis, the probability of the outcome  $|0\rangle$  is  $|\alpha|^2$  and for  $|1\rangle$  it is  $|\beta|^2$ . The measurement leads to a collapse to a classical state. The state space for  $N$  classical bits is of the dimension  $2^N$ , where a register of  $N$  qubits spans a  $2^N$ -dimensional Hilbert space. Two major differences originate from the quantum nature of the qubits. One of them is quantum parallelism, which is the fundamental principle of the power of most modern quantum algorithms. It arises from the fact that the quantum register can exist in a superposition of basis states. An operation performed on this state is thus performed on each single component. A crucial point of quantum computing is the state measurement, where the probability is equal for each outcome. In P. Shor's algorithm for factorization [25] this problem is circumvented, as the superposition state is transformed into a state by a quantum Fourier transform (QFT) returning the correct answer with a high probability.

An additional point is quantum correlation or quantum entanglement, which is a pure quantum mechanical phenomenon. In case of a measurement of entangled multi-qubit states, the states of the single qubits are not independent anymore, but still the outcome of a single measurement is statistical. These states cannot be described by a direct product of the single qubit states, e.g.:

$$(a_1|0\rangle + b_1|1\rangle) \otimes (a_2|0\rangle + b_2|1\rangle) \neq \frac{1}{\sqrt{2}}(|00\rangle + |11\rangle). \quad (1.34)$$

Entanglement gives rise to the speedup of quantum algorithms operating on pure states.

D. Deutsch formulated requirements that have to be fulfilled by quantum computers [24]. One of these conditions is the preparation of a defined initial state. As a second point, the implementation of a universal set of quantum gates needs to be possible. The quantum gates are the elementary, logic operations, which can be performed by a quantum computer on the qubits. Quantum gates are reversible and can be represented mathematically by unitary matrices. The set of universal quantum gates consists of a certain reduced amount of operations, which can be used to express any unitary operation as a sequence of them [26]. It could be shown that this is fulfilled by the two-qubit controlled NOT (CNOT) gate together with all one-qubit gates NOT,  $\Pi$  and Hadamard. The corresponding Pauli matrices take the forms given in Eqs. 1.35 and 1.36 for the two-qubit basis  $\{|00\rangle, |01\rangle, |10\rangle, |11\rangle\}$ .

$$\mathbf{NOT} = \begin{pmatrix} 0 & 1 & 0 & 0 \\ 1 & 0 & 0 & 0 \\ 0 & 0 & 0 & 1 \\ 0 & 0 & 1 & 0 \end{pmatrix}, \quad \mathbf{CNOT} = \begin{pmatrix} 1 & 0 & 0 & 0 \\ 0 & 1 & 0 & 0 \\ 0 & 0 & 0 & 1 \\ 0 & 0 & 1 & 0 \end{pmatrix} \quad (1.35)$$

$$\mathbf{\Pi} = \begin{pmatrix} 1 & 0 & 0 & 0 \\ 0 & 1 & 0 & 0 \\ 0 & 0 & -1 & 0 \\ 0 & 0 & 0 & -1 \end{pmatrix}, \quad \mathbf{H} = \frac{1}{\sqrt{2}} \begin{pmatrix} 1 & 0 & 1 & 0 \\ 0 & 1 & 0 & 1 \\ 1 & 0 & -1 & 0 \\ 0 & 1 & 0 & -1 \end{pmatrix} \quad (1.36)$$

The NOT and CNOT gates, given in Eq. 1.35 are qubit flip gates. In case of the NOT operation the flip of the state of the second (active) qubit is performed, independently of the state of the first qubit. The corresponding CNOT gate involves a control qubit (first qubit). Only, if this is in state  $|1\rangle$ , the active (second) qubit is flipped. A phase rotation of  $\pi$  of a qubit in state  $|1\rangle$  is implemented by a  $\Pi$  operation (Eq. 1.36). The Hadamard gate (Eq. 1.36) involves phase rotations in combination with qubit flips and is essential for the preparation of superposition states. A corresponding set of gates exists, where the role of the first and second (passive and active) qubits are interchanged. In accordance to the definition that a universal set can be used to implement any quantum operation, the sequence  $\mathbf{CNOT}_2 \mathbf{CNOT}_1 \mathbf{CNOT}_2$  composes a SWAP operation.

A further requirement of D. Deutsch is the preferably correct readout of the qubits after the quantum gate operations. Additionally, DiVincenzo formulated further essential requirements [27] for the realization of quantum computers.

The defined qubit system needs to be scalable, the storage of quantum information data must be possible and stable, furthermore a favorable relation of switching to decoherence times needs to exist.

### 1.2.2 Implementation of quantum information processing

Only ten years after the first description of the universal quantum computer, the first CNOT gate was realized by C. Monroe and D. Wineland [28] based on trapped ions, an implementation previously proposed by I. Cirac and P. Zoller [29]. In principle, any two-level system could be used as a qubit system, but also multi-level systems are suitable, if there is a possibility to decouple the non-qubit basis states efficiently. The electronic states of the ions in an electromagnetic trap are used to code the qubit states. The quantum information can be processed through the collective motion of the ions in the trap. Lasers apply couplings between the qubit states or a coupling between the internal qubit states and the external motional states to perform quantum gates or generate entanglement. A strategy for scaling the ion trap approach to larger numbers of qubits has been developed, based on arrays of ion traps [30]. In 2005, the first quantum byte has been achieved [31]. Ion traps as qubit systems are only one of the proposals so far.

Another very promising quantum computing technology was proposed in 1997 by D. Cory and is based on nuclear magnetic resonance (NMR) [32, 33]. In the year 2000, a five-qubit NMR computer was presented using spin states of molecules as qubits [34]. The difference to other implementations is that the scheme is based on ensembles of molecules. The quantum gates are realized through radio frequency pulses.

Other concepts rely e.g. on electronic degrees of freedom in solid state, such as spins of electrons in quantum dots and superconducting flux (or charge) qubits in Josephson junctions [35, 36, 37, 38, 39, 40, 41]. A scalable setup for quantum computing with superconducting circuits has been recently presented [42]. Implementations based on photons, where e.g. the polarization of light codes the qubit states are also investigated [43, 44, 45].

### 1.2.3 Molecular quantum computing

The concept of molecular quantum computing with vibrational qubits was first proposed by C. Tesch and R. de Vivie-Riedle [7]. The qubit states are encoded

in vibrational states of normal modes of polyatomic molecules. Mediated by the molecular dipole moment, the quantum gates can be realized by ultrashort, specially shaped femto- to picosecond pulses. The theoretical proof of principle was presented for the molecule acetylene [7, 46, 46, 47], where in case of a two and three qubit system the universal set of quantum gates could be successfully implemented. Additionally, quantum algorithms, such as the Deutsch-Josza algorithm [48] or a QFT [49] were calculated for two-qubit systems. Further studies suggested to select transition metal carbonyls as promising candidates, due to strong IR absorbance [50, 51, 52]. Studies on the effects of molecular parameters determining the vibrational modes, the intramode anharmonicity and the anharmonic coupling reflected basic requirements on these parameters and the effects on the efficiencies and properties of the quantum gates [53]. Phase effects within the shaped laser pulses were investigated as well as a quantum Fourier transformation implemented [49]. Investigations of further molecular candidates with the same or similar qubit coding schemes were performed by several other groups [54, 55, 56, 57, 58, 59, 60, 61, 62, 63, 64, 65, 66]. A comprehensive review on this topic is given in [67]. First experiments, which may allow for the realization of the proposed quantum computing scheme, were presented recently [68, 69, 70, 71, 72]. Here, the shaping of mid-IR pulses and tracing the population mechanism is essential. How the control schemes are performed in experiment will be shown in Sec. 1.3.2. In theory, the optimization of the quantum gates is based on OCT, which will be introduced in Sec. 1.3.3.

## **1.3 Quantum control**

Quantum systems and quantum processes have been studied for a long time with lasers, the main goal was to understand the observed system [1]. In current experiments the central question is the controllability and efficient manipulation of quantum systems. Here, the aim is to steer quantum processes in a desired way, which is commonly referred to as quantum control [3]. The experiments are based on ultrashort laser pulses, which are amplitude and phase modulated. A brief overview will be given on ultrashort laser pulses. The experimental and theoretical approaches to quantum control will be illustrated, i.e. pulse shaping techniques based on evolutionary algorithms and OCT.

### 1.3.1 Ultrashort laser pulses

Ultrashort laser pulses are the driving force of quantum control experiments. Their generation, characterization and their mathematical description will be briefly reviewed.

#### Pulse generation and characterization

Ultrashort pulses in the femto- to picosecond regime can be realized by inserting amplitude modulators in the laser cavity [73]. Saturable absorbers, either organic dyes or semiconductor materials, are used for passive mode-locking, modulating the losses in the cavity. The materials bleach out at high intensities. Due to initial intensity fluctuations in the resonator, a stronger fluctuation will experience less loss and will self-amplify, as a result a short pulse is generated. Ultrashort pulses of a few femtoseconds can be realized based on the Kerr lens mode locking mechanism. The refractive index of a medium is intensity-dependent, for large pulse intensities. The refractive index changes across the pulse profile in a Kerr medium leading to self-focusing of the pulse.

For ultrashort pulse characterizations, the laser waveforms need to be sampled by comparatively short events and the used methods are based on (auto)correlation functions. One technique is frequency resolved optical gating (FROG) [74, 75]. Several delay times are scanned, where the pulse is gated with a replica. In experiment, this is performed by using nonlinear optical effects (such as second harmonic generation or two photon absorption). The correlation function is additionally spectrally dispersed and the frequency resolved correlation trace can be measured. A different technique is SPIDER (spectral phase interferometry for direct electric field reconstruction) [76, 77] based on spectral interferometry. Here, a pulse is interfered with a frequency-shifted replica of itself. In this thesis, some of the calculated pulses are transferred to the joint time-frequency domain using the FROG technique to retrieve information, which cannot be derived from the time or frequency representations solely.

#### Mathematical description

The time duration of an ultrashort pulse is on the order of femto- to picoseconds, exhibiting a broad spectrum according to the Fourier relation. The electric field of the pulses can either be specified in the time (Eq. 1.37) or in the frequency domain (Eq. 1.38), where both representations are connected via Fourier

transforms [78].

$$\varepsilon(t) = \frac{1}{2\pi} \int_{-\infty}^{\infty} \tilde{\varepsilon}(\omega) e^{i\omega t} d\omega = \mathcal{F}[\tilde{\varepsilon}(\omega)] \quad (1.37)$$

$$\tilde{\varepsilon}(\omega) = \int_{-\infty}^{\infty} \varepsilon(t) e^{-i\omega t} dt = \mathcal{F}^{-1}[\varepsilon(t)] \quad (1.38)$$

The complex Fourier transformation of the real, electric field  $\varepsilon(t)$  is complex-valued and obeys the symmetry  $\tilde{\varepsilon}(\omega) = \tilde{\varepsilon}^*(-\omega)$ , where  $*$  denotes the complex conjugated. It is sufficient to characterize the spectral field only by the positive-valued part  $\tilde{\varepsilon}^+(\omega)$ . The power spectrum of the laser field is determined by:

$$|\tilde{\varepsilon}(\omega)|^2 = \Re(\tilde{\varepsilon}^+(\omega))^2 + \Im(\tilde{\varepsilon}^+(\omega))^2. \quad (1.39)$$

An inverse, complex Fourier transformation of  $\tilde{\varepsilon}^+(\omega)$  leads to the associated description of a complex, time-dependent field (Eq. 1.40).

$$\varepsilon(t) = \tilde{\varepsilon}^+(t) + \tilde{\varepsilon}^-(t) \quad (1.40)$$

$$= \frac{1}{2} \mathcal{E}(t) e^{i\Gamma(t)} + c.c. \quad (1.41)$$

$$= \frac{1}{2} \mathcal{E}(t) e^{i\omega_0 t} e^{i\varphi(t)} + c.c. \quad (1.42)$$

$$= \mathcal{E}(t) \cos(\omega_0 t + \varphi(t)) \quad (1.43)$$

The complex field can also be represented by a product of a real amplitude function  $\mathcal{E}(t)$ , commonly known as the envelope function, and a phase term  $e^{i\Gamma(t)}$  (Eq. 1.41). Assuming the spectral amplitude centered around the carrier frequency  $\omega_0$ , Eq. 1.41 can be rewritten as Eq. 1.42, with the time-dependent phase  $\varphi(t)$ , or in concise form as Eq. 1.43. In general, the phase function can be expressed as a Taylor series around the time  $t = t_0$  (Eq. 1.44).

$$\begin{aligned} \varphi(t) &= \varphi(t_0) + \frac{d}{dt} \varphi(t_0) (t - t_0) + \frac{d^2}{dt^2} \varphi(t_0) (t - t_0)^2 + \dots \\ &= \varphi_{CEP} + \gamma t - \delta t^2 + \dots \end{aligned} \quad (1.44)$$

The zero-order temporal phase coefficient  $\varphi_{CEP}$  in Eq. 1.44 is commonly referred to as carrier-envelope phase (CEP) and corresponds to a constant phase. It describes the temporal relation of the envelope function with respect to the carrier frequency oscillation of the electric field at the time  $t_0$ , where it is assumed

that the field is centered around  $t_0$ . The higher order temporal phase coefficients are time-dependent. The first order coefficient  $\gamma$  leads to a frequency shift, whereas a time dependence of second order  $\delta$  induces a linear frequency change, denoted as linear chirp.

The pulse power per unit area in a material of refractive index  $n$  is given by the temporal intensity:

$$I(t) = \varepsilon_0 c n \frac{1}{T} \int_{t-T/2}^{t+T/2} \varepsilon^2(t') dt' = \frac{1}{2} \varepsilon_0 c n \mathcal{E}^2(t), \quad (1.45)$$

and by the energy density per unit area:

$$W = \int_{-\infty}^{\infty} I(t) dt. \quad (1.46)$$

The pulse durations  $\tau_p$  and the bandwidth, i.e. the spectral width  $\Delta\omega_p$  of the ultrashort pulses are commonly defined as the full width at half maximum (FWHM) of the intensity profiles:

$$\tau_p = \text{FWHM}\{I(t)\}, \quad (1.47)$$

$$\Delta\omega_p = \text{FWHM}\{I(\omega)\}. \quad (1.48)$$

Since the electric field in the time domain is directly related to the field in the spectral domain, Eq. 1.47 and Eq. 1.48 are interdependent. The corresponding time-bandwidth product:

$$\tau_p \Delta\omega_p \geq 2\pi c_B, \quad (1.49)$$

has a minimum value of  $c_B = 4 \ln 2 / (2\pi) = 0.441$  in case of a Gaussian pulse shape. If a pulse exactly fulfills the lowest limit, it is known to be bandwidth- or Fourier-limited (FL). The temporal dependence of a Gaussian pulse is:

$$\varepsilon(t) = \varepsilon_0 e^{-(t/\tau_G)^2} \cos(\omega_c t), \quad (1.50)$$

with the parameter  $\tau_G = \tau_p / \sqrt{2 \ln 2}$  and a maximum energy  $\varepsilon_0$  and the equivalent spectral dependence takes the form:

$$\tilde{\varepsilon}(\omega) = \varepsilon_0 e^{-2 \ln 2 \left( \frac{\omega - \omega_c}{\Delta\omega_p} \right)^2}. \quad (1.51)$$

### 1.3.2 Coherent control with genetic algorithms

Coherent control experiments based on learning loop techniques are used to control quantum processes with modulated laser light [4, 79, 80]. The fundamentals of the learning loops together with pulse shaping techniques will be introduced in this section. A key element of the optimization strategy is the genetic algorithm (GA), improving the shaped laser pulses. Since the use of GAs can also be adapted to theoretical control studies, the essentials of genetic computing are also reviewed. In the last part, OCT is addressed, which has proven to be a very powerful tool for the theoretical prediction of laser pulse shapes in control studies.

#### Learning loops and pulse shaping

Experimental learning loop techniques have been applied successfully in various fields on control problems from chemistry, physics and biology [81, 82, 83, 84, 85, 86, 87, 88]. They are based on tailored femtosecond pulses, acting on quantum systems. A pulse shaping device [89, 90, 91] is used as an external control source. A feedback signal, i.e. the systems' response, can be retrieved from the experiments. Alternatively, in a theoretical setup, the response signal can be calculated.

An optimization algorithm is used in both cases to improve the desired quantum processes, by means of altering the generated laser fields. In this thesis, the prospects of a theoretical learning loop approach based on GAs for different optimization tasks are explored. The learning loop experiments calculations can be performed by sending preliminary defined FL pulses through a theoretical pulse shaper.

A spectral pulse shaping device consists of two spectrometers, one which disperses the spectral components onto space in its Fourier plane and the other one is applied in a reversed way to recollimate the frequencies. A spatial light modulating (SLM) device can be inserted in the optical path, which can apply a spatial phase and transmittance pattern in the Fourier plane and the spectrum of the pulse becomes modulated. Most frequently, three types of SLMs are used, acousto-optic modulators, deformable mirrors or liquid crystal SLMs. The shaping process of a FL pulse  $\tilde{\varepsilon}_{\text{in}}(\omega)$  is mathematically described by:

$$\tilde{\varepsilon}_{\text{out}}(\omega) = M(\omega)\tilde{\varepsilon}_{\text{in}}(\omega), \quad (1.52)$$

where  $M(\omega)$  is called the mask function, consisting of a transmittance  $T(\omega)$  and a phase  $\phi(\omega)$  part [92, 93]. It can be decomposed into  $n$  different, complex-valued filter functions:

$$M_n(\omega_n^0) = T_n(\omega_n^0) \exp(i\phi_n(\omega_n^0)), \quad (1.53)$$

for each of the  $n$  pixels. Each pixel comprises a spectral range of  $\Delta\omega_n$  with the respective central frequency  $\omega_n^0$ . The total spectral range of the mask is  $\Delta\omega = \sum_n \Delta\omega_n$ . The transmittance function  $T(\omega)$  is defined in the interval  $[0, 1]$  and the phase function  $\phi(\omega)$  in the range  $[-\pi, \pi]$ . To describe the pulse shaping procedure theoretically, the discretized mask function is interpolated, using a cubic spline interpolation scheme and masked onto an incident FL pulse. The temporal electric field is modulated according to:

$$\tilde{\varepsilon}^{\text{mod}}(\omega) = \varepsilon_0 \sqrt{T(\omega)} e^{-2 \ln 2 \left( \frac{\omega - \omega_c}{\Delta\omega_p} \right)^2} e^{i\phi(\omega)}. \quad (1.54)$$

In case of the phase function  $\phi(\omega)$ , two approaches are possible, it can either be optimized in an analytic form, e.g. a sinusoidal phase modulation can be applied of the general form:

$$\phi(\omega) = \sum_i a_i \sin(b_i\omega + c_i). \quad (1.55)$$

In this case,  $3 \cdot i$  different parameters have to be optimized. Alternatively, each value of the phase function can be varied individually. For a shaper with  $N$  pixels,  $3 \cdot i$  or  $N$  parameters have to be optimized for the phase function. If additionally a transmittance function  $T(\omega)$  is taken into account in similar ways, the number basically doubles and a vector consisting of all these parameters has to be optimized by the GA.

## Genetic algorithms

The fundamentals of GAs are briefly introduced for the application of femtosecond pulse shaping. A general and very detailed review on GAs can be found in [94]. As a class of evolutionary algorithms, GAs are global search heuristics, frequently used for combinatorial optimization problems. The basic ideas are taken from evolutionary biology, the basic structure of a GA is sketched in Fig. 1.1 and will be explained in the following. For the first generation of a GA, a starting population of candidate solutions, called individuals, is randomly generated

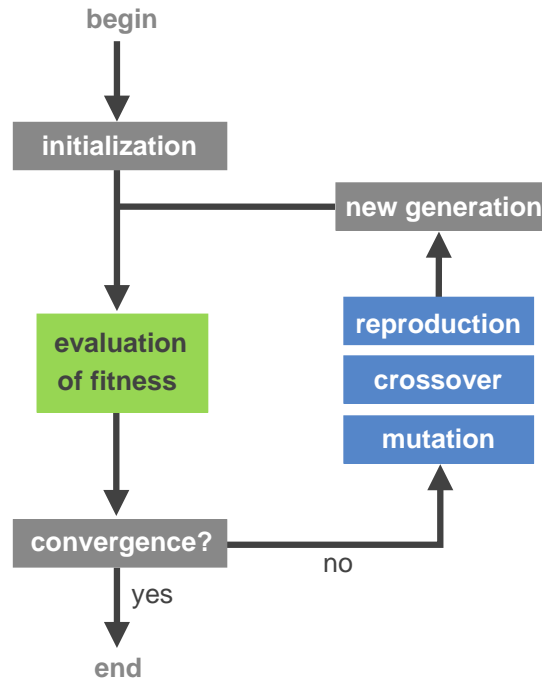


**Figure 1.1:** Structure of a genetic algorithm.

(initialization). Each individual has a genome, which corresponds to the phase and transmittance function in these simulations. A set of simple operations is defined, which generate the successive populations out of the initial population. The operators used in the GA are the selection (reproduction), the crossover (recombination) and the mutation operator.

In case of the selection operator, individuals are copied for the next generation according to their objective function value, i.e. the fitness. The fitness of each individual in the current population is evaluated by propagating the molecular system with each generated laser field and the efficiency of the quantum process is calculated. A higher fitness means that the probability for this individual, contributing offspring to the next generation is higher, which can be regarded as an artificial version of Darwinian natural selection. In algorithmic form, the selection operator can either be implemented by a biased roulette wheel, where a slot is assigned to each individual of the current generation. The slot size is defined proportionate to the fitness value of the respective individual. The candidates are selected by spinning the biased roulette wheel. The individuals,

performing better in the objective function, have a higher chance contributing offspring than others. Copies of the selected individuals are made, which enter a mating pool, corresponding to a new, tentative population. Another possibility of the selection operation is the tournament selection, which is based on a biased roulette wheel, but selects two individuals and decides for the higher-valued one. Consequently, more probably higher-valued individuals will be reproduced in case of the tournament selector.

After the selection has been performed in the GA, crossovers between the individuals in the mating pool take place. First, they are mated at random and crossings between a pair of individuals can occur. Different crossover techniques exist, a one-point crossover operation, used here, is based on a single crossover point of both parent individuals. All data of the genome beyond the crossing point is swapped between the two mating individuals and two new individuals are created.

The mutation operator plays only a secondary role and normally the mutation probability is chosen low compared to the recombination probability. The role of the mutation operator is to prevent the algorithm from loss of potential useful genetic material. A mutation randomly alters a single value in the genome of an individual, with a small probability.

The new generation of offspring is evaluated according to their fitness and evolves in the next iteration. In this thesis, a steady-state GA from the GALib genetic algorithm package [95] is applied. It is based on overlapping populations. The amount of overlap can be selected and corresponds to the percentage of the replaced population in each generation. Temporary, the offspring generation is added to the parent generation and the worst individuals are removed from the set. If an offspring is worse than an individual from the parent generation it will not pass over to the next generation. As an advantage, good solutions remain in the population for more iterations.

### **1.3.3 Optimal control theory**

The corresponding theoretical technique to quantum control experiments is OCT. An optimality criterion has to be achieved and the method finds an appropriate control law for it, the optimal laser field. Different OCT concepts for quantum control investigations were developed, predominantly in the groups of H. Rabitz [96, 6], D. Tannor and S. Rice [97, 5] based on the calculus of varia-

tions. In general, the following OCT functional (Eq. 1.56) has to be maximized.

$$J(\psi_i(t), \lambda(t), \varepsilon(t)) = F(\tau) - \int_0^T \alpha(t) |\varepsilon(t)|^2 dt - \int_0^T \lambda(t) G(\psi_i(t), \varepsilon(t)) dt \quad (1.56)$$

It includes three terms, the optimization aim  $F(\tau)$ , an integral over the laser field, penalizing the pulse fluence and an ancillary constraint.

The optimization aim  $F(\tau)$  is to transfer the initial wave function  $\psi_i$  into a final state  $\phi_f$  after the laser excitation time  $T$  and can be formulated as the square of the scalar product of the initial state, propagated in time with the target state:

$$F(\tau) = |\langle \psi_i(T) | \phi_f \rangle|^2. \quad (1.57)$$

Initial and target states can be chosen as eigenstates or arbitrary superpositions of eigenstates. For the implementation of global quantum gates, it is necessary to perform several qubit basis transitions with the same laser pulse. In this sense, global means that independently of the initial qubit state the correct transition has to be performed. For these calculations, the definition of the control aim is extended and for a  $N$ -dimensional qubit basis it takes the form:

$$F(\tau) = \sum_{k=1}^N |\langle \psi_{ik}(T) | \phi_{fk} \rangle|^2. \quad (1.58)$$

A different formulation of the optimization aim additionally facilitates the correct phase relation between the single transitions [98, 99, 49].

The second term of Eq. 1.56 is an integral over the laser field  $\varepsilon(t)$  with a time-dependent factor  $\alpha(t)$ . In principle, high values of  $\alpha$  assure low field intensities and complexities. Depending on the implementation, it is known as the penalty factor or Krotov change parameter. With the choice of  $\alpha(t) = \alpha_0/s(t)$  and e.g. a sinusoidal shape function  $s(t)$ , an envelope function can be impressed on the laser field [100, 14]. This guarantees smooth switching on and off behaviour of the pulse, instead of abrupt field intensity changes for the times  $t = 0, T$ .

The last term of the functional (Eq. 1.56) comprises the time-dependent Schrödinger equation as an ancillary constraint, denoted by  $G(\psi_i(t), \varepsilon(t))$ , with the Lagrange multiplier  $\lambda(t)$ :

$$\int_0^T \lambda(t) G(\psi_i(t), \varepsilon(t)) = 2\Re \left[ C \int_0^T \langle \lambda(t) | i \left[ \hat{H}_0 - \hat{\mu} \varepsilon(t) \right] + \frac{\partial}{\partial t} | \psi_i(t) \rangle dt \right]. \quad (1.59)$$

Separable differential equations can be derived from this form due to the formulation  $2\Re$  in Eq. 1.59 and a suitable choice of the factor  $C$  in dependence on the definition of the optimization aim. In case, a single transition is chosen as control aim (Eq. 1.57), the factor  $C$  becomes  $C = \langle \psi_i(t) | \psi_f(t) \rangle$ . For multi-target optimal control theory (MTOCT) the control objective equals Eq. 1.58 and the factor  $C$  in the ancillary constraint includes a sum, running over all  $k$  transitions. The complete multi-target functional reads:

$$\begin{aligned}
 J(\psi_{ik}(t), \lambda_k(t), \varepsilon(t)) &= \sum_{k=1}^N \left\{ |\langle \psi_{ik}(t) | \phi_{fk} \rangle|^2 \right. \\
 &\quad \left. - 2\Re \left[ \langle \psi_{ik}(T) | \phi_{fk} \rangle \int_0^T \langle \lambda_k(t) | i \left[ \hat{H}_0 - \hat{\mu} \varepsilon(t) \right] + \frac{\partial}{\partial t} | \psi_{ik}(t) \rangle dt \right] \right\} \\
 &\quad - \alpha_0 \int_0^T \frac{|\varepsilon(t)|^2}{s(t)} dt. \tag{1.60}
 \end{aligned}$$

The calculation of optimal laser fields now relies on finding the extremum of the functional (Eq. 1.60) with respect to the functions  $\psi_{ik}(t)$ ,  $\lambda_k(t)$  and  $\varepsilon(t)$ . The derivative of the functional with respect to  $\lambda_k(t)$  and  $\psi_{ik}(t)$  leads to the following coupled equations of motion:

$$i \frac{\partial}{\partial t} \psi_{ik}(t) = \left[ \hat{H}_0 - \hat{\mu} \varepsilon(t) \right] \psi_{ik}(t), \quad \psi_{ik}(0) = \phi_{ik}, \tag{1.61}$$

$$i \frac{\partial}{\partial t} \lambda_k(t) = \left[ \hat{H}_0 - \hat{\mu} \varepsilon(t) \right] \lambda_k(t), \quad \lambda_k(T) = \phi_{fk}, \tag{1.62}$$

with the corresponding boundary conditions. The propagated wave functions  $\psi_{ik}(t)$  have to correspond to the initial states  $\phi_{ik}$  at the time  $t = 0$  and the Lagrange multipliers are equal to the target states at the end of the propagation  $\lambda(T) = \phi_{fk}$ . According to [96], the functional (Eq. 1.60) is also differentiated with respect to the laser field  $\varepsilon(t)$ , where only linear terms are kept and terms containing  $(\delta\varepsilon(t))^2$  are neglected.

$$\begin{aligned}
 \delta_{\varepsilon(t)} J &= J(\psi_{ik}(t), \lambda_k(t), \varepsilon(t) + \delta\varepsilon(t)) - J(\psi_{ik}(t), \lambda_k(t), \varepsilon(t)) \\
 &\approx - \sum_{k=1}^N \int_0^T \left[ 2\alpha_0 \frac{\varepsilon(t)}{s(t)} + 2\Im \langle \psi_{ik}(t) | \phi_{fk} \rangle \langle \psi_{fk}(t) | \hat{\mu} | \psi_{ik}(t) \rangle \right] \delta\varepsilon(t) dt \\
 &= 0 \tag{1.63}
 \end{aligned}$$

Since there is no incident condition imposed on  $\delta\varepsilon(t)$ , Eq. 1.63 is fulfilled when the integrand turns zero and an equation constructing the electric field can be derived:

$$\varepsilon(t) = -\frac{s(t)}{\alpha_0 N} \Im \left[ \sum_{k=1}^N \langle \Psi_{ik}(t) | \Psi_{fk}(t) \rangle \langle \psi_{fk}(t) | \hat{\mu} | \psi_{ik}(t) \rangle \right]. \quad (1.64)$$

The coupled Eqs. 1.61, 1.62, 1.64 can be interpreted in different ways and different methods to obtain the optimal field were proposed. The schemes can be based on gradient-type optimization of the laser fields [101, 102]. Alternatively, the Krotov method, which is a global iterative procedure, was developed [5, 103, 99]. In this case, the  $2N + 1$  coupled differential equations (Eqs. 1.61, 1.62, 1.64) are solved iteratively by a self-consistent field method, which proceeds in the following way. The target states  $\Psi_{fk}(t)$  are propagated backward in time with the electric field  $\varepsilon(t)$  (Eq. 1.62). Afterwards, simultaneous propagation forward in time of the wave functions and the target states takes place (Eqs. 1.61, 1.62), where the new field is determined in each step as intermediate feedback according to Eq. 1.64. This field is then used in the next iteration for back-propagation. Also, schemes using an immediate feedback from the control field in an entangled fashion were proposed, where quadratic convergence is reached [6].

According to [104], the constraint on the pulse fluence can also be chosen to take the form:

$$\int_0^T \frac{\alpha_0}{s(t)} [\varepsilon(t) - \varepsilon'(t)]^2, \quad (1.65)$$

in the OCT functional (Eq. 1.60), where  $\varepsilon'(t)$  corresponds to the electric field from the previous iteration. The constraint restricts the change in pulse energy in each iteration with the Krotov change parameter  $\alpha_0$ . In the next iteration step of MTOCT, the improved laser field  $\varepsilon(t)^{k+1}$  is constructed as follows:

$$\varepsilon^{k+1}(t) = \varepsilon^k(t) + \frac{s(t)}{\alpha_0 N} \Im \left[ \sum_{k=1}^N \langle \Psi_{ik}(t) | \Psi_{fk}(t) \rangle \langle \psi_{fk}(t) | \hat{\mu} | \psi_{ik}(t) \rangle \right]. \quad (1.66)$$

This method is known as the modified Krotov OCT scheme.

From the OCT-optimized laser fields, the mask functions can be retrieved [92] according to:

$$M(\omega) = \tilde{\varepsilon}^+(\omega) / \varepsilon_{\text{in}}(\omega). \quad (1.67)$$

The calculated, shaped OCT pulses are Fourier transformed and the positive, spectral part, centered at the frequency  $+\omega_0$  is fitted with a Gaussian envelope  $\varepsilon_{\text{in}}(\omega)$ , centered at the same frequency. Since the shaping device can only attenuate or retard spectral components, the fit is required to encompass all frequency components of the shaped OCT field. The calculated mask functions are a direct link between OCT and the corresponding optimal control experiments (OCEs).

## **2 Molecular quantum computing based on the stimulated, non-resonant Raman effect**

Thus far, the concept of molecular quantum computing with vibrational qubits has been implemented theoretically in IR active vibrational normal modes with very high quantum efficiencies [50]. The logic gate operations are realized by shaped laser pulses in the mid-IR regime. First applications of direct pulse shaping techniques in this frequency regime were demonstrated in the latest experiments [68, 69], which presently open a way for the realization of vibrational qubits in the IR regime. The first efficient vibrational state-to-state transitions, which are key elements of vibrational IR quantum gates, have been shown recently [70].

In contrast, shaping of laser light in the UV/VIS and near-IR domain is a widely established technique [105, 106, 107, 81, 87] and the implementation prospects of molecular non-resonant Raman quantum gates in the easily accessible frequency regime are investigated and presented for the first time. This type of quantum gates will provide new flexibilities, such as the choice of laser wavelengths.

### **2.1 Stimulated, non-resonant Raman quantum computing**

In the initially proposed concept of molecular quantum computing, the qubit states were defined by vibrational eigenstates of an IR active normal mode and specially shaped IR laser fields act as the quantum gate operations [7]. This scheme is now transferred to Raman active vibrational normal modes, where equivalently the degree of excitation of the selected modes codes the qubit basis

states  $|0\rangle$  and  $|1\rangle$ , as exemplified in Fig. 2.1. Based on the stimulated, non-resonant Raman effect, the quantum logic operations can be implemented and the laser-molecule interaction is mediated by the molecular polarizability  $\hat{\alpha}$ , in this case.

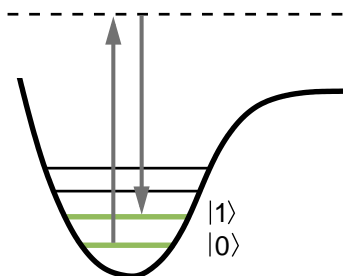


**Figure 2.1:** Example of a one-qubit system. The qubit basis states  $|0\rangle$  and  $|1\rangle$  are coded by two vibrational states (green) and the qubit flips are performed by a non-resonant laser-molecule interaction.

Finding a suited molecular system for the theoretical proof of principle is not a trivial task. From previous studies [53] it is known that the selected normal modes of the candidate have to fulfill several requirements. To set up a two-qubit system, the molecule must exhibit at least two strong Raman active vibrational modes. Typically, C-H stretching vibrations meet this demand. Besides the spectroscopic activity, the set of selected vibrational modes should be strongly anharmonic, with respect to the intra- ( $\Delta_i$ ) and intermode ( $\Delta_{ij}$ , also known as anharmonic coupling) anharmonicities [53]. The relevance of this requirement is demonstrated in Fig. 2.2. The level structure of a model two-qubit system is presented in Fig. 2.2 a), where the arrows indicate qubit basis and subsequent transitions, which are relevant for the discussion. Mostly, two different cases may be existent in a set of two vibrational modes. In the first case [upper panel of Fig. 2.2 b)], the intramode anharmonicity is similarly high as the anharmonic coupling. This turns out as a favorable situation for the implementation of a CNOT gate, where only a qubit flip (green line) occurs if the control qubit (first qubit in this example) is in state  $|1\rangle$ . The optimized laser pulse is most probably centered at the transition frequency  $|10\rangle \rightarrow |11\rangle$  (green line), as shown in Fig. 2.2 c), upper panel. In contrast, the intramode anharmonicity may be sig-

nificantly stronger than the intermode anharmonicity [Fig. 2.2 b), lower panel], which leads to two close transition frequencies  $|10\rangle \rightarrow |11\rangle$  (green line) and  $|00\rangle \rightarrow |01\rangle$  [black line, Fig. 2.2 b) and c), lower panels]. For such a molecular case, a NOT gate involving the two qubit flips (green and black line) can be realized easily.

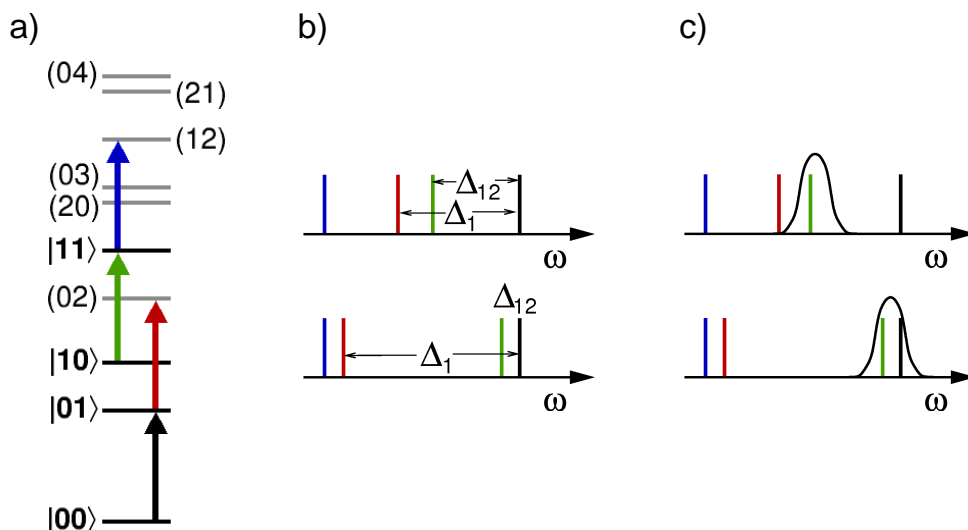


**Figure 2.2:** Clarification of the role of normal mode anharmonicities for the implementation of quantum logic gates in a two-qubit system. a) Level structure of a model two-qubit system. The arrows indicate qubit basis and subsequent transitions. b) Definition of the intramode anharmonicity  $\Delta_i$  and the anharmonic coupling  $\Delta_{ij}$  for two different model systems. c) Spectrum of laser pulses acting as quantum gates with respect to the vibrational transition frequencies.

A promising molecular candidate needs to be suited for the implementation of the complete universal set of quantum gates and not only for one single logic operation. Therefore, the system must provide balanced anharmonic properties, so each quantum gate operation can be realized by simple structured and short laser pulses.

A favorable candidate, complying with these conditions was found by scanning several molecules with promising Raman spectra, i.e. at least two strong Raman active and resolvable modes. Quantum chemical calculations (b3lyp/6-

31++G\*\*) were performed to investigate the corresponding anharmonic features [108]. The most promising molecule was found to be *n*-butylamine with the two strongly Raman active C-H stretching modes depicted in Fig. 2.3. The funda-

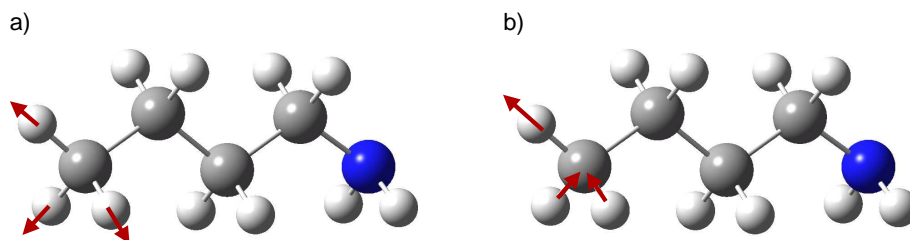


**Figure 2.3:** *n*-butylamine - candidate for the implementation of non-resonant Raman quantum gates. The two-qubit basis states are defined by the vibrational ground states and first excited states of the two Raman active C-H stretching modes depicted in a) and b).

mental frequencies of these modes are  $\nu_1 = 2990 \text{ cm}^{-1}$  and  $\nu_2 = 3030 \text{ cm}^{-1}$  and the anharmonicities  $\Delta_1 = 74 \text{ cm}^{-1}$ ,  $\Delta_2 = 103 \text{ cm}^{-1}$  and  $\Delta_{12} = 22 \text{ cm}^{-1}$ .

The potential energy surface and the polarizability tensor components were calculated along the vibrational modes. The 2D structure of the selected components  $\alpha_{xx}$ ,  $\alpha_{yy}$ ,  $\alpha_{zz}$ ,  $\alpha_{xy}$  of the polarizability are depicted in Fig. 2.4. The eigenfunctions and eigenvalues were explicitly evaluated with the relaxation method presented in Sec. 1.1.3 and the transition frequencies and anharmonicities determined. The eigenfunctions were used to transfer the polarizability components into the eigenstate representation (equivalently to the dipole moment in Eq. 1.12).

For the definition of the two-qubit basis ( $|00\rangle$ ,  $|01\rangle$ ,  $|10\rangle$ ,  $|11\rangle$ ) as sketched in Fig. 2.3 the vibrational ground state of each selected normal mode is encoded as the logic value  $|0\rangle$  and the first excited state as the logic value  $|1\rangle$ .

## 2.2 MTOCT with frequency filters

The quantum operations are based on the stimulated, non-resonant Raman effect and the induced quantum dynamics obeys the following Schrödinger equation:

$$i\frac{\partial}{\partial t}\Psi(t) = \hat{H}_0\Psi(t) - \frac{1}{2}\varepsilon_1(t)\hat{\alpha}\varepsilon_2(t)\Psi(t). \quad (2.1)$$

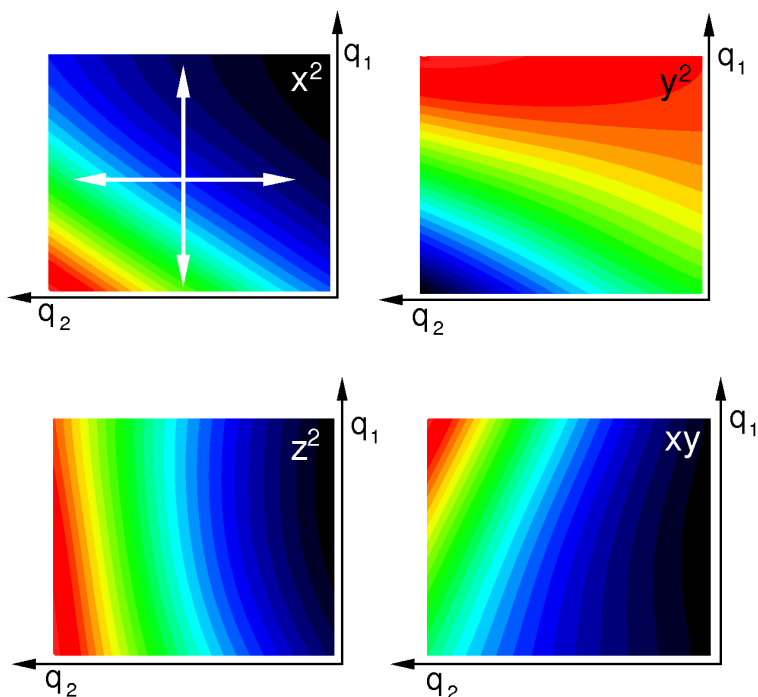


**Figure 2.4:** 2D structure of four selected components of the polarizability tensor  $\hat{\alpha}$  along the two selected C-H stretching modes of *n*-butylamine.

The laser-molecule interaction is dependent on the two control fields  $\varepsilon_1(t)$  and  $\varepsilon_2(t)$ . A new strategy has to be developed for the simultaneous optimization of both laser pulses. The multi-target formulation of the OCT functional Eq. 1.60 with the time-dependent Schrödinger equations (Eq. 2.1) cannot be applied in this case, as will be explained in detail, since it demonstrates the difficulties which arise from optimal control calculations of non-linear, non-resonant processes.

As a first step the desired control objective is assumed as a simple state-to-state transition from the vibrational ground state ( $\Psi_i = \Psi_0$ ) to the first excited state ( $\Psi_f = \Psi_1$ ), as indicated in Fig. 2.5 a). Even, if additionally one laser is kept fixed ( $\varepsilon_1$ ) during the optimization with the OCT scheme (Eq. 1.60) and the time-dependent Schrödinger equation (Eq. 2.1), the result will differ from the initially desired one, sketched in Fig. 2.5 a). This situation is visualized in Fig. 2.5 b), the two processes marked on the left (light-blue and dark-blue) and

on the right (green and light-blue) are not distinguishable within this formalism and both paths will be used. Consequently, the spectrum of the optimized laser field  $\varepsilon_2$  will contain two frequency components  $\omega_2$  and  $\omega_3 = \omega_2 + 2\Delta$  [Fig. 2.5 c),  $\Delta$  corresponds to the transition frequency  $|0\rangle \rightarrow |1\rangle$ ]. This point is not inherently problematic yet, but also does not correspond to the simplest solution of a pulse with one distinct carrier frequency, as considered in Fig. 2.5 a). The OCT algorithm (based on Eq. 1.60) completely fails, if both laser fields  $\varepsilon_1(t)$  and  $\varepsilon_2(t)$  are optimized simultaneously, since equivalently to the frequency component  $\omega_2$ , which splits into the two components  $\omega_2$  and  $\omega_3$ , in addition the spectrum of the previously fixed laser  $\varepsilon_1(t)$  will also start to split into two components  $\omega_1$  and  $\omega_1 + 2\Delta$ . As a further progressive effect, the spectra of both laser fields will spread completely in the frequency domain.

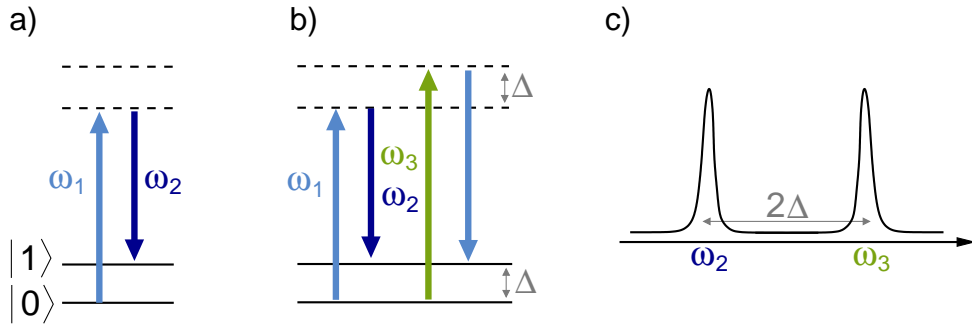


**Figure 2.5:** a) Level scheme of a non-resonant Raman state-to-state transition, which has to be optimized. b) In case of the OCT optimization of the laser field  $\varepsilon_2(t)$  [ $\varepsilon_1(t)$  is fixed during this optimization], the two indicated processes are not distinguishable for the OCT algorithm and both transition pathways are used. c) Resulting spectrum of the optimized laser field  $\varepsilon_2(t)$ .

As an answer to this problem, one has to gain control over the laser pulse spectra within the OCT formalism. Several suggestions have been presented, dealing with this challenge and introducing this feature in different ways [101, 109, 110, 92]. However, all approaches demonstrated so far do not show monotonic convergence or are not generally applicable.

A new, modified implementation of OCT based on the Krotov method, which allows for strict limitations on the spectrum of the optimized laser fields, was developed and will be presented [111]. The new multi-target optimal control

functional for a molecular non-resonant Raman interaction takes the form:

$$\begin{aligned}
 J[\Psi_k(t), \Phi_k(t), \varepsilon_1(t), \varepsilon_2(t)] = & \\
 \sum_{\mathbf{k}} \left\{ & |\langle \Psi_k(T) | \Phi_k \rangle|^2 - \sum_{l=1}^2 \alpha_0 \int_0^T \frac{|\varepsilon_l(t) - \tilde{\varepsilon}_l(t)|^2}{s(t)} dt - \sum_{l=1}^2 \gamma_l |F_l(\varepsilon_l(t))| \right. \\
 & \left. - 2 \Re \left[ \langle \Psi_k(T) | \Phi_k \rangle \int_0^T \langle \Phi_k(t) | \left[ i \left( \hat{H}_0 - \frac{1}{2} \varepsilon_1(t) \hat{\alpha} \varepsilon_2(t) \right) + \frac{\partial}{\partial t} \right] | \Psi_k(t) \rangle dt \right] \right\}. \quad (2.2)
 \end{aligned}$$

It includes the two laser fields  $\varepsilon_l(t)$  with  $l = 1, 2$  and the time-dependent Schrödinger Eq. 2.1 with the non-resonant Raman interaction. The control objective is determined by the square of each overlap  $\langle \Psi_k(T) | \Phi_k \rangle$  of the propagated initial states  $\Psi_k(T)$  at the final time  $T$  with the target states  $\Phi_k$  of the global quantum gate operation. The change of the pulse energy is restricted with the Krotov change parameter  $\alpha_0$ . The appropriate choice of the initial reference field  $\tilde{\varepsilon}_l(t)$  and of the parameter  $\alpha_0$  finds solutions of minimal pulse energies. A temporal shape function [100]  $s(t)$  is inserted to achieve smooth switching on and off behavior of each laser field. The temporal duration of the laser-molecule interaction can be limited either by the total time  $T$  or by the shape function  $s(t)$ , in accordance to the control scenario and the decoherence time scales. The wave function has to satisfy the time-dependent Schrödinger equation (Eq. 2.1) including the time evolution of the non-resonant Raman process.

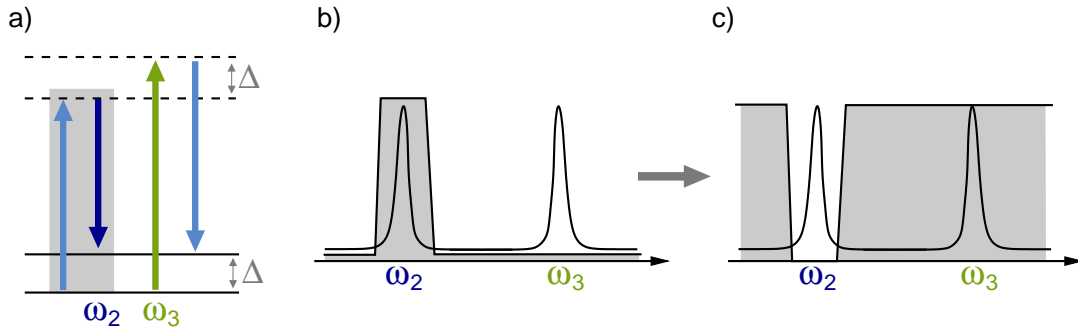


**Figure 2.6:** a) Performed filtering operation of the laser field spectra for the optimization of a non-resonant Raman transition. b) Respective band-pass filter and c) band-stop filter.

A new frequency constraint is introduced in the MTOCT functional (Eq. 2.2), where the new terms  $F_l(\varepsilon_l(t))$  are given in the time representation and restrict each electric field  $\varepsilon_l(t)$ . Throughout the formalism, the frequency filter operation is treated mathematically correct, together with the corresponding Lagrange multipliers  $\gamma_l(t)$ . The filter operations can in principle be realized in the time domain by linear digital filters, and particularly by finite impulse response (FIR) filters [112]:

$$F(\varepsilon(t)) = \sum_{j=0}^N c_j \varepsilon(t - j\Delta t), \quad (2.3)$$

with the FIR filter coefficients  $c_j$  and the step size  $\Delta t$  in the discrete time representation. By variation of the MTOCT functional (Eq. 2.2) with respect to the initial states  $\Psi_k(t)$ , the target states  $\Phi_k(t)$  and the laser fields  $\varepsilon_l(t)$ , a set of coupled differential equations can be derived. The iterative calculation of the laser fields is performed with the Krotov method [103]. The next iteration step  $n + 1$  for the laser field  $\varepsilon_1(t)$  and analogously for  $\varepsilon_2(t)$  can be formulated as:

$$\varepsilon_1^{n+1}(t) = \varepsilon_1^n(t) - \frac{s(t)}{2\alpha_0} \left( \gamma_1(t) - \sum_k C_{1,k} \right), \quad (2.4)$$

with  $\varepsilon_1^n(t) = \tilde{\varepsilon}_1(t)$ , and:

$$C_{1,k} = \Im[\langle \Phi_k(t, \varepsilon_1^n, \varepsilon_2^n) | \Psi_k(t, \varepsilon_1^{n+1}, \varepsilon_2^{n+1}) \rangle \times \langle \Phi_k(t, \varepsilon_1^n, \varepsilon_2^n) | \hat{\alpha} \varepsilon_2^{n+1} | \Psi_k(t, \varepsilon_1^{n+1}, \varepsilon_2^{n+1}) \rangle]. \quad (2.5)$$

The Lagrange multipliers  $\gamma_l(t)$  can be interpreted as correction fields needed to suppress the undesired frequency components. In the optimal case the Lagrange multipliers  $\gamma_l(t)$  are adjusted to subtract exactly the undesired field components from the optimized uncorrected fields  $\sum_k C_{l,k}$  (Eq. 2.5). The spectral constraint  $F_l(\varepsilon_l(t))$  depends only linearly on each electric field and it is possible to realize the side conditions  $|F_l(\varepsilon_l(t))| = 0$  using Fourier filters  $f_l(\omega)$ . It turned out that under practical considerations, it is easier to use Fourier filters instead of FIR filters. The Lagrange side conditions can be implemented in form of band-stop filter operations [Fig. 2.6 c)] using the inverse  $f_l'(\omega) = 1 - f_l(\omega)$  of the band-pass filters [Fig. 2.6 b)]  $f_l(\omega)$ , which guarantees that only the undesired spectral components pass the band-stop filters [Fig. 2.6 c)]. The spectral and temporal shape functions have to obey the time-frequency uncertainty principle.

The Lagrange multipliers  $\gamma_l(t)$  cannot be determined directly. In fact, for the calculation of  $\gamma_l(t)$  the field change  $\sum_k C_{l,k}$  must be predicted in the actual iteration step. This task is performed by propagating the target states  $\Phi_k$  and the initial wave functions  $\Psi_k$  with the laser fields  $\varepsilon_l^n(t)$  from the previous iteration. The construction of the resulting fields  $\gamma_l'(t)$  resembles the OCT fields of the unmodified algorithm.

$$\begin{aligned} \gamma_1'(t) &= \sum_k \Im[\langle \Phi_k(t, \varepsilon_1^n, \varepsilon_2^n) | \psi_k(t, \varepsilon_1^n, \varepsilon_2^n) \rangle \\ &\times \langle \Phi_k(t, \varepsilon_1^n, \varepsilon_2^n) | \hat{\alpha} \varepsilon_2^n | \psi_k(t, \varepsilon_1^n, \varepsilon_2^n) \rangle] \approx \sum_k C_{1,k} \end{aligned} \quad (2.6)$$

Filtering this output  $\gamma_1'(t)$  or analogously  $\gamma_2'(t)$  with the band-stop filter  $f_l'(\omega)$  [Fig. 2.6 c)] transforms them into the correction fields  $\gamma_1(t)$  or  $\gamma_2(t)$ . The transformation is accomplished with the help of Fourier transforms  $\mathcal{F}$ .

$$\gamma_l(t) = \mathcal{F}^{-1}[f_l'(\omega) \cdot \mathcal{F}(\gamma_l'(t))] \quad (2.7)$$

Each of the new fields  $\varepsilon_l^{n+1}(t)$  can now be calculated by inserting the result from Eq. 2.7 in Eq. 2.4. The Lagrange multipliers  $\gamma_l(t)$  represent the time-dependent electric fields of the undesired frequency components. The correction fields are evaluated in each iteration step and are subtracted from the optimized uncorrected field (Eq. 2.4). Finally, to maintain the validity of the side condition the optimized field has to be filtered with the band-pass operation  $f_l(\omega)$  after each iteration.

The modified OCT scheme provides monotonic convergence, i.e. each iteration step improves the objective. Its convergence is proved analogously to the procedure given in [104] for standard Krotov OCT. The difference in the line of argumentation arises from the new constraints and enters in:

$$\begin{aligned} \int_0^T & - \frac{\alpha_0}{s(t)} \Delta \varepsilon_l^2(t) + \gamma_l(t) |F_l(\varepsilon_l^{n+1}(t))| - \gamma_l(t) |F_l(\varepsilon_l^n(t))| \\ & + \Delta \varepsilon_l(t) \left[ 2 \frac{\alpha_0}{s(t)} \Delta \varepsilon_l(t) + \gamma_l(t) \right] dt \geq 0, \end{aligned} \quad (2.8)$$

(conforming with Eq. A15 of [104]).  $\Delta \varepsilon_l(t) = \varepsilon_l^{n+1}(t) - \varepsilon_l^n(t)$  denotes the change of the laser fields between two iterations.

In accordance with a Lagrange side condition, the output of the filter operations has to be zero. Consequently, all terms of Eq. 2.8 containing  $F_l(\varepsilon(t))$

become zero. Inserting Eq. 2.4 into Eq. 2.8 leads to:

$$\int_0^T \frac{3}{4} \frac{s(t)}{\alpha_0} \gamma_i^2(t) + \frac{s(t)}{\alpha_0} \gamma_i(t) \sum_k C_k + \frac{1}{4} \frac{s(t)}{\alpha_0} \left( \sum_k C_k \right)^2 dt \geq 0, \quad (2.9)$$

where only one non-quadratic term appears besides two positive, quadratic ones. As a result, the integral is always greater than or equal to zero, which meets the requirements of monotonic convergence.

## 2.3 Molecular candidate and Raman quantum gates

The theoretical implementation of Raman quantum gates, comprising a non-resonant, two-photon, two-color process, can be regarded as a great challenge for the new OCT scheme with frequency filters (Eq. 2.2). The quantum dynamics are carried out with a Chebychev propagation scheme (Sec. 1.1.2, [113]).

A schematic sketch of the vibrational ladder and the transitions induced by the two quantum gate operations NOT and CNOT are depicted in Fig. 2.7. As already explained, the OCT scheme (Eq. 1.60) fails for the simultaneous optimization of two non-resonant laser fields, since the virtual states are not determined within the formalism and the carrier frequencies of the laser pulses are independent of the eigenvalues of the system. The new algorithm provides the opportunity to optimize both laser fields within a selected and limited frequency range and simple structured, stimulated, non-resonant Raman quantum gates with high efficiencies can be predicted for the first time.

The OCT calculations were performed in the eigenstate representation, using the 50 lowest eigenstates. The laser-molecule interaction is based on the  $x^2$ -tensor component (Fig. 2.4) and consequently both laser fields  $\varepsilon_1(t)$  and  $\varepsilon_2(t)$  are assumed  $x$ -polarized. For the optimizations, temporal shape functions of the form:

$$s(t) = \sin^2 \left( \frac{t}{T} \pi \right), \quad (2.10)$$

are used, where the time  $t$  runs from 0 to  $T$ , the end of the laser-molecule interaction period. A universal set of quantum gates is implemented for the  $n$ -butylamine two-qubit system by stimulated, non-resonant Raman processes. The CNOT, NOT and Hadamard gate with efficiencies above 99 % are presented

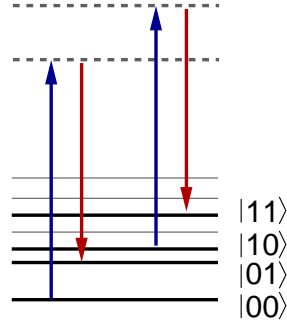


**Figure 2.7:** Stimulated, non-resonant Raman quantum gates. a) A global NOT gate is indicated by the arrows  $|00\rangle \leftrightarrow |01\rangle$  and  $|10\rangle \leftrightarrow |11\rangle$ . A CNOT gate is realized by pulses, switching the state of the active qubit when the control qubit (first qubit) is in state  $|1\rangle$  and induces the population transfer  $|10\rangle \leftrightarrow |11\rangle$ .

in Fig. 2.8. The  $\Pi$  gate is assumed to be implemented by a time delay for the correct phase rotation. The laser fields  $\varepsilon_1(t)$  and  $\varepsilon_2(t)$  of the global CNOT gate can be realized by simple Gaussian-shaped laser fields [compare Fig. 2.8 a) for  $\varepsilon_1(t)$ , the shape of  $\varepsilon_2(t)$  is equivalent]. Their related spectra are depicted together with their band-pass filter functions  $f_l(\omega)$  in Fig. 2.8 b). The carrier frequencies were chosen to be in the near IR regime with 800 nm ( $12500 \text{ cm}^{-1}$ ) and 643 nm ( $15541 \text{ cm}^{-1}$ ). The global NOT and Hadamard operations [Fig. 2.8 c) and d)] are more complex in structure, because two vibrational transitions [compare Fig. 2.7 a) for the NOT gate] have to be driven simultaneously and the fundamental qubit transition is close to the corresponding passive one. The  $x^2$ -tensor component of the polarizability drives the vibrational transitions for both qubit modes. Thus, it can be expected that polarized fields shaped to discriminate the qubit modes, might further simplify the laser field structures.

The monotonic convergence for the CNOT gate optimization with a Krotov change parameter  $\alpha_0 = 10$  (referring to the fluence integral calculated in au) can be traced from Fig. 2.9, solid line. The dashed line shows the evolution (normalized to unity) of the undesired spectral components during the optimization. Since the guess fields were chosen as simple, bandwidth tailored Gaussian-shaped laser fields, no frequency components have to be suppressed. In the first iteration step, the amount of undesired spectral components jumps

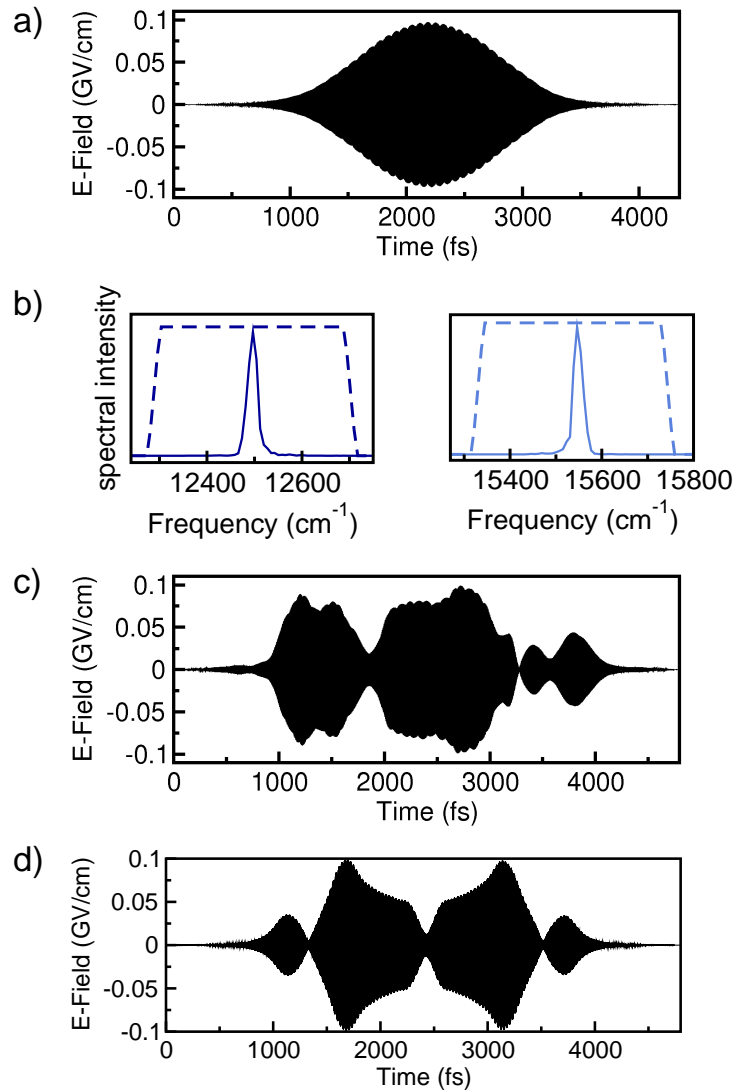


**Figure 2.8:** The non-resonant Raman fields  $\varepsilon_1(t)$  acting as quantum logic operations are depicted. The corresponding laser fields  $\varepsilon_2(t)$  have the same envelope functions, but different carrier frequencies. a) Global CNOT gate laser field. b) Spectra of both CNOT fields with their band-pass functions (dashed lines). c) Laser field for the global NOT gate and d) for the global Hadamard operation.

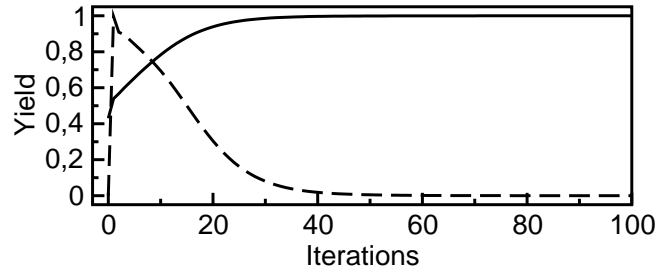


**Figure 2.9:** The solid line indicates the convergence of the modified OCT algorithm after the total time  $T$  (determined by the yield  $\sum_{k=1}^4 \frac{1}{4} \langle \Psi_{ik}(T) | \Psi_{fk}(T) \rangle$ ) during the optimization. The amount of the suppressed frequency components during the optimization is shown by the dashed line (scaled to one).

to a maximum of less than 1 % of the pulse energy, but converges to zero, while reaching the optimization aim.

## 2.4 Application prospects of bandwidth-limited OCT

In general, OCT as the theoretical counterpart to OCEs is a powerful method for the prediction of pulse structures as an initial guess and guidance for OCE. With OCT, insight into the quantum pathways of these processes is directly available and the numerous applications range from the control of chemical reactions in gas and condensed phase [114, 115] to the control in nanostructures [116, 117] and to quantum optical problems like quantum information processing [7, 67, 118, 119] or the preparation of cold molecules [104, 120]. However, one fundamental difference between OCE and OCT is the spectral bandwidth of the laser field, inherently present in the experiment but in principle unlimited in the original OCT formulation. The general comparability of experimental and theoretical results may be complicated, since the theoretical answer for the optimal pulse can always span a wide bandwidth with quantum pathways out of experimental reach.

The presented frequency filtering OCT algorithm [111] is the first method,

which allows for the treatment of the time and the frequency domain on an equal footing in OCT calculations, while preserving the monotonic convergence and universal applicability. It guarantees a close link to learning loop control experiments and offers an elegant possibility to study OCEs theoretically by explicitly including the experimental feature of the limited spectral bandwidth as a constraint.

The optimized non-resonant Raman quantum gates demonstrate the power of the presented method, but are only one of the possible applications of the frequency filtering OCT scheme. The control of other multi-color, multi-photon processes with ultrashort laser pulses is now accessible. Additionally, the applications of the new method can be easily transferred to various problems, covering a wide range of physics. For control tasks beyond the typical molecular physics area, such as the preparation of cold molecules by photo-association [104], atom transport in optical lattices [121], fast and robust gate operations with trapped ions [122] and NMR qubits [123] and voltage waveforms for transport sequences in ion traps [124], frequency filtering becomes a crucial requirement to predict realizable control functions. In general, the simplification of theoretical control functions, such as pulse shapes for the experiment can be achieved.

## **2.5 Conclusion**

A new realization strategy for the concept of molecular vibrational quantum computing has been presented by the implementation of simple structured, non-resonant stimulated, Raman quantum gates of high efficiencies [111]. Thereby, vibrational quantum computing in the ground state is transferred for the first time to the 800 nm regime, which is well established and accessible for pulse shaping techniques.

For the optimization of the non-resonant Raman quantum gates, a Krotov OCT approach has been developed, which treats time and frequency domain equally, thus, unifying global optimal control with spectral constraints. The new tool optimizes laser fields under realistic experimental spectral conditions. Optimal laser fields and control pathways in the experimentally accessible search space are predictable now. Additionally, an arbitrary pattern can be imprinted on the selected frequency range to suppress or enhance distinct quantum pathways. Thus, a strong and direct link to OCE is provided. The method has been

successfully demonstrated for a non-resonant multi-photon process, but can also easily be transferred to linear processes.



# 3 Control of vibrational quantum processes with genetic algorithms

OCT [96, 97, 6] and OCEs [81, 87] have been successfully demonstrated for numerous applications in molecular physics, driving control processes with modulated laser pulses. However, the underlying search strategies differ, while OCT operates in the time domain, OCE optimizes the laser fields in the frequency domain. This implies that both search procedures experience a different bias and follow different pathways on the search landscape. A clear advantage of OCT is the possibility to strictly limit the laser-molecule interaction time, which is important, especially in the condensed phase, where decoherence sets an upper limit for the temporal control window. In the parameter space of OCT, it was possible for different control tasks [7, 111] to find a subspace of high-efficiency solutions with simple structured laser fields, providing robust mechanisms.

In recent years, coherent control of molecular vibrational excitation with shaped mid-IR pulses has been achieved [72, 125, 126, 71, 91]. Additionally, first methods of direct pulse shaping in this frequency regime have been developed [70, 68, 69]. This allows, together with the possibility to follow the population transfer induced by the modulated pulses [70], for the first experimental implementation of quantum logic operations realizing molecular vibrational quantum computing operating on IR active modes.

Inspired by these recent developments, the question is investigated of whether and how OCE results can be traced in the OCT solution space of simple structured and short laser pulses. The focus is on similarities and differences of GA and OCT searches and solutions found. Based on knowledge from previous OCT studies, the aims are simple and robust GA solutions. This will enable the prediction of a promising and concerted search strategy and for optimal solutions within the control space of the experiment.

The control and optimization prospects in the frequency domain are studied theoretically, using a GA and shaping FL pulses. The results are discussed

in comparison to OCT solutions and the possible overlap of OCE and OCT solution subspaces is explored. Strategies to approach OCT solutions in OCE searches, based on GA for amplitude and phase modulation, are investigated and presented. In the theoretical simulation, the experimental constraints, e.g. the incident pulse duration, the carrier frequency, the maximum energy and the properties of the mask functions, can be met and conserved in the beginning and during the optimization.

The objectives of this study are state-to-state transitions and unitary transformations, within the scope of vibrational excitation of transition metal carbonyls. Previous theoretical studies [50, 52, 51] already proposed transition metal carbonyls, and in particular  $\text{MnBr}(\text{CO})_5$ , as favorable candidates for the realization of molecular quantum computing with vibrational IR qubits. Additionally, many experimental studies illustrate the suitability of such complexes for photo-physical investigations [127, 128, 129, 130, 131] and recent experiments on coherent control of  $\text{W}(\text{CO})_6$  [70] provide the opportunity to check the consistency of theory and experiment. The possibility to optimize vibrational quantum gate operations with GAs theoretically, has been demonstrated previously [59, 62] for small molecules.

Analogously to experimental closed loop setups, the application prospects of two different implementations of the phase function are investigated, a pixelated phase variation and a sinusoidal phase modulation. The approach based on analytic, parametrized phase forms was introduced in the experiment to decrease the complexity of the shaped pulses and to facilitate the interpretation of OCEs [132]. The control landscape generated by the parametrized phase functions are examined and the underlying mechanisms clarified. Strategies to decrease the complexity of pulse shapes gained from the pixelated mask function approach are developed. They benefit from previous OCT calculations. Additionally, the capabilities of the experimental GA search are extended by optimizing the FL pulses with the GA simultaneously to the phase and transmittance functions. The most promising FL pulse properties and mask functions for future quantum control experiments can be predicted from these calculations.

## 3.1 Model systems and computational details

The objectives of this study are vibrational state-to-state transitions and unitary transformations for the two metal carbonyls  $\text{W}(\text{CO})_6$  and  $\text{MnBr}(\text{CO})_5$ .

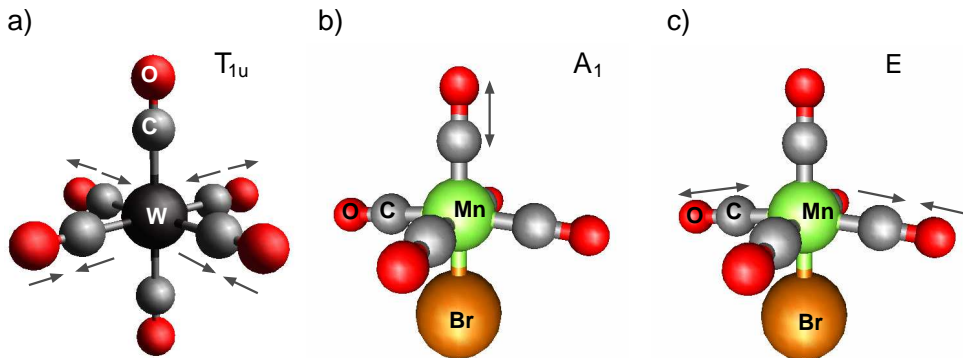


**Figure 3.1:** IR active normal mode vibrations used for the implementation of state-to-state transitions and unitary transformations. a)  $T_{1u}$  mode of  $W(CO)_6$ . b)  $A_1$  mode of  $MnBr(CO)_5$ . c)  $E$  mode of  $MnBr(CO)_5$ .

The control investigations are performed for strongly IR active C-O stretching normal modes of the metal carbonyls, the  $T_{1u}$  mode of  $W(CO)_6$  [Fig. 3.1 a)] and the  $E$  and  $A_1$  mode of  $MnBr(CO)_5$  [Fig. 3.1 b) and c)]. The potential energy curve of the  $T_{1u}$  mode of  $W(CO)_6$  and the corresponding dipole moment are calculated quantum chemically [108] with density functional theory (b3lyp/6-31G\*, LanL2DZ for W), in case of the  $MnBr(CO)_5$  see [50]. The vibrational eigenfunctions are explicitly calculated by a relaxation method (Sec. 1.1.3), the dipole matrix elements are evaluated and the Hamiltonian is set up in the eigenstate representation. In case of the molecule  $W(CO)_6$ , the vibrational eigenstates from the transient spectrum [70] are used to simulate the experimental conditions accurately, the energy of the higher lying vibrational levels are extrapolated with the anharmonicity traced from the spectrum. The time propagation is performed with the SPO technique (Sec. 1.1.2). For the quantum gate calculations the vibrational ground state is defined as the qubit state  $|0\rangle$  and the first vibrational excited state as  $|1\rangle$ .

The shaped laser fields, driving the desired vibrational quantum processes are optimized similar to the closed loop technique, which is often pursued in experiments and sketched schematically in Fig. 3.2. The incident, FL pulses are characterized by the carrier frequency  $\omega_c$ , the FL pulse duration  $\tau_p$  (FWHM) and the maximum intensity  $\varepsilon_0$  as given in Eq. 1.50. With the shaping device a phase and a transmittance function is impressed on a FL pulse spectrum

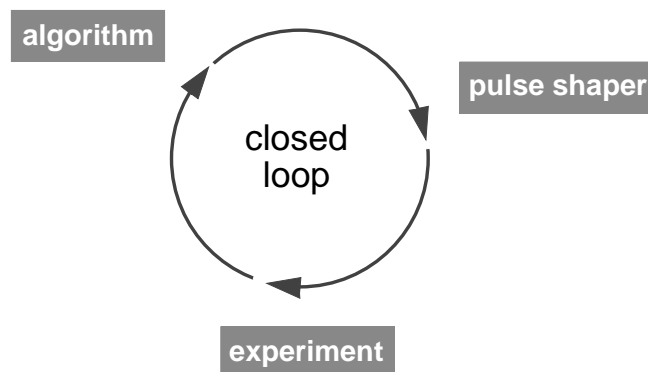


**Figure 3.2:** Schematic sketch of the closed loop setup in OCEs.

according to Eqs. 1.52 and 1.54. The phase functions used in this study are either parametrized sinusoidal functions as given in Eq. 1.55 or pixelated mask functions (phase and transmittance) are used. The modulated field is then applied on the sample in the experiment or in this theoretical study the molecular system is propagated under the influence of the time-dependent electric laser field and the quantum yield of the process is calculated afterwards. This data is returned to the optimization algorithm, where a steady-state GA from the GALib genetic algorithm package [95] is applied in this study. It replaces only the individuals with the lowest fitness by offspring. As an advantage, good solutions remain in the population for more iterations. The phase and transmittance functions are now optimized by the GA operators, borrowed from Darwinian evolutionary theory, to increase the efficiencies of the control processes iteratively.

In optimal control calculations [96, 97, 6, 7], pulse parameters are entered in terms of a guess laser field, but they are not binding for the formalism and are generally altered during the optimization, except of the pulse duration. OCT-specific parameters, which need to be chosen initially, are a penalty factor for the restriction of the pulse energy and a shape function, to ensure a smooth switching on and off behavior of the pulse intensity (Eq. 1.60). For the GA, one has to specify the FL pulse parameters, the number of pixels and the pixel width explicitly. These parameters stay fixed during the optimization. Solutions for the selected FL pulse and pixel properties are generated exclusively. Whereas, in OCT the required properties of the FL pulses can be deduced from the optimal laser field ([92], Eq. 1.67) and can vary for runs with different penalty factors.

Additional GA-specific input data are the mutation rate, the crossing-over rate, the replacement factor, the population size and the sampling of the shaper. The parameters 0.33 for the replacement rate, 0.05 for the mutation rate and 0.95 for the crossover rate are used.

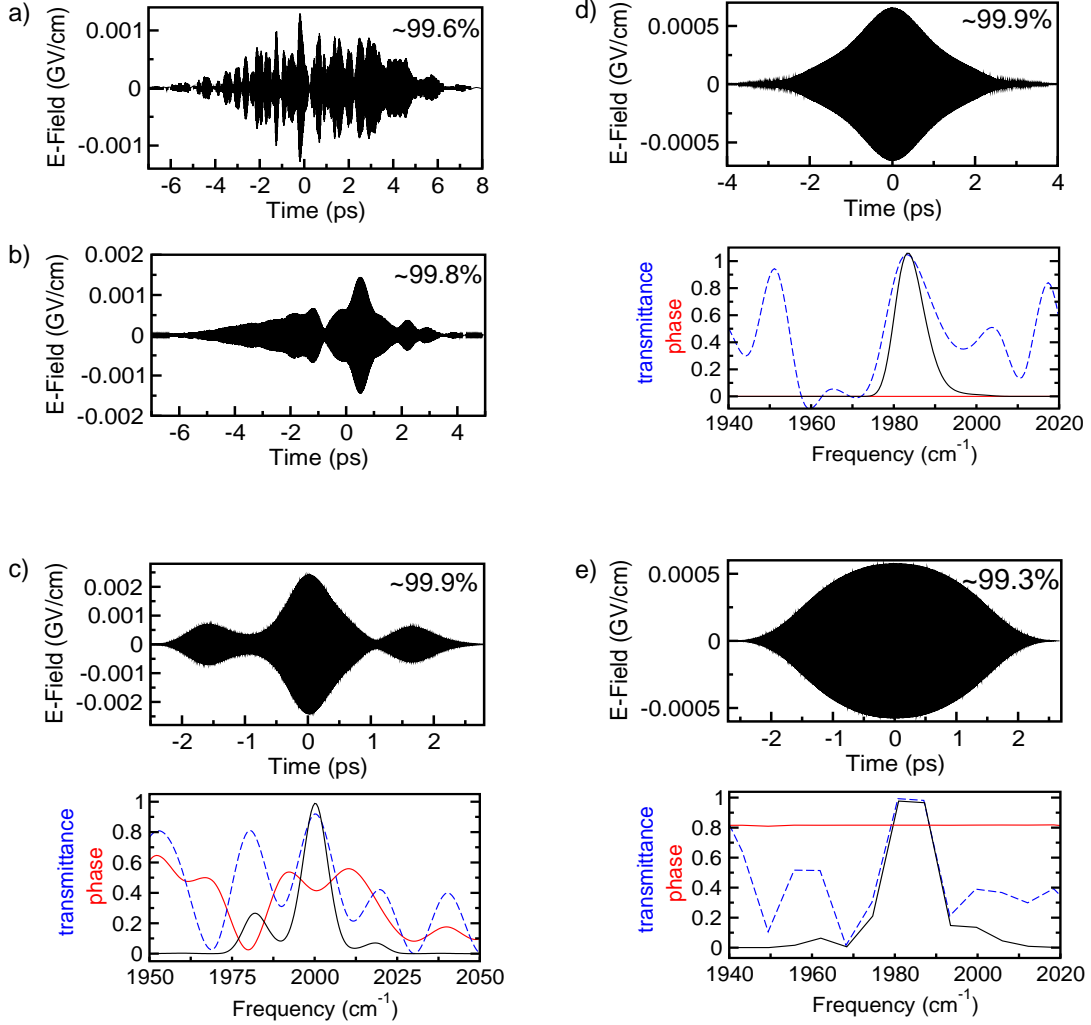


**Figure 3.3:** From a) to d): NOT gates optimized with a GA. c), d) Lower panels: scaled spectra (black line), phase (red line) and transmittance (blue line) functions. Due to the cubic spline interpolation the transmittance might slightly overshoot the range  $[0, 1]$ , this should not affect the validity of the results. e) OCT result for the NOT gate.

## 3.2 Results and discussion

The results for the state selective excitation of the  $T_{1u}$  of  $W(CO)_6$  analogously to the experiment [70] are investigated. Additionally, quantum gates are optimized for the metal carbonyls with sinusoidal phase functions and pixelated mask functions and both approaches discussed. Strategies, based on the knowledge from previous OCT calculations, are used and lead to simplifications of the resulting laser fields.

### 3.2.1 NOT gate: $T_{1u}$ mode of $W(CO)_6$

The first optimization aim is a NOT gate operation, switching the qubit basis states  $|0\rangle \leftrightarrow |1\rangle$  for the qubits encoded in a  $T_{1u}$  normal mode of  $W(CO)_6$ . The pixelated phase  $\phi(\omega)$  and transmittance functions  $T(\omega)$  are optimized with a spectral pixel resolution of  $10\text{ cm}^{-1}$ . The FL pulse parameters are given in Tab. 3.1, first row. The best individual yields an efficiency of 99.6% and a

$\tau_p$ [fs]	$\varepsilon_0$ [au]	$\omega_c$ [ $\text{cm}^{-1}$ ]
105	0.002	2000
480	0.001	2000
700	0.0003	2000

**Table 3.1:** FL pulse properties for NOT gates.

rather complex envelope function, depicted in Fig. 3.3 a). Similar structures of highly efficient quantum gates have been reported earlier for different molecules [59, 63, 62]. For more robust laser fields, the focus is on the simplification of such pulses, in favor of adiabatic state switching and low field intensities. From OCT, a certain tendency to longer FL pulses for gate operations in the carbonyl complexes is known. Consequently, the FWHM of the FL pulse is increased and the parameters given in Tab. 3.1, second row, are used. A clear simplification of the envelope function results with a shorter time duration and the laser field consists only of a few subpulses [Fig. 3.3 b)]. In previous OCT work [52], the variations within the phase functions were very small. Thus, assumingly the envelope functions can further be simplified when additionally the maximum phase variation is limited, i.e. the co-domain is decreased from  $[0, 2\pi]$  to  $[0, 0.1 \cdot 2\pi]$ . The result is shown in Fig. 3.3 c), upper panel, in the time

domain and in the lower panel, in the frequency domain, the envelope reveals three subpulses.

For comparison, a corresponding OCT calculation was performed, where a total pulse duration of 5.3 ps was used for the shaped OCT pulse and a penalty factor  $\alpha = 200$ . The resulting, highly efficient NOT gate laser field (99.3 %) is presented in Fig. 3.3 e), together with the calculated spectrum (black line) and mask functions [phase: red line, transmittance: blue line, both not interpolated, spectral pixel width  $< 7 \text{ cm}^{-1}$ , lower panel of Fig. 3.3 e)]. The field is almost completely amplitude modulated, but not phase-shaped. The FWHM of the corresponding FL pulse is elongated to 825 fs and the spectrum is centered at the fundamental transition frequency ( $1983 \text{ cm}^{-1}$ ).

The FL pulse derived from the OCT result is employed as incident pulse for further GA calculations and a spectral pixel width of  $6 \text{ cm}^{-1}$  is used. First, the co-domain of the phase function is confined to a minimum range of  $[0, 2\pi] \cdot 0.01$ . The resulting NOT gate (not shown here) is also highly efficient, however, the phase is still varying and the GA fully uses the available range, the phase function is limited to. Statistically, varying phases are much more probable than constant phase functions in GA optimizations. As these fluctuating phase functions already give good solutions, the GA has no bias for flat phase functions. No correlation is imposed on the phase values of the pixels to enforce constant phase functions, as in case of OCT, where this is indirectly implemented by the use of high penalty factors  $\alpha$ . Thus, the OCT optimization explores and converges in a different part of the search space compared to theoretical and experimental GA applications. Ultimately, only amplitude shaping of the OCT FL pulse is allowed in the GA search and the resulting field is shown in Fig. 3.3 d). An efficiency exceeding 99.9 % is reached, and the GA finds a solution very close to the OCT result. The laser fields mainly differ in the duration, as the GA offers no time constraint for the optimized pulse [Fig. 3.3 d), e), upper panels]. Although, limitations on the phase range lead to simplified control fields, more demanding control tasks will require some flexibility in the phase function [52].

The strategy of elongated FL pulses and a limited co-domain of the phase function, is also attempted for a Hadamard operation. A spectral pixel resolution of  $10 \text{ cm}^{-1}$  is used and the parameters for the FL pulse are given in Tab. 3.1, third row. For high quantum yields the boundaries of the phase variation must be relaxed to  $[0, 2\pi] \cdot 0.5$  and efficiencies exceeding 99.4 % are obtained (Fig. 3.4).

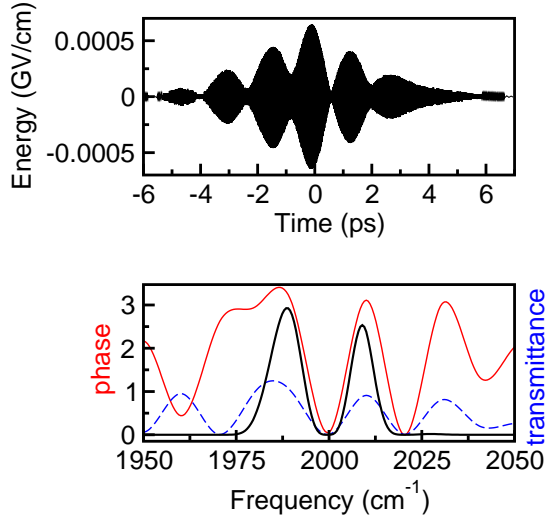


**Figure 3.4:** Upper panel: Hadamard gate, lower panel: scaled spectrum (black line), phase function  $\phi(\omega)$  (red line) and the transmittance function  $T(\omega)$  (blue line).

### 3.2.2 Objective with a cost function

Purely pixel-based GA optimizations yield complex field structures for unitary transformations. Simplifications of pulse structures can be achieved when the knowledge from OCT results is used, i.e. simple solutions can be found within the search space of the GA. As OCT results are not always available, a favorable alternative is to extend the objective by a cost function, analogously to OCT. In Sec. 3.2.1, the objective was simply defined by the efficiency of the population transfer:

$$O = \frac{1}{N} \sum_{k=1}^N |\langle \Psi_{ik}(T) | \Phi_{fk} \rangle|^2, \quad (3.1)$$

with each of the  $k$  wave functions  $\Psi_i(T)$  propagated to the final time  $T$  and the target states  $\Phi_f$ . The field intensity weighted by a penalty factor  $\alpha$  is now subtracted from the overlap term:

$$O = \frac{1}{N} \sum_{k=1}^N |\langle \Psi_{ik}(T) | \Phi_{fk} \rangle|^2 - \alpha \int_0^T \varepsilon(t)^2 dt. \quad (3.2)$$

Consequently, efficient laser fields with low intensities dominate the ones with high intensities. For a mask function with a spectral pixel resolution of  $10 \text{ cm}^{-1}$

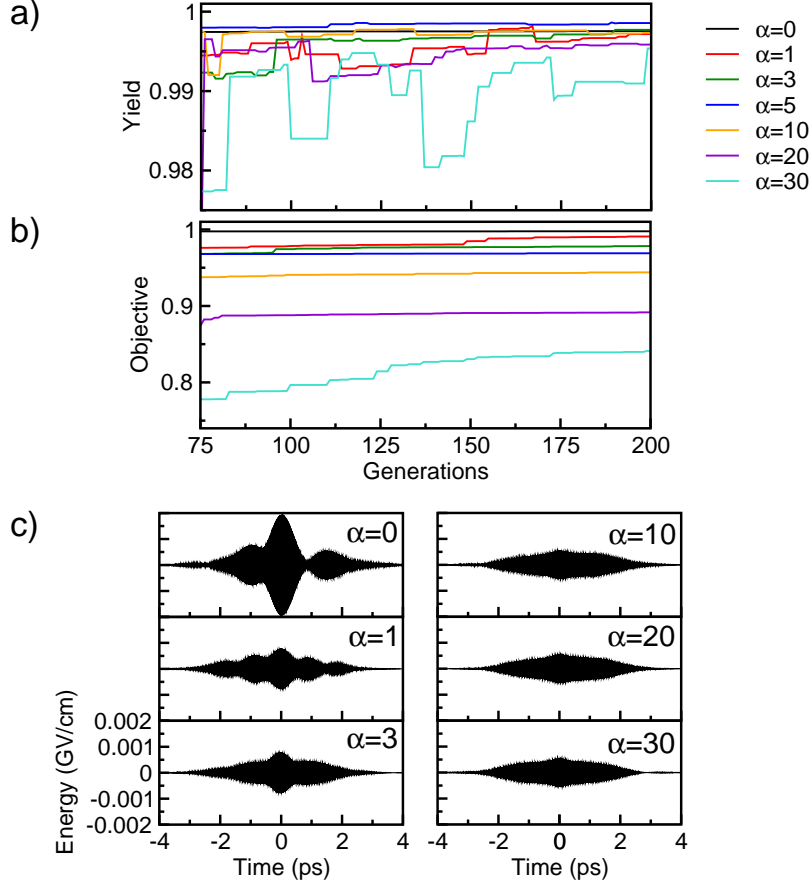


**Figure 3.5:** a) Convergence of the quantum yield and b) of the objective function for different  $\alpha$  values. c) Optimized laser fields for different  $\alpha$  values.

and the FL pulse parameters given in Tab. 3.2, the penalty factor  $\alpha$  is scanned exemplarily for the state-to-state transition  $0 \rightarrow 1$  [Fig. 3.5 a) and b)].  $\alpha$  is given in atomic units, referring to the variables  $\varepsilon(t)$  and  $t$  also used in atomic units. Accordingly with ascending values of  $\alpha$ , the maximum objective reached, decreases and the monotonic convergence of the GA runs slightly vanishes [Fig. 3.5 b)]. Still, control efficiencies above 99 % are reached up to a value of  $\alpha = 20$  and the monotonic convergence stays mostly acceptable [Fig. 3.5 a)]. The resulting envelope functions [Fig. 3.5 c)] more and more resemble each other with increas-

$\tau_p$ [fs]	$\varepsilon_0$ [au]	$\omega_c$ [cm <sup>-1</sup> ]
725	0.001	2000

**Table 3.2:** FL pulse properties for a GA search with a modified objective function.

ing  $\alpha$  and it can be deduced that the GA is guided towards similar pathways to achieve the optimization aims.

Equivalently to the energy cost function, population in distinct vibrational levels (e.g. overtone states) or the complexity of the envelope can be incorporated.

### 3.2.3 Phase modulation in analytic form

The exclusive application of analytic phase functions emerged from the aim to reduce the complexity of the shaped laser fields and to understand the underlying mechanisms [85, 132, 133]. In OCT, it is neither possible to address the phase function of the laser fields directly, nor can analytic expression be defined. In the GA scheme this is straightforward to implement.

#### State-to-state transition in the $T_{1u}$ mode of $W(CO)_6$

##### The control landscape for multipulses

The state-to-state transition  $0 \rightarrow 1$  in the  $T_{1u}$  mode of  $W(CO)_6$  is optimized with a sinusoidal phase modulation following the experiment [70]:

$$\phi(\omega) = \sum_i a_i (\sin b_i \omega + c_i), \quad (3.3)$$

where  $i = 1$  and  $c_i = 0$  is used. Analogously to the experiment, no transmittance function is employed. The FL pulse properties are given in Tab. 3.3. The resulting multipulses are characterized by the phase parameters  $a_i$  and  $b_i$ . The control landscape is investigated by scanning the influence of these parameters ( $a_1 = a$  and  $b_1 = b$ ) on the quantum efficiency (Fig. 3.6), where  $a$  is dimensionless and  $b$  is a time, given in atomic units. Sections of the control landscape are shown in Fig. 3.6 for the large parameter range  $a$ : [0.6, 2.4] and  $b$ : [20000, 40000], the smaller inset shows an enlarged upper part of the control

$\tau_p$ [fs]	$\varepsilon_0$ [au]	$\omega_c$ [ $\text{cm}^{-1}$ ]
212	0.001	1983

**Table 3.3:** FL pulse properties for analytic phase functions.

surface. The landscape is characterized by a high periodicity along  $b$ , with efficiencies ranging from 0% to 90%. The variation along  $a$  is significantly lower and thus  $b$  is the dominant control parameter.

The phase parameter  $a$  is the modulation depth, which determines the relative intensity of the single subpulses. The modulation time  $b$  defines the temporal shift between the individual subpulses. The temporal pattern of the CEP of the individual subpulses is constant for a given  $c$  value. For  $c = 0$  the CEP shift from subpulse to subpulse is  $\pi$  in the first half of the pulse sequence and zero in the second half [Fig. 3.7 a), upper panel, dashed line]. This pattern is

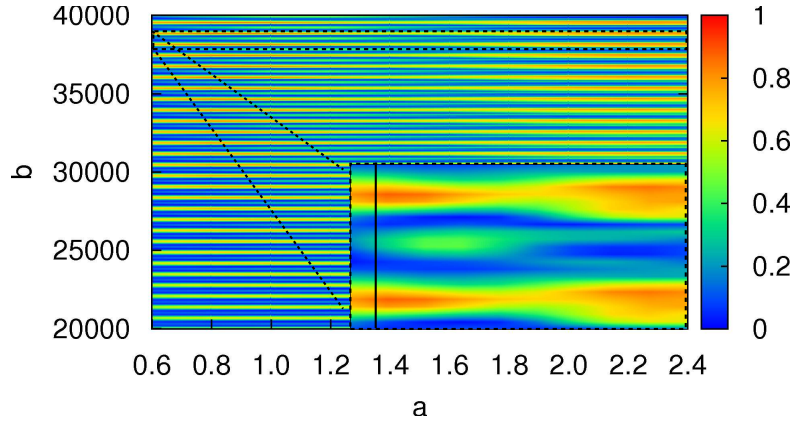


**Figure 3.6:** Control landscape for the quantum yield as a function of the phase parameters  $a$  and  $b$  for the transition  $0 \rightarrow 1$  calculated for the ranges  $a : [0.6, 2.4]$  and  $b : [20000, 40000]$ . The inset shows an enlarged part of the surface.

not affected by variation of  $b$ . However, depending on  $b$ , an optical phase jump occurs between the subpulses, due to the combination of the fixed CEP pattern and the varying temporal shifts. The range of the optical phase jump  $[0, 2\pi]$  corresponds to an oscillation period of the carrier frequency  $\omega_c = 1983 \text{ cm}^{-1}$

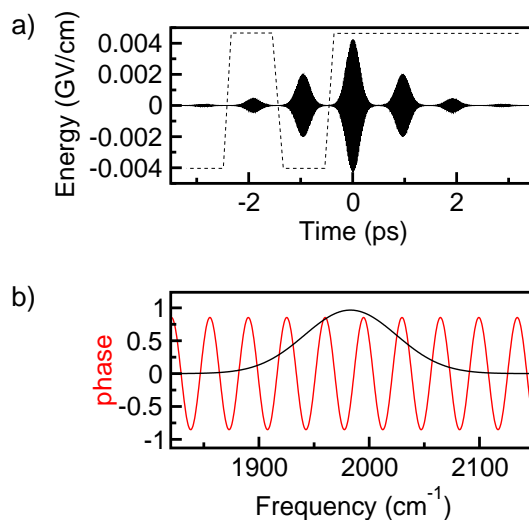


**Figure 3.7:** a) Multipulse generated with a sinusoidal phase modulation. The dashed line shows the corresponding CEP pattern. b) The scaled spectrum (black line) and the sinusoidal phase function (red line) is depicted.

and is reflected in Fig. 3.6 in the periodicity of the control surface (a difference of  $\Delta b \sim 700$  au between the high-efficiency regions equals  $\sim 16.82$  fs).

### Mechanisms induced by multipulses

The phase effects on the population transfer mechanism  $|0\rangle \rightarrow |1\rangle$  are discussed exemplarily for a cut along the control surface marked in Fig. 3.6 by the vertical line in the smaller inset ( $a = 0.8$  and  $b: [38000, 39000]$ ). In Fig. 3.8 the change in population of the states 0 [Fig. 3.8 a)] and 1 [Fig. 3.8 b)] are plotted as a function of time and of  $b$ . For three  $b$  values ( $b \sim 38200, 38550, 38900$ ) the initial state 0 is almost completely depopulated, but only in two cases ( $b \sim 38200$  and  $b \sim 38900$ ) the population is transferred into the target state 1. Two values (marked as black arrows) are selected, one which leads to a high and one which leads to low transfer efficiency into state 1. Their individual mechanisms are shown in Fig. 3.9. The black line corresponds to the initial state 0, the red line to the target state 1 and the green line to the overtone state 2. Also included are the corresponding laser fields and the optical phase jumps (in units of  $\pi$ ) between the single subpulses. A  $b$  value of 38900 induces a phase jump of  $1.9\pi$ .

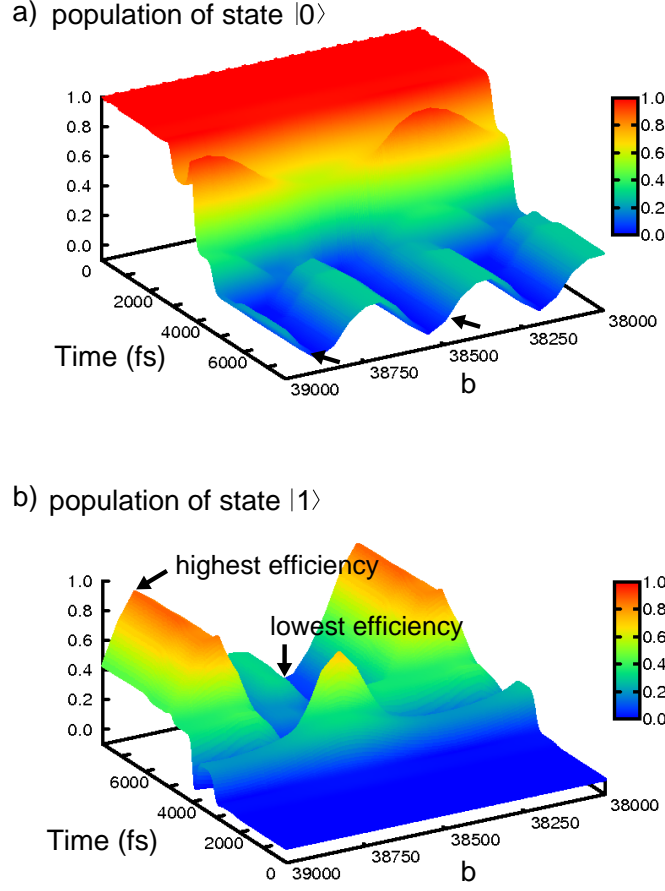


**Figure 3.8:** Population transfer mechanisms for the excitation  $0 \rightarrow 1$  with the phase parameters  $a = 0.8$ ,  $b: [38000, 39000]$ . Progression of the population a) in state 0, b) in state 1. The time axis point in opposite directions for better visibility.

In the first half of the pulse sequence an optical phase jump of  $0.9\pi$  results as the combination of the  $b$  induced phase jump and the CEP shifts from subpulse to subpulse. Since there are no CEP shifts in the second part, the optical phase jump is here  $1.9\pi$ . From the transfer mechanisms [Fig. 3.9 a)], it can be deduced that the first optical phase jumps of about  $\pi$  lead to subpulses, which reverse the action of the preceding pulse. See e.g. the action of the subpulse at  $t = 3000$  fs or even more pronounced for  $t = 3900$  fs. This finding is general for

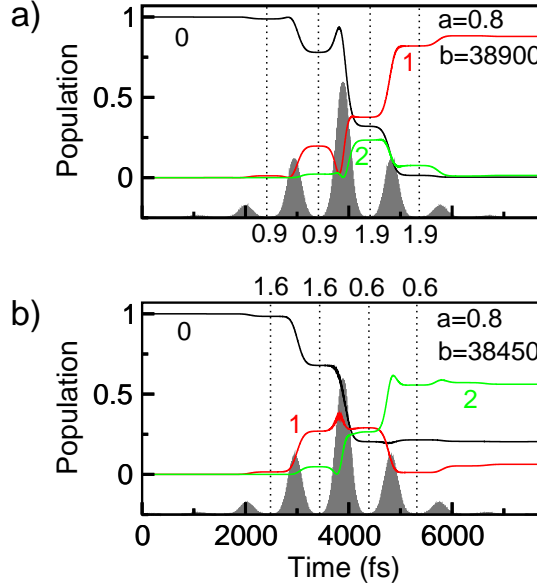


**Figure 3.9:** Mechanisms, scaled laser envelopes and phase shifts for two selected sets of phase parameters. a)  $a = 0.8$ ,  $b = 38900$ , b)  $a = 0.8$ ,  $b = 38450$ .

all subpulses with optical phase jumps of  $\pi$  and is more effective, the closer the optical phase jump is to  $\pi$ . These optical phase jumps are most effective when the carrier frequency of the laser is in resonance with the transition energy. In the present study, the laser is tuned to the  $0 \rightarrow 1$  transition, thus all overtone transitions (such as  $1 \rightarrow 2$ ) are less affected.

The main subpulse [Fig. 3.9 a), upper panel] starts to depopulate the target state again. Due to the higher intensity, the target state is repopulated afterwards by the remaining pulse. For the next subpulse (second half of the pulse sequence), the optical phase jump is almost  $2\pi$  and the population transfer into the vibrational state 1 is continued, whereas the overtone state 2 is depopulated. The same holds for the last subpulse. From the control landscape (Fig. 3.6) and the mechanisms discussed (Fig. 3.8), it can be concluded that the best results are reached for the given setting (i.e. molecular and FL pulse properties) for optical phase jumps close to  $\pi$  in the first half of the pulse sequence and close to  $2\pi$  in the second half. If  $b = 38450$  [Fig. 3.9 b)] optical phase jumps of  $1.6\pi$ , and  $0.6\pi$  are obtained. In this case, neither a reversal of the excitation process,

nor a continuation takes place. Instead, the net transfer in the first vibrational excited state is almost zero, while the overtone state is populated.

Analogously, the complete control landscape depicted in Fig. 3.6 with respect to the periodicity in  $b$  can be understood. A deviation of its structure will only emerge when a parameter  $b$  is selected, which leads to subpulses overlapping in time.

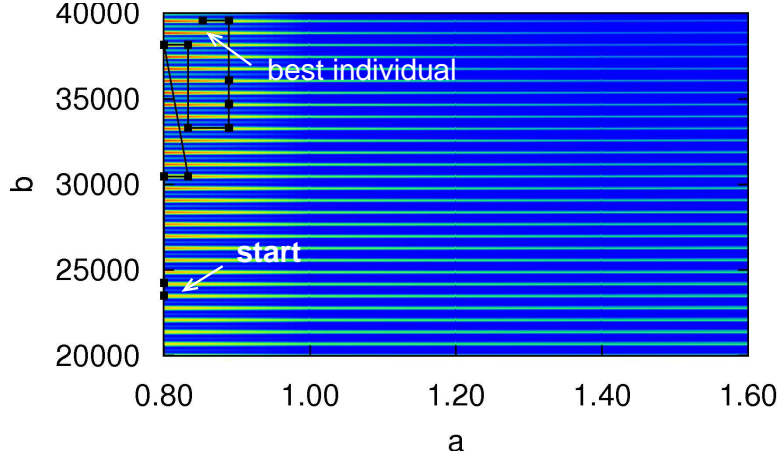


**Figure 3.10:** Control landscape for the quantum yield as a function of the phase parameters  $a$  and  $b$  for the transition  $0 \rightarrow 1$ : in the range  $a : [0.8, 1.6]$  and  $b : [20000, 40000]$  calculated with the pulse duration as cost function (Eq. 3.4). The search path of the GA run is indicated by the black dots.

### Pulse duration as cost function

Variation of the parameter  $a$  determines the relative intensity of the single subpulses. Large  $a$  values increase the effective number of subpulses and equivalently the pulse duration. Such GA results would be unfavorable when time limitation is required to protect the coherence of molecular processes. Therefore, a cost function is included within the objective function to confine the pulse duration:

$$O = \frac{1}{N} \sum_{k=1}^N |\langle \Psi_{ik}(T) | \Phi_{fk} \rangle|^2 - \alpha_{\tau} \tau. \quad (3.4)$$

For  $\tau$  the FWHM of the shaped pulse is used in atomic units and the penalty factor  $\alpha_\tau = 0.00025$  (units  $1/t$  [au]). The structure of the control landscape changes (Fig. 3.10) as the algorithm is forced to converge to a subspace with shorter durations, recognizable by the lighter areas (from yellow to red) in Fig. 3.10. As can be traced from the GA run, the best result (88.4%) within the parameter range  $[0.0, 2.4]$  for  $a$  and  $[20000, 40000]$  for  $b$  is found after a few generations. The dots mark the best individuals of the generations and the line maps the GA search path on the landscape. The corresponding best laser field, its spectrum and phase function is depicted in Fig. 3.7.

### NOT gate in the $T_{1u}$ mode of $W(\text{CO})_6$

Starting with the FL pulse (Tab. 3.3), suited for the fundamental state-to-state transition, a NOT gate with a sinusoidal phase modulation is optimized and a slightly enlarged search space for  $b$ :  $[20000, 50000]$  is used. For this search space no high-efficiency solution of a NOT gate exists. The transition  $|0\rangle \rightarrow |1\rangle$  can be switched with an efficiency of 81.8%, but the reverse process only reaches 48.2%. The explanation can be given from the control landscapes of both processes (Fig. 3.11). Their periodicity is shifted by half an oscillation, i.e. a maximum for a  $|0\rangle \rightarrow |1\rangle$  transition matches a minimum or a secondary maximum condition for the  $|1\rangle \rightarrow |0\rangle$  process and vice versa. The mechanism reveals that good solutions for the process  $|0\rangle \rightarrow |1\rangle$  induce overtone transitions into the vibrational state  $v = 2$  when the laser field operates on state  $|1\rangle$  to reverse the switching. The best efficiencies for the reverse process  $|1\rangle \rightarrow |0\rangle$  are reached for a parameter  $b \sim 38550$ , where the optical phase jumps are  $\sim 2\pi$  ( $1.86\pi$ ) in the first part and  $\sim \pi$  ( $0.86\pi$ ) in the second part of the pulse sequence. The sequence of these optical phase jumps is exactly reversed to the progression required for the  $|0\rangle \rightarrow |1\rangle$  transition. Consequently, unitary operations cannot be realized by a simple sinusoidal approach for the phase modulation. Only when the distinct optical phase jumps are weakened can their implementation be successful.

A straightforward solution is to increase the summation over  $i > 1$  in Eq. 3.3. Thereby, the efficiency of the NOT gate can be raised to 95%, however, at the cost of higher complexity of the shaped laser fields. A new strategy is pursued to obtain efficient NOT gates with simple structures. Besides the phase parameters  $(a_i, b_i, c_i)$ , the FL pulse properties are included in the GA optimization

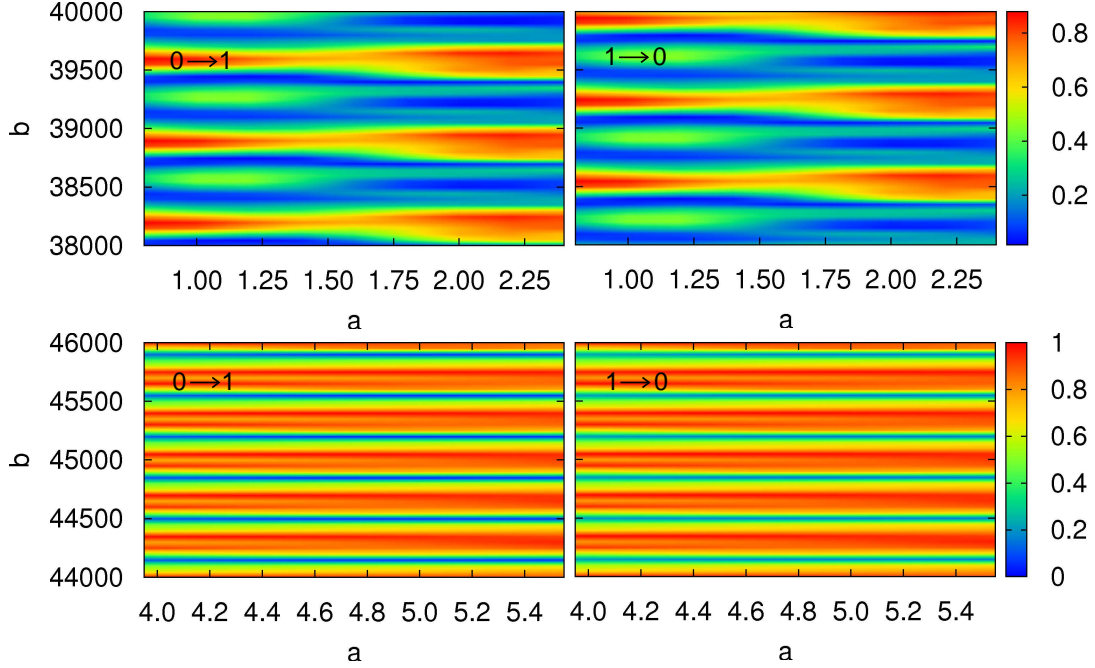


**Figure 3.11:** Control landscapes for the quantum yield as a function of the phase parameters  $a$  and  $b$  for both NOT processes  $|0\rangle \rightarrow |1\rangle$  (left) and  $|1\rangle \rightarrow |0\rangle$  (right). Upper panel:  $a$ :  $[0.8, 2.4]$ ,  $b$ :  $[38000, 40000]$ . The periodicity of the surfaces is shifted by half an oscillation. Lower panels:  $a$ :  $[3.95, 5.55]$ ,  $b$ :  $[44000, 46000]$ . The control landscapes for both switching processes match. The landscapes are evaluated for different FL pulses.

simultaneously, which is related to amplitude shaping. Hence, the genome of the GA is extended by the carrier frequency  $\omega_c$ , the maximum energy  $E_0$  and the FWHM of the FL pulse  $\tau_p$ . This approach increases the flexibility of the GA optimization beyond the experimental possibilities and guarantees that the full dimensionality of the defined control parameter space can be used, here on the basis of sinusoidal phase modulation.

For the five degrees of freedom, the parameter ranges are given in Tab. 3.4. As a result, a sinusoidal phase modulated NOT gate could be optimized with an efficiency exceeding 99.6% [Fig. 3.12 a)]. The resulting parameters are given in Tab. 3.4 and the control landscapes of both NOT processes are depicted in Fig. 3.11, lower panels. Now, the maxima on the control surfaces of both

parameter	min.	max.	GA result
$a$	0.0	5.0	4.75
$b$	20000	60000	44625
$\varepsilon_0$ [au]	0.0	0.01	0.00056
$\tau_p$ [fs]	0.0	2500	1504
$\omega_c$ [cm <sup>-1</sup> ]	1950	2050	1990.9

**Table 3.4:** Parameter ranges for the FL pulse properties and sinusoidal phase functions for a NOT gate.

processes  $|0\rangle \rightarrow |1\rangle$  and  $|1\rangle \rightarrow |0\rangle$  match. The significant change in the control landscapes (Fig. 3.11 upper and lower panels) arises from the combination of a rather narrow-band FL pulse and phase parameters, which lead to temporally overlapping subpulses (Fig. 3.11, lower panels) without pronounced optical phase jumps. As a consequence, the multipulse character vanishes. The variation of amplitude in combination with phase modulation seems to be essential to realize a unitary transformation.

### FL pulse optimization for the state-to-state transition in the $T_{1u}$ mode of $W(CO)_6$

The same optimization strategy is applied for the  $0 \rightarrow 1$  state-to-state transition. The corresponding parameters are given in the Tab. 3.5. The best result ( $\sim 94\%$ ) within 200 generations for a population size of 50 is shown in Fig. 3.12 b). The optimal pulse is very similar in shape to the laser field found in the experiment [70]. Also the excitation mechanism [Fig. 3.12 b), lower panel] provides the same features with the main part of population transferred by the second half of the multipulse. The explicit FL pulse and phase properties are given in Tab. 3.5. This good agreement for the pulse structure and mechanism shows that the presented approach is able to match the search spaces in theory and experiment and predicts that the highest possible transition rate will be obtained for a FL pulse with  $\tau_p = 215.8$  fs.

parameter	min.	max.	GA result
$a$	0.0	2.4	2.22
$b$	20000	50000	43140
$\varepsilon_0$ [au]	0.0	0.01	0.00107
$\tau_p$ [fs]	0.0	700	215.8
$\omega_c$ [ $\text{cm}^{-1}$ ]	1950	2000	1998.0

**Table 3.5:** Parameter ranges for the FL pulse properties and sinusoidal phase functions for a state-to-state transition.

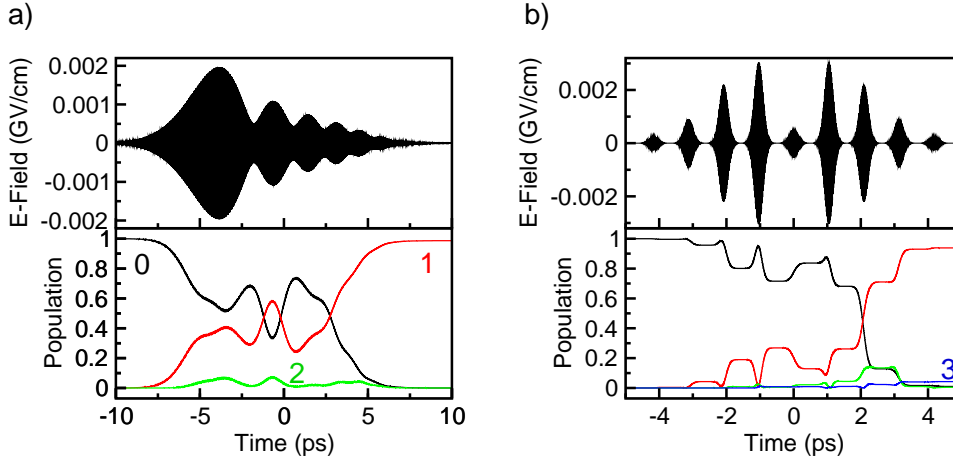


**Figure 3.12:** a) GA-optimized NOT gate and mechanism ( $0 \rightarrow 1$  transition).  
 b) Optimized pulse for the  $0 \rightarrow 1$  state-to-state transition in  $\text{W}(\text{CO})_6$  and mechanism. The black lines indicate the population in state  $|0\rangle$ , the red lines in state  $|1\rangle$  and the green (blue) in the overtone state  $v = 2$  ( $v = 3$ ).

### 3.2.4 Prediction of quantum gates for $\text{MnBr}(\text{CO})_5$

The GA optimization is extended to the two-qubit system  $\text{MnBr}(\text{CO})_5$ , for which a universal set of quantum gates with OCT was previously calculated [52]. The predicted, highly efficient quantum gates were simple structured and an interesting point is whether comparable solutions can be provided by the GA.

A universal set of quantum gates, with great importance attached to structural

simplicity, is optimized as benchmark for future experimental searches. The quantum gates involving population transfer (CNOT, NOT and Hadamard) are calculated explicitly. It is assumed that the  $\Pi$  gate is implemented by a time delay, which induces the correct phase rotation. Quantum gates, yielding phase correct target states, can be optimized either by maximizing the fidelity, defined as:

$$F = \frac{1}{N^2} \left| \sum_k^N \langle \Psi_{ik} | \Phi_{fk}(T) \rangle \right|^2. \quad (3.5)$$

Alternatively, one can optimize the population transfer only:

$$P = \frac{1}{N} \sum_{k=1}^N |\langle \Psi_{ik}(T) | \Phi_{fk} \rangle|^2, \quad (3.6)$$

and make use of the free phase evolution of the qubit basis states, i.e. append a phase gate. This is equivalent to a certain delay time of several femto- to picoseconds, in which the phase of each state evolves until the correct phase relation is reached at the end of the delay [49]. The second approach converges faster and corresponds to the direct, experimental observable. Exemplarily, the CNOT and NOT gates are depicted in Fig. 3.13, where the subscript E denotes that the gate is operating on the E symmetric mode and A on the  $A_1$  symmetric mode, respectively. These gates were optimized by maximizing the population transfer. A delay time will have to be attached to receive the correct phase relation. 15 pixels with a spectral width of  $5 \text{ cm}^{-1}$  for each pixel were used and the phase variation was confined to  $[0, 2\pi] \cdot 0.5$ , no further constraints were applied. These quantum gates (Fig. 3.13) operate very efficiently with a population transfer exceeding at least 99.0%. They are similarly simple structured compared to the OCT results [52] but clearly longer in duration as the defined phase space is again fully utilized, allowing for large amplitude modulations of the mask functions. In OCT calculations, the phase function cannot be addressed directly, however, the penalty factor together with the choice of the total laser-molecule interaction time can suppress unnecessary jumps in phase and/or transmittance.

For the CNOT<sub>E</sub> gate, also the fidelity of the process using a GA was maximized. The duration of the shaped pulse is determined by using a threshold value of  $5 \cdot 10^{-6} \text{ au} \approx 25 \cdot 10^{-6} \text{ GV/cm}$  of the electric field. The propagation

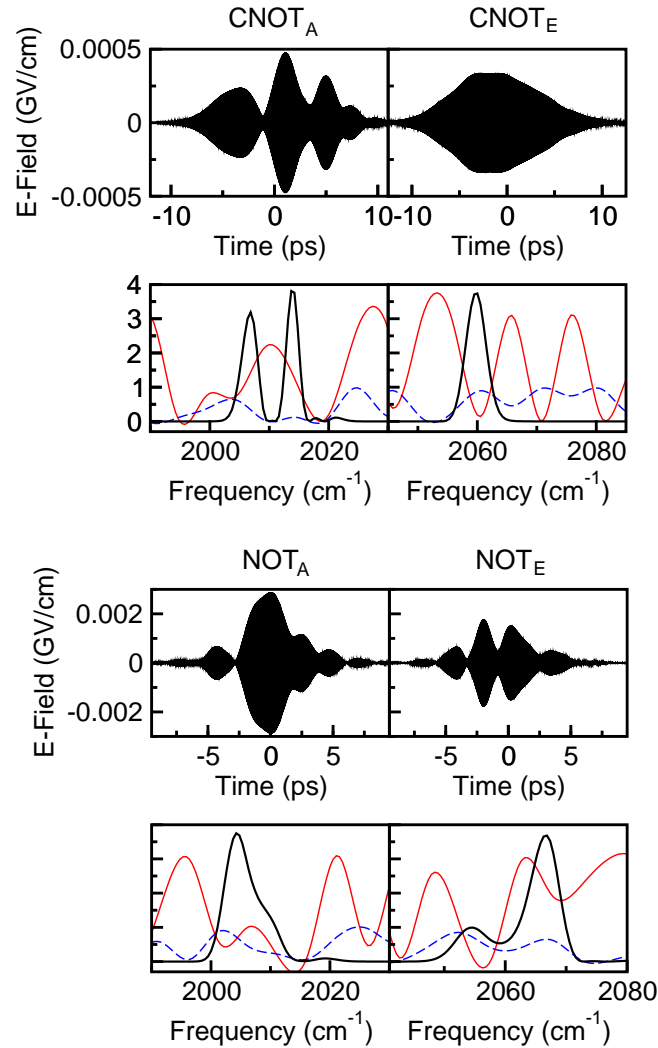


**Figure 3.13:** GA-optimized CNOT and NOT gates for  $\text{MnBr}(\text{CO})_5$ , operating either on the A, or on the E mode, with scaled spectra (black lines), phase functions (red lines) and transmittance functions (blue lines) depicted in the lower panels.

starts when this threshold is exceeded the first time. Equivalently, it ends when the value is reached the last time. At this final time, the fidelity of the whole process is calculated. In Fig. 3.14 a), a comparison of the convergence of both approaches, the maximization of the fidelity versus the population transfer, is

shown. The population size is 50 and the number of generations 1000. The GA run for the pure population transfer (red line) reaches an efficiency of over 99% after approximately 100 generations. The optimal quantum gate is depicted in Fig. 3.13. An additional delay time of  $\sim 4$  ps makes the CNOT gate phase-correct for use in quantum algorithms. In the second case [Fig. 3.14 a), black line], a maximum fidelity of  $\sim 97\%$  is reached after 700 generations. The slightly reduced fidelity is mainly due to an incomplete population transfer. Additionally, implementation prospects of pure sinusoidal phase modulation of

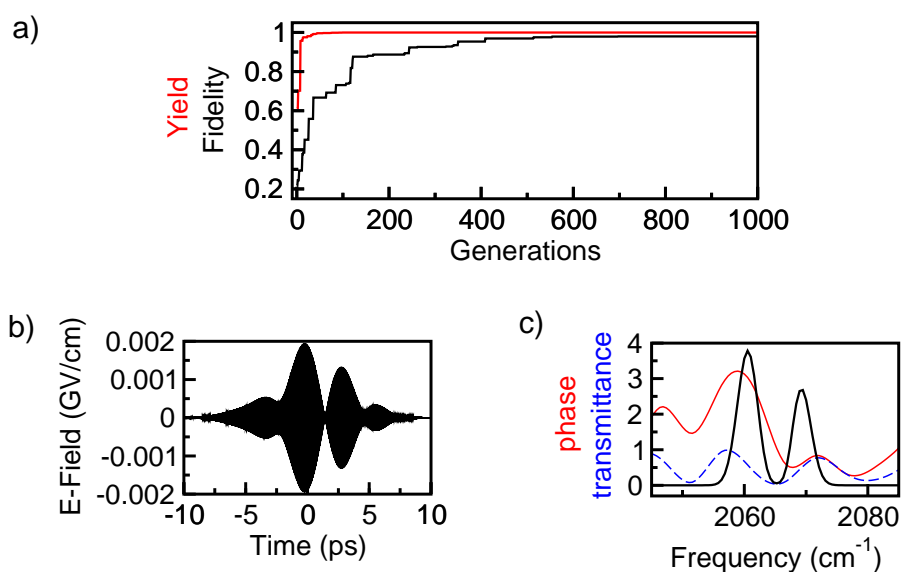


**Figure 3.14:** a) Convergence of the maximization of the population transfer versus the fidelity for the  $\text{CNOT}_E$  gate. Phase-correlated optimization of the CNOT gate: b) laser field, c) scaled spectrum (black line), phase (red line) and transmittance function (blue line).

two-qubit quantum gates were tested. In the multipulse parameter ranges, the efficiencies of the quantum gates cannot compete with free phase and amplitude modulated laser fields. Thus, for the experimental implementation of multi-qubit quantum gates, the more flexible approach of a pixelated mask functions is most promising. To avoid unnecessary complex pulse structures, it will be helpful to confine the co-domain of the phase to a limited range.

### 3.3 Conclusion

The differences originating from quantum control in the frequency domain by a GA and in the time domain by OCT are investigated. With a careful choice of the OCT-specific parameters, it is always possible in OCT calculations to find the simplest structured laser fields for high-efficiency solutions, which are probably the most robust ones. By default, a GA is used in closed loop experiments and its application in theoretical studies facilitates reliable predictions in the search space, strictly limited to the experimental parameters and their variation range. Pixel-based mask functions often lead to complex pulse structures with long pulse durations. In the GA search, approaches to decrease the complexity of the resulting pulse structures were introduced, borrowing concepts from previous OCT work. The studied objectives were state-to-state transitions and unitary transformations in the vibrational manifold of transition metal carbonyls. For pixelated phase and transmittance functions, longer FL pulses and the restriction of the co-domain of the phase function lead to simplifications of the pulse envelopes. Additionally, cost functions were implemented in the objective function, which can be used to reduce the field intensity or the pulse duration and guide the GA runs into distinct subspaces of simple structured and short results. Analogously, cost functions may be included, which decrease the complexity of the envelope function or the degree of the overtone excitation. For the GA runs with the modified objectives, solutions already approaching the subspace of optimal OCT results could be found.

Additionally, the effect of sinusoidal phase modulation, frequently used in experiment, omitting amplitude modulation, was investigated. The corresponding control landscape could be calculated and from its analysis one can derive the physical mechanism of the vibrational multipulse excitation. The laser fields and transfer mechanism obtained for the state-to-state transfer in  $\text{W}(\text{CO})_6$  agrees very well with the experiment [70]. The best, highly efficient solutions, were obtained when the FL pulses properties (carrier frequency  $\omega_c$ , maximum energy  $\varepsilon_0$  and FWHM  $\tau_p$ ) were optimized simultaneously. From the results, it can be predicted that multipulses are not suitable for the implementation of unitary transformations. This could easily be extracted by the analysis of the control landscapes. When the sinusoidal phase approach is used, an optimized FL pulse is essential for high efficiencies, i.e. a certain amount of amplitude shaping is required. In general, it was found that pixelated phase and transmittance functions

will lead to higher quantum yields. To reduce the complexity of the resulting field envelope, alternatively to the analytic phase confinement, parameter constraints and limitations on the co-domains can be introduced, without loss of efficiency.

In summary, with the GA optimization scheme, one has the possibility to explore the experimental search space by setting all relevant parameters to the actual, experimental conditions. The comparison showed that good agreement for pulse shapes and mechanisms could be reached. Stimulated by these results, several strategies to approach the subspace of low-complexity OCT results could be implemented successfully and simple structured, robust pulses for the GA search with high efficiencies could be proposed. For the experimental implementation of unitary transformations based on vibrational qubits, it can be predicted that the use of pixelated phase and amplitude modulation together with a careful choice of the phase range limitation will be most promising [134].

## 4 Optimization with multi-objective genetic algorithms

The optimization strategies presented in Chapter 3 are based on a single objective function, which corresponds to the quantum efficiency of the investigated processes. Features like the pulse intensity may be included in the formalisms as cost functions, similar to OCT (Eqs. 1.56, 1.60, 2.2). The additional cost term is subtracted from the objective function in the GA optimization (e.g. Eq. 3.2), however, the convergence of the quantum yield is reduced in this case. If a problem is to be studied, involving the control of several features simultaneously, multi-objective algorithms are suited for this task. They can handle several control objectives at the same time. The concept of multi-objective GAs (MOGAs) will be presented and the notion of optimality, which is not obvious anymore within this formalism will be explained. The new technique is applied to optimize picosecond laser fields, driving the vibrational quantum processes, state-to-state transitions and unitary transformations as already studied in Chapter 3. It allows for the additional control of features related to the shaped laser fields and the excitation mechanisms simultaneously to the quantum yield. Within the parameter range, accessible to the experiment, the main focus is on short pulse durations and low pulse energies to obtain preferably robust laser fields. Equivalently, the amount of intermediate overtone excitation can be minimized, which is crucial for quantum control scenarios when dissipative effects occur. Additionally, the interdependency of these properties and the quantum yield is interesting, this could not be studied with OCT so far.

## 4.1 Multi-objective genetic algorithm and application

For the first generation of GAs, a starting population of individuals is randomly generated, where each individual, i.e. each solution is described by a decision vector  $x = (x_1, x_2, \dots, x_n)$  in the decision or parameter space  $X$  of dimension  $n$ . The fitness of every individual is evaluated. Afterwards, a selection of the individuals is performed and they are randomly recombined and mutated to build up a new generation, which is evolving to find better solutions for the control problem. In a single-objective algorithm the fitness is determined by assigning each solution to an objective value  $y$  in the one-dimensional objective space  $Y$  according to  $f : X \rightarrow Y$ . A solution  $x^{(1)} \in X$  is better than another solution  $x^{(2)} \in X$  if the corresponding objective value  $y^{(1)} > y^{(2)}$ . All solutions, existing in the parameter space  $X$ , are mapped on the objective space  $Y$  and a single optimal solution is the result of a single-objective GA run. In the GA investiga-

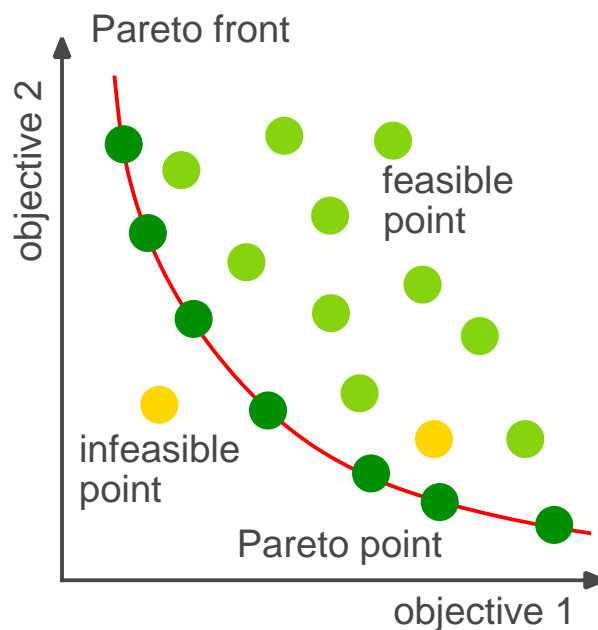


**Figure 4.1:** 2D Pareto front (red line and dark-green circles). The light-green dots are feasible points, whereas the yellow ones indicate infeasible solutions, with respect to the constraints.

tions presented in Sec. 3.2.2, where two conflicting goals should be accomplished simultaneously, both of the criteria were mapped onto a single objective value  $y$  or in other words, a cost function in the objective was included besides the original optimization aim [94]. This optimization strategy leads to a compromise of both control aims similar as in OCT, but the interdependency of the two single objectives cannot be traced clearly. Multi-objective optimizations, also known as multi-criteria optimizations, are best suited for such multi-dimensional control tasks. Now, a solution is assigned to an objective vector  $y = (y_1, y_2, \dots, y_k)$  with the dimensionality  $k$ , given by the number of objectives [135]. The decision of which solutions are better than others is more complex and is made with the selection operator. Here, the concept of Pareto optimality (Pareto dominance relation) is applied. An objective vector  $y^{(1)}$  prevails all other vectors  $y^{(j)}$  if no component  $y_i^{(1)}$  is smaller than the corresponding components  $y_i^{(j)}$  and at least one component has to be larger. Such solutions are said to be non-dominated and they can be mapped onto different objective vectors. Consequently, a Pareto optimal set of solutions is obtained, which build up the Pareto front (Fig. 4.1) in the objective space. The front represents the varying impact of the individual objectives.

In this study, the Elitist Non-Dominated Sorting Genetic Algorithm II (NSGA-II) [136] is applied, which has already been used in quantum control experiments [137]. Additionally, various supplementary constraints might be included in the NSGA-II algorithm. If a solution violates a constraint, it is an infeasible solution and discarded from the set. A schematic sketch of the Pareto front with feasible and infeasible solutions is depicted in Fig. 4.1. The multi-objective algorithm is applied to design optimal laser fields for molecular control scenarios, where it is desirable, to control additional features on the outcome simultaneously. With this algorithm several control objectives can be maximized or minimized, such as the quantum yield and the pulse duration, the degree of overtone excitation, the complexity of the pulse and many more. As in the previous studies (Chapter 3) the genome of the GA comprises the phase and transmittance functions. The modulated laser fields are again constructed by modulations of the FL pulse spectra with the mask functions and calculation of the feedback signals. In case of the phase function  $\phi(\omega)$  the two approaches (parametrized and pixelated forms) will be tested in the MOGA study.

## 4.2 Results and discussion

The MOGA calculations focus on the vibrational excitation processes of IR active modes of the two metal carbonyls  $\text{W}(\text{CO})_6$  and  $\text{MnBr}(\text{CO})_5$ , already studied with single-objective GAs and presented in Chapter 3.

### 4.2.1 2D Pareto fronts for state-to-state transitions

Possible routes for highly efficient state-to-state population transfer, induced by preferably short laser pulses, are investigated theoretically for the  $T_{1u}$  mode of  $\text{W}(\text{CO})_6$ . The fundamental transition  $0 \rightarrow 1$  participates as one key element in the corresponding molecular unitary transformations, where short switching times are very desirable.

The dependence of the quantum yield on different factors, referring to the pulse properties and the control mechanisms is explored. Simultaneously to the maximization of the quantum yield, the additional aims are minimal temporal pulse duration, pulse energy and intermediate overtone population. These features are especially relevant when decoherence sets an upper limit for the laser-molecule interaction time. The dissipative effects will be most disturbing when intermediate overtone excitation is high. Within the experimentally available range, the pulse energy is minimized to prevent side effects, such as non-linear processes. The experimentally investigated molecule  $\text{W}(\text{CO})_6$  is used as a candidate to study different 2D Pareto fronts. The MOGA calculations presented are performed with a population size of 60 and 500 generations.

#### **Objectives: quantum yield and pulse duration**

The MOGA offers an elegant possibility to study the relation of the quantum yield and the pulse duration of shaped laser fields. From the previous GA study (Chapter 3) it is known that the quality of the solutions depends on the FL pulse properties. Therefore, the genome of the MOGA, which comprises only the mask parameters in the experiment, is extended by the FL pulse properties, the FWHM  $\tau_p$ , the carrier frequency  $\omega_c$  and the maximum energy  $\varepsilon_0$ .

As a first test, pixelated mask functions with a spectral pixel resolution of  $10\text{ cm}^{-1}$  are used for all calculations presented in Sec. 4.2.1 together with the parameters given in Tab. 4.1 for the incident pulse. As an alternative, an analytic form  $\phi(\omega) = a \sin(b\omega)$  for the phase function is applied, as often used

parameter	min.	max.
$a$	0	10
$b$	20000	60000
$\varepsilon_0$	0.00001 au	0.001 au
$\tau_p$	100 fs	2000 fs
$\omega_c$	1950 $\text{cm}^{-1}$	2020 $\text{cm}^{-1}$

**Table 4.1:** FL pulse properties for state-to-state transitions.

in the experiment [85, 133, 132] and especially in the mid-IR regime [70]. The two phase parameters  $a$  and  $b$  are optimized. In total, five parameters, have to be adjusted by the GA, given in Tab. 4.1 for analytic phase functions. If pixelated mask functions are applied with 20 pixels for each function (phase and transmittance), 43 parameters including the FL pulse properties are optimized.

The Pareto fronts for the maximization of the quantum yield and minimization of the pulse duration are depicted in Fig. 4.2. The duration of a shaped laser field is defined as the period of time, during which the field  $|\varepsilon(t)|$  exceeds a threshold value of  $5 \cdot 10^{-6}$  GV/cm. Below this energy the mid-IR molecule-laser interaction with the carbonyl complexes is negligible. In the upper panel, pixelated mask functions and in the lower panel analytic phase functions are optimized. The efficiencies are shown from 25 % to 100 % and the high-fidelity region is enlarged in the smaller insets. Both Pareto fronts are convex with respect to the feasible solutions, which is the simplest case for MOGA optimizations. The convex behavior implies that a high quantum yield and short pulse durations are objectives which are reconcilable to some extent. The fronts are characterized by two branches, the vertical one corresponds to high quantum yields and the horizontal one to short pulse durations. A main difference, traced from Fig. 4.2 a) and b), is that in case of an analytic phase modulation the durations of the pulses, reaching high efficiencies, are clearly longer. The FWHMs of the initial FL pulses are in the same range for both approaches. They are found to be rather long (1.0 – 1.5 ps) and the analytic, sinusoidal phase modulation cannot generate multipulses for the solutions, setting up the Pareto front in Fig. 4.2 b). Thus, the long durations of the sinusoidal phase modulated pulses are not due to large subpulse shifts in the multipulse, but rather caused by the inflexible sinusoidal phase approach.

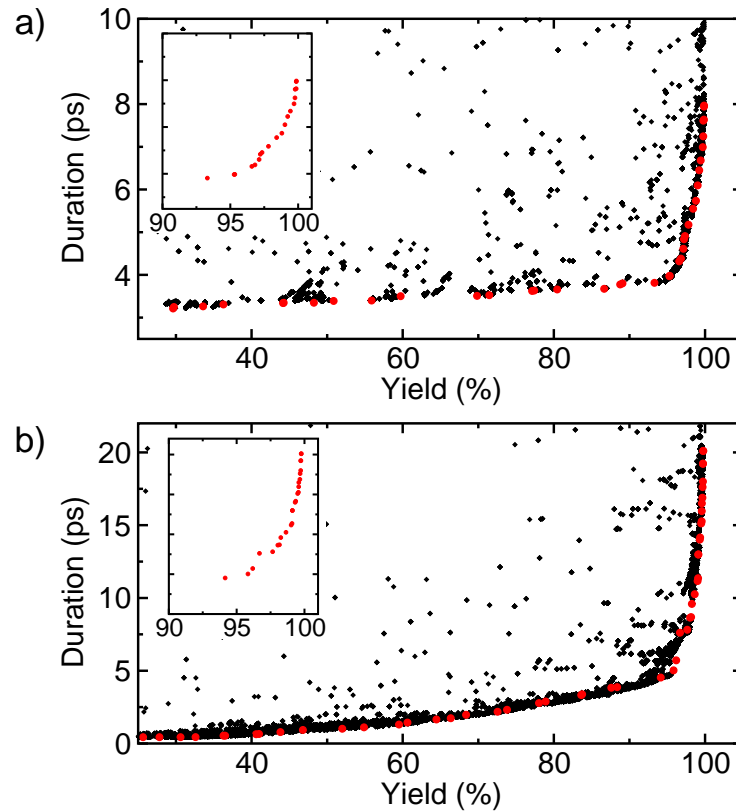


**Figure 4.2:** MOGA results for the two objectives: high quantum yield and low pulse duration. a) Pixelated mask functions. b) Analytic phase function. In both cases the black symbols indicate the feasible solutions and the red dots border the Pareto fronts.

In Fig. 4.3 the best solutions ( $> 99\%$ ) for the pixelated mask functions and the analytic phase are depicted together with the corresponding scaled spectra and their mask functions. The pixelated phase function (Fig. 4.3, left) is rather flat and the shaped pulse provides a duration of  $\sim 8$  ps. In contrast, the sinusoidal phase (right) leads to a temporal duration of  $\sim 20$  ps. The efficiencies of all laser fields exceeding  $80\%$  are monitored (Fig. 4.4, top). For the analytic phase (black dots), 30 solutions are found on the Pareto front and 22 for the pixelated mask functions. Additionally, the FL pulse properties are given in the lower three panels. There is no explicit trend for these properties, instead, in the high-fidelity region different solutions with optimal parameters are found

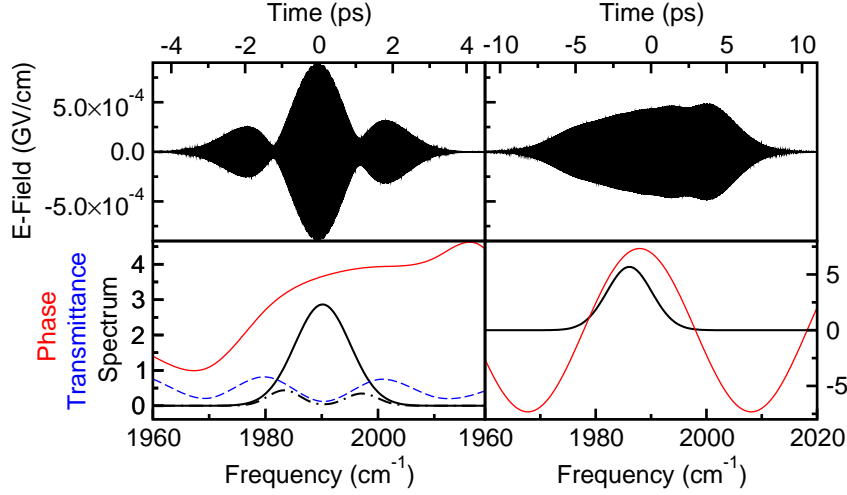


**Figure 4.3:** Resulting best laser fields for the two objectives: high quantum yield and low pulse duration, in the upper panels. The respective mask functions (red: phase; blue, dashed: transmittance) and scaled spectra (black) are depicted in the lower panels. Left: pixelated mask functions. The solid black line refers to the spectrum of the FL pulse, whereas the black dashed line shows the shaped, scaled spectrum. Right: analytic phase modulation.

varying over a broad range, i.e. the FWHMs reach from 900 fs to 1880 fs, the maximum energy from 0.001 GV/cm to 0.0033 GV/cm and the carrier frequency from  $1984\text{ cm}^{-1}$  to  $1991\text{ cm}^{-1}$ . This very advantageous result means that the optimal subspace of different control parameters is rather flexible, and an optimal solution, matching best with the experimental conditions, can be selected from the set. A very obvious distinction can be found in the magnitude of the maximum energy, which is always larger for pixelated mask functions, where additional amplitude modulation is possible. This can be seen in Fig. 4.3, left side, where a pronounced spectral damping by the transmittance function is induced. Accompanied by the fact that the carrier frequencies for pixelated mask functions are detuned by  $5\text{ cm}^{-1}$  (Fig. 4.4, bottom) compared to the analytic functions, the transmittance suppresses the major spectral component (Fig. 4.3, left side), to reach a higher frequency resolution. From the previous results (Chapter 3), it is clear that the complexity of the phase function, in case of the pixelated mask

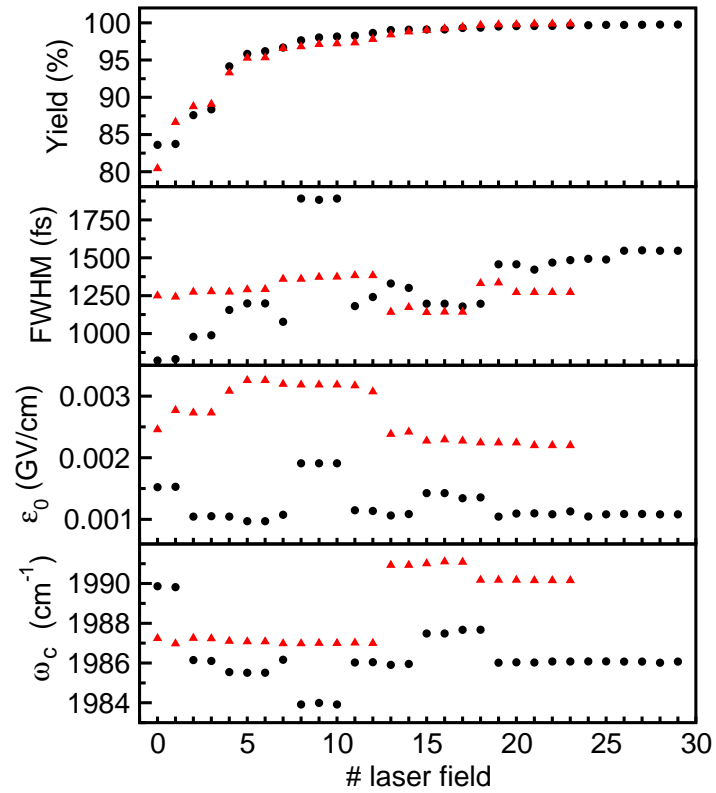


**Figure 4.4:** For the high-fidelity region of the Pareto fronts from Fig. 4.2, the yield and the FL pulse properties (FWHM, maximum energy  $\epsilon_0$  and carrier frequency  $\omega_c$ ) are depicted. The black dots refer to an analytic phase modulation and the red triangles to pixelated mask functions.

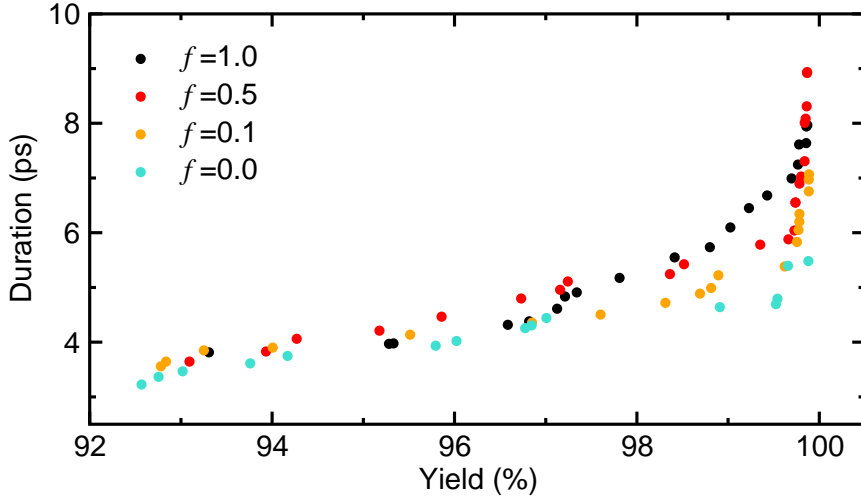


**Figure 4.5:** Resulting Pareto fronts for the two objectives: high quantum yield and short pulse duration, where the phase range is confined, i.e. scaled by the factors  $f$  given in the legend.

functions, can easily be reduced by decreasing the co-domain of the phase function by a factor  $f$  (given in the legend) to the range  $[0, 2\pi] \cdot f$ . The effect of limited phase ranges are shown in Fig. 4.5, where it can be traced that smaller ranges benefit the MOGA search. In general, phase variations between each pixel are much more probable than flat phase functions, but lead to longer pulse durations and complex structures [134]. To find optimal solutions with respect to both objectives, either the number of GA generations can be enlarged significantly or as demonstrated in Fig. 4.5 the co-domain of the phase can be confined.

Only a small part of the complete Pareto front (Fig. 4.2), the high-fidelity region, exceeding efficiencies of 99.0% is relevant in the context of quantum information processing. If such a high-efficiency constraint is introduced and not fulfilled by a solution, this infeasible point is discarded. Consequently, the algorithm searches more intensively in the region of the feasible solutions, which become predominantly located in the high-fidelity regime. This region is better sampled now, since the same number of generations and population size as before is used. The fidelity is limited to a minimum of 99.0% and a corresponding calculation for the pixel mask functions leads to a Pareto front, more dense

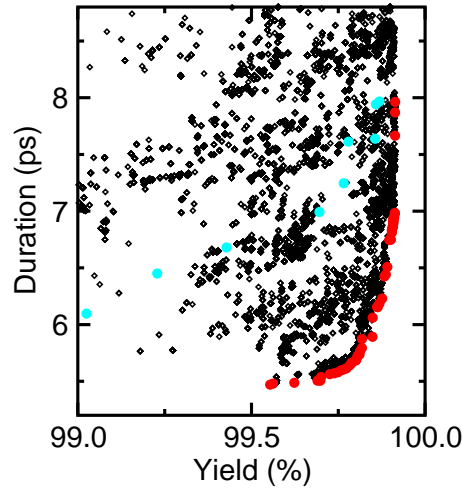


**Figure 4.6:** MOGA optimization constrained to the high-fidelity region. Red dots: position of the Pareto-optimal solutions, black symbols: position of all feasible solutions, light-blue dots: Pareto front of the corresponding unconstrained calculation [Fig. 4.2 a)].

in the regime from 100% to 99% (Fig. 4.6). The black symbols indicate the position of all feasible solutions and the red dots of the Pareto-optimal solutions. The front is steeper and dominates the previous front without the use of the constraint [shown in Fig. 4.2 a) and for comparison indicated in Fig. 4.6 by the light-blue dots]. Here, significantly shorter FWHMs of the FL pulses in the range of 590 fs are found, which is, however, a statistical finding. This can be traced from several MOGA runs with efficiency-constraints, but with random starting individuals. In each run, the highly efficient solutions converged to different FL pulse FWHMs, distributed in the complete range used (Tab. 4.1). All these solutions must also be found in the unconstrained search when the number of iterations is enlarged. In conclusion, in case of pixelated mask functions, a very broad FWHM range at least from 100 fs to 2000 fs, appropriately combined with the remaining FL pulse parameters, can lead to highly efficient, short laser pulses for state-to-state transitions.

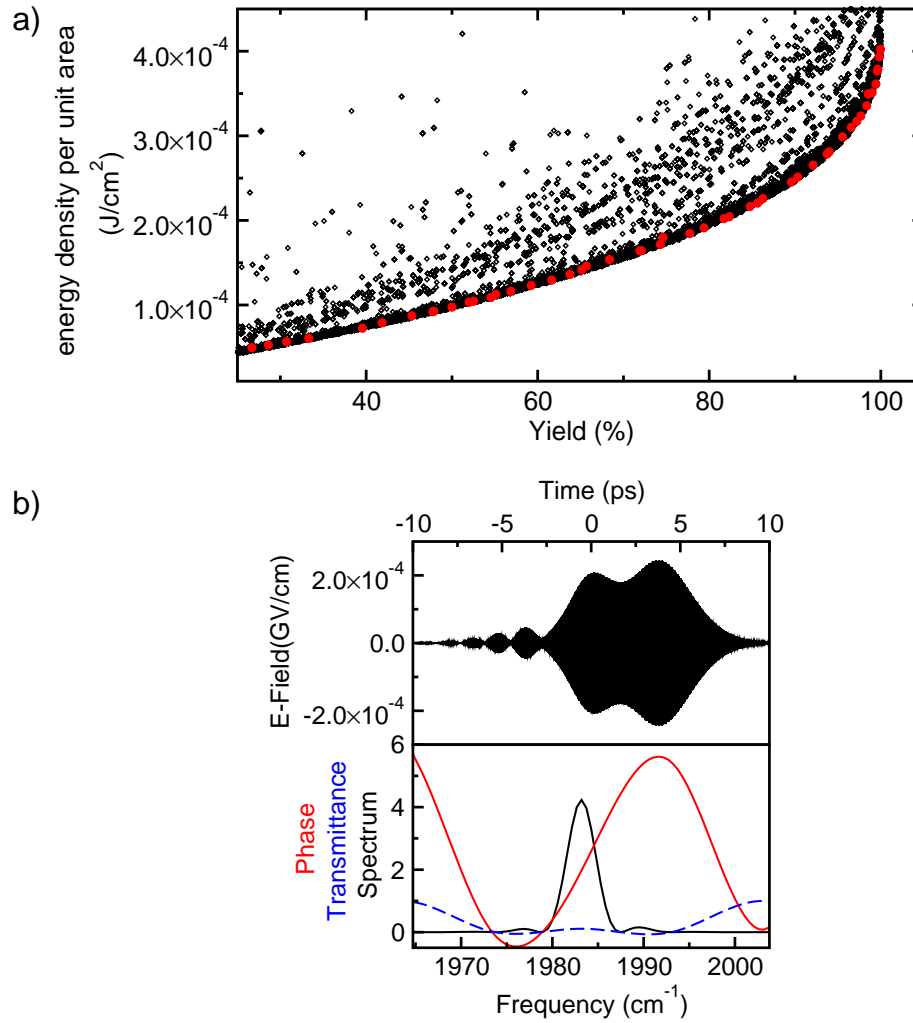


**Figure 4.7:** a) Result of the MOGA optimization with the two objectives high quantum yield and low pulse energy. b) The most efficient laser pulse together with the scaled spectrum and mask functions is depicted.

### Minimization of the pulse energy

The pulse energy, which is a further crucial feature, was unconfined so far and no bias on the energy-efficiency of the transfer process was implemented. Analogously to OCT, where a penalty energy function is included, the energy of the shaped field ( $\int_0^T \varepsilon(t)^2 dt$ ) can be incorporated as the second objective besides the maximization of the quantum yield. No constraint on the phase range is used and the FL pulse parameter ranges are given in Tab. 4.1. The resulting Pareto front is depicted in Fig. 4.7 a), for pixelated mask functions. The minimum pulse energy of the Pareto-optimal solutions has to exceed  $3.4 \cdot 10^{-4} \text{ J/cm}^2$  for an efficiency of 99%. There are several optimal points on the front, exceeding efficiencies of 99% with similar envelope functions for the modulated laser fields. The rather short pulse durations in the range of  $\sim 8 \text{ ps}$ , which was obtained before when the minimization of the pulse duration was the second control aim, cannot be maintained. The temporal duration of the best pulse now exceeds 20 ps [Fig. 4.7 b)]. The best pulse is obtained with a transmittance function strongly damping the spectral signal of the FL pulse. This is one possible solution, also often observed in OCT. Less spectral damping can be obtained when the FL pulse energy is limited, which is not possible in OCT calculations. To reach all desired features at the same time, the three objectives, low energy, short pulse duration and high quantum yield, have to be defined. Corresponding calculations will be presented in Sec. 4.2.2 for a unitary transformation.

### Minimization of the overtone population

A high degree of intermediate overtone population may be obstructive for quantum control experiments. Population relaxation times ( $T_1$ ) in the condensed phase for carbonyl complexes are only approximately half as long as the  $T_1$  time scale of the first excited vibrational state or even shorter [70]. A low overtone excitation can be reached indirectly by using long FL pulses, but the amount of overtone population can also explicitly be formulated as a second objective. The intermediate population  $P_i(t)$  in all  $i$  overtone states, i.e.  $\sum_{i=2}^N \int_0^T P_i(t) dt$  can be minimized, where the time is used in atomic units. The corresponding Pareto front is shown in Fig. 4.8 a). For the used setup, it can be seen that still a finite amount of overtone excitation has to be taken into account for highly efficient solutions. A value of 0.05 integrated population corresponding to an

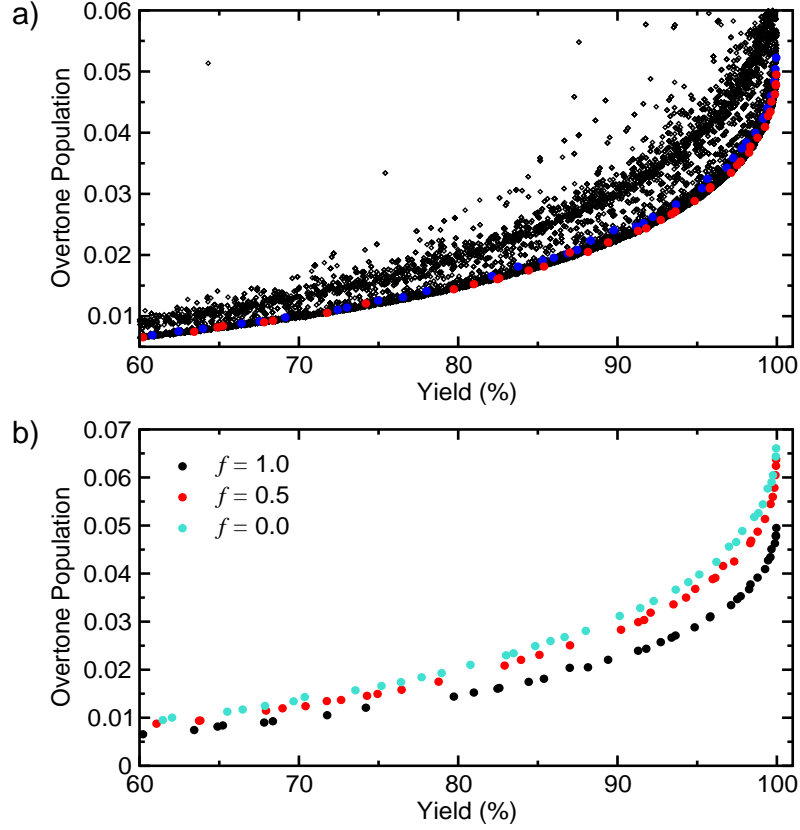


**Figure 4.8:** a) Result of the MOGA optimization with the two objectives high quantum yield and low overtone population. Black and red symbols: for pixelated mask functions. Blue symbols: for analytic phase functions. b) Pareto fronts, with confined co-domains  $([0, 2\pi] \cdot f)$  of the phase range, where the factors  $f$  are given in the legend.

intermediate population maximum of 16% in the second vibrational state is still necessary.

Solutions with confined phase ranges [Fig. 4.8 b)] cannot compete with the calculation for the complete range  $[0, 2\pi]$  and a flexible phase functions turns out to be essential here. A progression of the Pareto front similar to the pixelated phase [Fig. 4.8 a), red symbols] is obtained when a sinusoidal phase modulation is applied on the rather long FL pulses (blue symbols). Consequently, the sinu-

soidal phase functions facilitates the suppression of the amount of population transfer in higher vibrational levels equivalently to the pixelated mask functions.

With the analysis of the 2D Pareto fronts, the interplay of the quantum yield with additional features of interest can be understood and interpreted for the first time, qualitatively as well as quantitatively. From the 2D fronts it is also possible to judge whether higher dimensional fronts are needed to improve the solutions with respect to their feasibility.

### 4.2.2 3D Pareto front for a unitary transformation

It is desirable to reach all objectives, presented in Sec. 4.2.1, simultaneously for effective, robust and realizable quantum gate operations. The effect of the three most relevant objectives: the maximization of the quantum yield, the minimization of the shaped pulse duration and the energy density per area, will be discussed. The quantum yield is defined as the average quantum efficiency of the single population transfer processes induced by the quantum gate operation. To obtain a phase correct quantum gate, an additional time delay has to be attached, for correct phase rotation [49]. As an example, the two-qubit CNOT gate, operating on the E mode of  $\text{MnBr}(\text{CO})_5$  is used. The calculations are performed for pixelated mask functions with a spectral resolution of  $10 \text{ cm}^{-1}$  for 1000 generations and a population size of 100 individuals. Additionally, a constraint of a minimum 90.0 % yield is applied. The 3D Pareto front, shown in Fig. 4.9 a), is tilted in the 3D objective space and for better visualization it is interpolated. The highest efficiencies are shown as the red section and mark the region of unitary transformations that can be realized with minimal pulse energy and duration. For short pulses, the section is slightly curved, while for increasing pulse durations the energy stays constant. For durations  $< 9 \text{ ps}$ , intermediate overtone excitation occurs and higher energies are necessary to depopulate these states again. For longer pulse durations the spectral resolution suffices to avoid overtone excitation and the required energy only depends on the size of the fundamental transition matrix element. The Pareto front tilts towards lower quantum yields for smaller pulse energies and durations. The pulses, found as Pareto-optimal solutions provide very simple envelope functions. Most of them are almost Gaussian-shaped or composed of few Gaussian-shaped pulses overlapping in time. The quantum gate laser field with the highest efficiency is presented in Fig. 4.9 b). The pulse energy is  $11.8 \cdot 10^{-4} \text{ J/cm}^2$  and the pulse du-

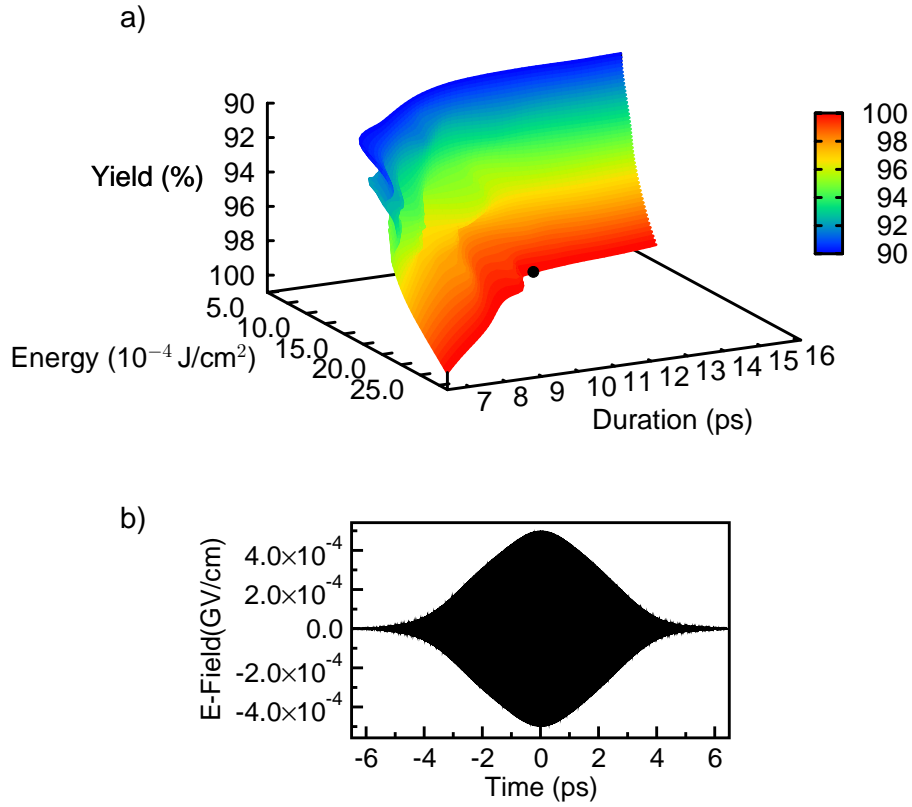


**Figure 4.9:** a) 3D Pareto front for the unitary transformation  $\text{CNOT}_E$  with the three objectives quantum yield, pulse duration and pulse energy. b)  $\text{CNOT}_E$  gate, one of the optimal solutions from the optimal set. The position is indicated on the 3D Pareto front by the black dot.

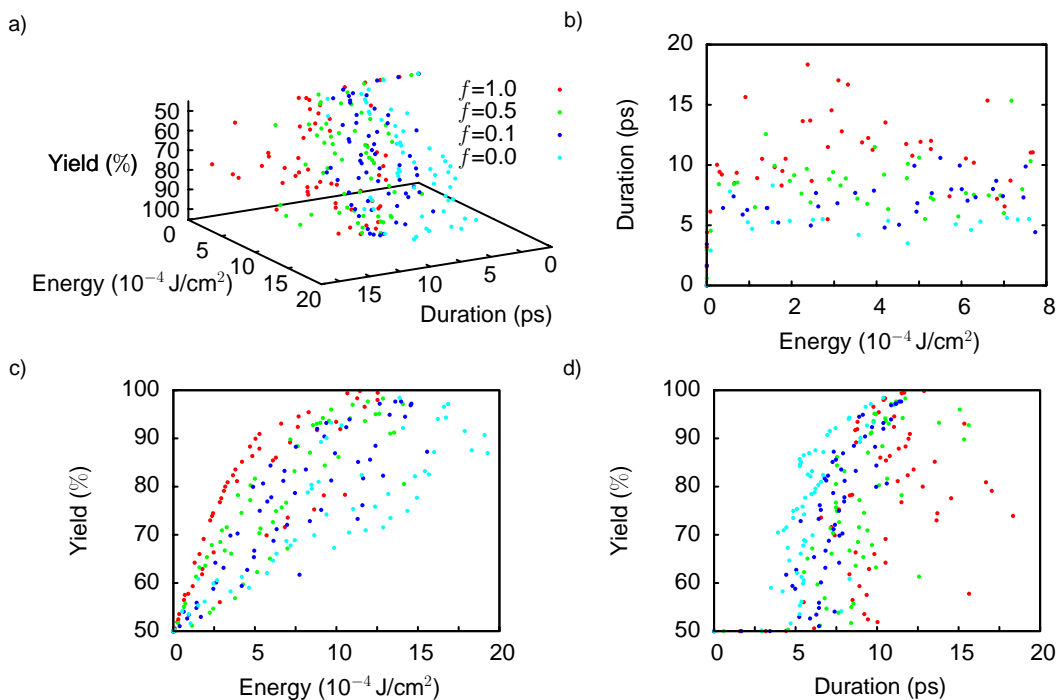


**Figure 4.10:** a) 3D Pareto front for a unitary transformation with different factors  $f$ , confining the co-domain of the phase function  $[0, 2\pi] \cdot f$ . Projection onto two objectives: b) pulse duration and energy c) yield and pulse energy d) yield and pulse duration.

ration is 12 ps. The Pareto-optimal pulse shapes are very similar to the previous OCT results [53, 52]. Here, the duration was varied manually to obtain simple pulse structures, in the MOGA calculation the pulse duration was selected as an objective. Now, the solutions found by the search strategies OCT and MOGA clearly coincide, which means that the MOGA results match the OCT subspace or vice versa the simple structured OCT results are located on the Pareto fronts.

Different co-domains  $[0, 2\pi] \cdot f$  for the phase functions are compared in Fig. 4.10, where a spectral pixel resolution of  $10 \text{ cm}^{-1}$ , a population size of 60 and 500 generations were used. In Fig. 4.10 a) the 3D Pareto fronts for the factors  $f = 1.0, 0.5, 0.1, 0.0$  are depicted, Figs. 4.10 b), c), d) show projections onto two of the objectives. From Fig. 4.10 b), the relation of the pulse energy and the pulse duration can be traced. The pulse durations become shorter for

confined co-domains, e.g. for pure amplitude modulation ( $f = 0$ , cyan dots) the mean pulse duration is  $\sim 7$  ps compared to  $\sim 14$  ps for full phase modulation (red dots), which can also be seen in Fig. 4.10 d). On the other hand, flexible phase functions lead to shaped pulses with the least pulse energy (red dots in Fig. 4.10 c) and vice versa, the most energy is needed for pulses, which are amplitude modulated only. All 3D Pareto fronts obtained for the factors  $f$  confining the co-domains would merge into one for a large number of generations. If one feature, such as the pulse duration, is of special interest the search can be accelerated significantly by reducing the phase range. If more, conflicting features are of interest, an appropriate compromise must be found, e.g. low pulse energy is facilitated by flexible phase functions, whereas low pulse durations are realized by small phase variations.

Changing the spectral resolution for the pixels from  $10 \text{ cm}^{-1}$  to  $5 \text{ cm}^{-1}$  enables faster convergence, but leads to more complex envelope functions. Additionally, the pulse duration regime for high-efficiency solutions shifts from 7 ps – 15 ps to 8 ps – 27 ps. From these results, it can be suggested for experimental studies to use only the minimum necessary spectral resolution of the pixels so that the desired quantum yield can still be reached. This will lead to envelope functions with the lowest complexity, the shortest pulse durations and lowest energies, which are the most robust solutions in the search space.

## 4.3 Conclusion

This study focused on MOGAs for the optimization of mask functions for laser fields, driving different quantum processes such as state-to-state transitions and unitary transformations [138]. By default, single-objective GAs are used in closed loop experiments, where the main emphasis is put on the quantum yield and no bias concerning e.g. the pulse duration is included. Here, different other features of the shaped laser pulse or the excitation mechanism are optimized simultaneously. Particularly, the pulse duration, the energy density per unit area and the induced degree of intermediate overtone excitation are taken into account. The Pareto fronts for each set of objectives are constructed. All of them are convex with respect to the dominated feasible solutions and consequently the selected objectives (quantum yield, pulse energy, pulse duration, intermediate overtone population) can be reconciled. The minimum requirements on the laser pulses or crucial features of the excitation mechanisms can be extracted from

these fronts. Highly efficient Pareto-optimal solutions can be realized with a large variety of FL pulse parameters, which is very advantageous as it makes the subspace of control parameters rather flexible and an optimal solution, matching best with the experimental conditions, can be located and selected from the Pareto fronts. From the analysis of the 2D and 3D Pareto, the interplay of various objectives of interest can be traced, qualitatively and quantitatively. For experimental applications, it can be suggested to use only the minimum necessary spectral resolution of the pixels and to adapt the phase co-domain to generate short pulse durations. These results are assumed to be the most robust ones also against dissipation, and as a positive side effect, they show very simple envelope functions. In addition, the MOGA and OCT predictions for the unitary transformations match very well. The most promising solutions for given control scenarios were found and experimental routes towards them were revealed [138].

## 5 Laser field optimization with a modified ant colony algorithm

Quantum control experiments based on computer controlled pulse modulators typically lead to complex pulse shapes [133]. When using pixelated mask functions, the pixel values are completely uncorrelated and can take any arbitrary value in the range  $[0, 2\pi]$ . Distinct phase jumps between neighboring pixels are possible, which tends to generate complex laser fields, consisting of several subpulses. Strongly varying phases and transmittance functions also lead to longer pulse durations. An idea, circumventing the high complexities and allowing for the interpretation of the control processes is based on the parametrization of the shaped pulses, frequently sinusoidal forms have been applied in the experiment [133, 85, 132]. The parametrized mask functions are characterized by smoother progressions and the resulting envelopes can turn out simpler. However, from the theoretical investigations presented in Chapter 3 and discussed in [134], it is clear that the parametrized, sinusoidal phase modulation, is not the best choice in the context of molecular quantum computing with vibrational qubits and for the implementation of highly efficient quantum gates.

Since the efficiencies of complex and long pulses are not necessarily lower than for simpler pulse structures, the GA-based concepts, which is used in the experiments by default without a limitation of the phase range will only produce simple solutions (with simple pulse structures similar to OCT results) by instance. The simplest laser fields could be optimized theoretically by the use of multi-objective algorithms as shown in Chapter 4, allowing for the control over any desired property of the laser pulse or the resulting mechanism. Here, also the confinement of the phase range, presented in Chapter 3, was used as for the single-objective algorithm. However, this is only a first step, since the phase functions can still vary in the available ranges, the co-domains are limited to. Moreover, it would not be reasonable to implement a similar restriction of

the transmittance functions and for too strong phase limitations the GAs might lose the required flexibility for more complex control tasks.

Thus, a new optimization concept, also operating in the frequency domain as GAs, is necessary, which tolerates phase jumps, needed to reach high quantum efficiencies, but avoids strong fluctuations of the mask functions. Such a concept will lead to simple results and could be implemented as an alternative to single-objective algorithms in the experiment.

A new optimization strategy is presented, which combines the benefits of both mask function approaches from the experimental setup, parametrized and pixelated forms. Learning from their advantages and shortcomings, it is clear that a slight correlation between the pixel values has to be implemented. This introduces a control on the complexity of the mask functions, which is directly related to the complexity of the resulting shaped laser fields. The value, each pixel takes, will still be optimized freely, but with the new method, a tunable correlation between neighboring pixels is introduced, while the flexibility of the phase is assured by avoiding strict parametrizations. The optimization procedure still corresponds to a learning loop setup, but instead of a GA, the optimization is based on a modified ant colony optimization (ACO) scheme.

## 5.1 Basics of ACO

ACO was first introduced by M. Dorigo [139, 140]. It is a probabilistic technique for combinatorial optimization problems. As a natural algorithm, it is a part of swarm intelligence. The idea of ACO was originally derived from ants and their behavior of finding direct paths from their nest to the food source fast, despite the fact that they are almost blind. The algorithm basically mimics the behavior of natural ants. Initially, ants search for food randomly [Fig. 5.1 a)]. Coincidentally, an ant can find a short track and when returning to the colony, after finding food, they deposit pheromone trails  $\tau$  [Fig. 5.1 b) and c)], which is the major feature of the collective communication network. Depending on the strength of the pheromone trail, the following ants, which encounter such a path, will probably follow the trail instead of travelling at random [Fig. 5.1 c)]. Consequently, when returning from such a path, as a positive feedback, they will even reinforce it and build up a collective memory, attracting more ants. Since ants are not completely blind, also a visibility function  $\eta$  is taken into account in the algorithm, helping the ants to find shorter ways. The artificial ants in the

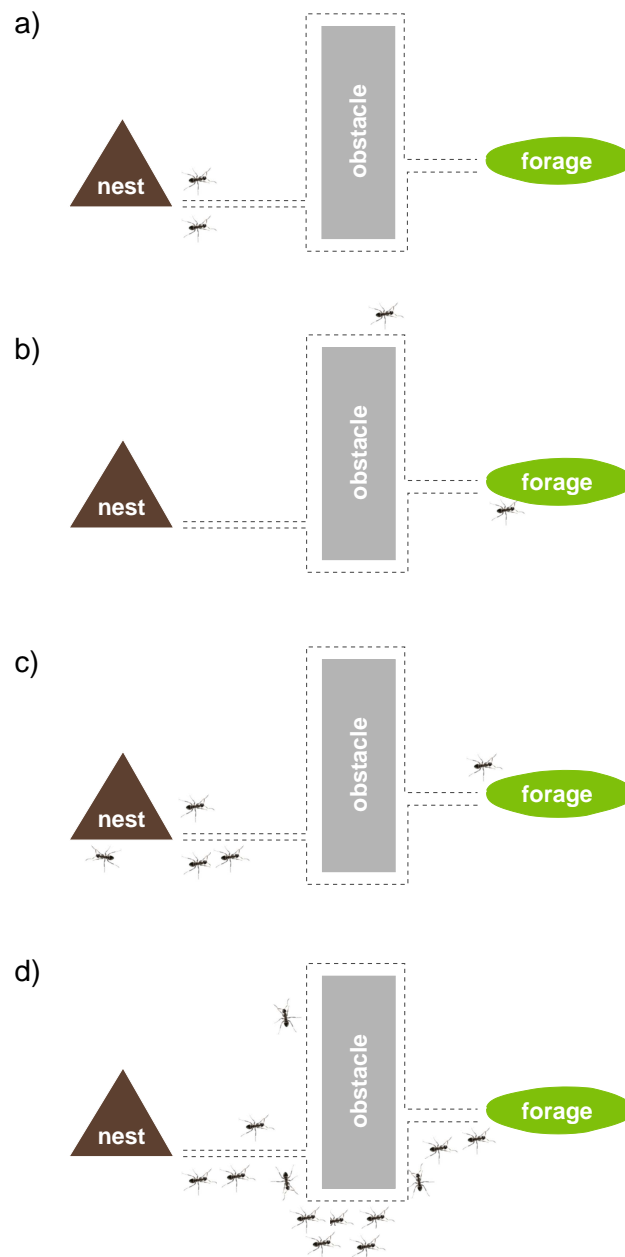


**Figure 5.1:** Initially, ants are searching for food randomly a). After a short time an ant trail has established d), due to pheromone deposition b), which is attractive to other ants c) and builds up a collective memory.

algorithm choose their paths according to a probability function  $p$ , depending on the pheromone trail  $\tau$  and the visibility  $\eta$ . Over time, the pheromone trails start to evaporate (with the evaporation rate  $1 - \rho$  and the trail persistence  $\rho$ ) and their attraction to following ants, passing these trails, will be reduced. If an ant takes a long way from the nest to the food source and back, the pheromone density will be lower than on short tracks and the short ones will be preferred by other ants. Within a short time, a direct ant trail from the nest to the food source will be established [Fig. 5.1 d)].

This optimization scheme has been demonstrated for the travelling salesman problem [139, 140] and also applied successfully in various, mainly technical branches. Also different fields in chemistry make use of the ACO algorithm, such as protein folding [141] and conformational analysis of flexible, drug-like molecules [142]. The original probability function of the algorithm presented by M. Dorigo for the travelling salesman problem is given in Eq. 5.1, describing the probability for an ant to travel from the city  $i$  to  $j$  in the iteration  $t$ , summing over all  $m$  towns.

$$p_{ij}(t) = \frac{[\tau_{ij}(t)]^\alpha [\eta_{ij}(t)]^\beta}{\sum_m [\tau_{im}(t)]^\alpha [\eta_{im}(t)]^\beta} \quad (5.1)$$

The pheromone trail between these cities is given by  $\tau_{im}(t)$  and is adjusted from iteration to iteration, whereas the visibility  $\eta_{im}$  is constant. The parameters  $\alpha$  and  $\beta$  specify the impact of the pheromone trail and the visibility.

## 5.2 ACO application to quantum control

In theoretical quantum control studies, simple structured control fields, inducing adiabatic switching mechanisms without high overtone population, can be obtained with OCT, using high penalty factors [52]. When the outcome is transferred to the frequency domain, the corresponding mask functions can be retrieved as a direct link to the experiment [92]. Usually, the phase function is rather smooth and phase jumps are rare and not pronounced [52]. The modulation of the transmittance function is stronger and often suppresses spectral components of the FL incident pulses. A default GA implementation cannot be used directly to provide results conforming with OCT properties of the mask functions and MOGA optimizations might be demanding to realize in experi-

ment. In contrast, the pulse characteristics known from the simple structured OCT results can be conserved when using the ACO algorithm, which also operates in the frequency domain.

In this approach, probability functions  $p$  are defined, referring to the transmittance ( $p^T$ ) and the phase ( $p^\phi$ ). In GA calculations, each value of the phase and transmittance range is equally likely to be chosen. Instead, the modified ACO approach, similar to the one presented in [142] for the conformational analysis of drug-like molecules, is based on non-uniform probability functions. Here, they consist of the visibilities  $\eta^\phi$  and  $\eta^T$  and the pheromone trail functions  $\tau^\phi$  and  $\tau^T$ , given in Eqs. 5.2 and 5.3.

$$p^{\phi_i}(\Delta\phi_i, t) = (1 - \beta)\tau^{\phi_i}(\Delta\phi_i, t) + \beta\eta^\phi(\Delta\phi_i) \quad (5.2)$$

$$p^{T_i}(\Delta T_i, t) = (1 - \beta)\tau^{T_i}(\Delta T_i, t) + \beta\eta^T(\Delta T_i) \quad (5.3)$$

Both types of probability functions are calculated in each iteration  $t$ .  $p^{\phi_i}(\Delta\phi_i, t)$  describes the probability that an ant will choose a phase variation  $\Delta\phi_i$  between the pixels  $i$  and  $i - 1$ . The total number of phase pixels is  $n$ . Each pair of neighboring pixels has its own phase probability function, denoted by the index  $i$  in  $p^{\phi_i}$ . Accordingly,  $\Delta T_i$  gives the difference of the transmittance values for the two neighboring pixels  $i$  and  $i - 1$ . The parameter  $\beta$  specifies the weight of the visibility functions  $\eta$  and the pheromone trail attractiveness  $\tau$ . The phase visibility function  $\eta^\phi$  (Eq. 5.4) allows for phase jumps between neighboring pixels discretized in the range  $\Delta\phi_i : [-\pi, \pi]$ . Since the phase variations should be as low as possible, a normal distribution, centered at a phase jump  $\Delta\phi_i = 0$ , is chosen. The size of the standard deviation  $\sigma_\eta^\phi$  determines the probability of larger phase variations occurring between two neighboring pixels.

$$\eta^\phi(\Delta\phi_i) = N^{\eta^\phi} \frac{1}{\sigma_\eta^\phi \sqrt{2\pi}} e^{-\frac{1}{2} \left( \frac{\Delta\phi_i}{\sigma_\eta^\phi} \right)^2} \quad (5.4)$$

The phase visibility function is constant for each iteration  $t$  and for each pair of pixels of the phase function. Similarly, the transmittance visibility function (Eq. 5.5) is defined. Since the transmittance should vary only slowly, deviations between the pixels are defined and discretized in the range  $\Delta T_i : [-1, 1]$  and the distribution is centered around  $\Delta T_i = 0$ .

$$\eta^T(\Delta T_i) = N^{\eta^T} \frac{1}{\sigma_\eta^T \sqrt{2\pi}} e^{-\frac{1}{2} \left( \frac{\Delta T_i}{\sigma_\eta^T} \right)^2} \quad (5.5)$$

The parameters  $N^{\phi^T}$  and  $N^{\eta^T}$  are used to normalize both functions. The algorithmic pheromone trail communication network works as follows. A trail (for each pair of pixels) is updated in every new iteration  $t + 1$ , where a certain part of the old trails  $\tau$ , determined by  $\rho$ , does not evaporate from one iteration to the next one and is added to the respective trail updates  $\Delta\tau$  (Eqs. 5.6 and 5.7).

$$\tau^{\phi_i}(\Delta\phi_i, t + 1) = \rho\tau^{\phi_i}(\Delta\phi_i, t) + (1 - \rho)\Delta\tau^{\phi_i}(\Delta\phi_i) \quad (5.6)$$

$$\tau^{T_i}(\Delta T_i, t + 1) = \rho\tau^{T_i}(\Delta T_i, t) + (1 - \rho)\Delta\tau^{T_i}(\Delta T_i) \quad (5.7)$$

Again, the functions are discretized in the ranges of  $\Delta\phi_i$  and  $\Delta T_i$ . The trail updates are given in Eqs. 5.8 and 5.9.

$$\Delta\tau^{\phi_i}(\Delta\phi_i) = N^{\tau_i^{\phi}} \sum_k \Delta\tau^{\phi_i, k}(\Delta\phi_i) \quad (5.8)$$

$$\Delta\tau^{T_i}(\Delta T_i) = N^{\tau_i^T} \sum_k \Delta\tau^{T_i, k}(\Delta T_i) \quad (5.9)$$

They correspond to a sum over the trail updates referring to the individual  $k$  ants in the actual iteration step and include parameters to normalize the functions for each pair of pixels  $i$ . The single trail updates, referring to the path of an ant  $k$  are given in Eqs. 5.10 and 5.11 and are evaluated in every iteration for every ant.

$$\Delta\tau^{\phi_i, k}(\Delta\phi_i) = \frac{Y^k}{\sigma\sqrt{2\pi}} e^{-\frac{1}{2}\left(\frac{\Delta\phi_i - \Delta\phi_i^k}{\sigma}\right)^2} \quad (5.10)$$

$$\Delta\tau^{T_i, k}(\Delta T_i) = \frac{Y^k}{\sigma\sqrt{2\pi}} e^{-\frac{1}{2}\left(\frac{\Delta T_i - \Delta T_i^k}{\sigma}\right)^2} \quad (5.11)$$

The functions reflect normal distributions with the standard deviations  $\sigma$  located around the phase or transmittance variation values  $\Delta\phi_i^k$  and  $\Delta T_i^k$  chosen by the  $k$ -th ant. The distributions are additionally weighted by a factor corresponding to the quantum yield  $Y^k$  of the process, driven by the laser pulse, which is constructed from the path of ant  $k$ . To reach faster convergence, these expressions (Eqs. 5.10 and 5.11) can further be modified, which will be discussed

below. At the first iteration  $t = 0$ , the probability functions correspond to the respective visibility functions, since no pheromone trail exists in the beginning:

$$p^{\phi_i}(\Delta\phi_i, 0) = \eta^{\phi}(\Delta\phi_i), \quad (5.12)$$

$$p^{T_i}(\Delta T_i, 0) = \eta^T(\Delta T_i). \quad (5.13)$$

Now, a specified number of ants starts to travel over  $n - 1$  values, for the phase and transmittance functions. They take discretized values in the ranges of  $\Delta\phi_i$  and  $\Delta T_i$  (sampled in 1000 intervals), according to the respective probability functions. As selection operator, a biased roulette wheel is applied. The slot sizes are proportionate to the corresponding amplitude values of the probability functions. Within an iteration, each ant makes  $n - 1$  roulette wheel selections for the phase function. The first phase pixel value is set to  $\phi_0 = 0$  and the complete function is composed of the optimized  $\Delta\phi_i$  values, starting for  $i = 1$ , according to:

$$\phi_i = \phi_{i-1} + \Delta\phi_i. \quad (5.14)$$

The same holds for the transmittance function:

$$T_i = T_{i-1} + \Delta T_i. \quad (5.15)$$

The initial value is set to  $T_0 = 1$ . In case that the transmittance over- or undershoots the domain of definition, it is readjusted to this range. As illustrated in Chapter 3 and in [134], the constructed phase and transmittance functions modulate the incident laser pulses. The molecular system is afterwards propagated under the influence of the external, electric field and the yield of the desired quantum process, corresponding to the feedback signal is evaluated. If all ants of the actual iteration have completed their tour, i.e. constructed their laser fields and the quantum yield is evaluated, they deposit a certain amount of pheromone on the trails according to Eqs. 5.10 and 5.11 and the trails are updated using Eqs. 5.8, 5.9, 5.6, 5.7. Together with the visibility functions the new probability functions are determined based on Eqs. 5.2 and 5.3 and the next generation of ants starts to travel. Learning from the previous ants, they alter the laser fields statistically, according to the updated collective memory and improve the quantum yield.

For the study of the power of the modified ACO method, a vibrational NOT quantum gate for the molecule  $\text{W}(\text{CO})_6$  was chosen as objective. As before, the

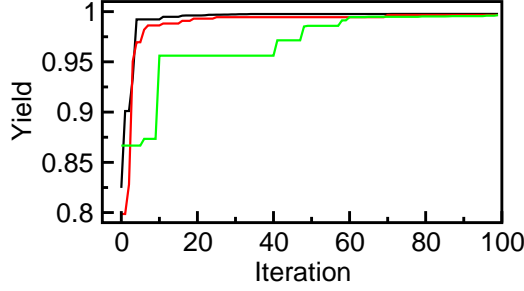


**Figure 5.2:** Convergence of the ACO approach over the first 100 iteration. In each case the maximum quantum yields are depicted. Black line: the 30 % best ants contribute to the probability functions. Red line: the ants reaching quantum efficiencies higher than 90 % contribute. Green line: all ants contribute to the probability function.

qubit basis states  $|0\rangle$ ,  $|1\rangle$  are encoded by the vibrational ground state and first excited state of a  $T_{1u}$  symmetric mode of the carbonyl complex. For the quantum gate optimizations, a FL pulse with the carrier frequency  $\omega_c = 2000 \text{ cm}^{-1}$ , the FWHM of the intensity profile  $\tau_p = 468 \text{ fs}$  and the maximum energy  $\varepsilon_0 = 0.001 \text{ au} = 0.005 \text{ GV/cm}$  was used.

Tests on the convergence were performed, where the usage of Eqs. 5.10 and 5.11 were altered. In the first run, they were used as given in the equations above (Eqs. 5.10, 5.11, green line of Fig. 5.2). This approach shows the slowest convergence and an efficiency of 99 % is reached for the first time after 59 iterations in the calculation and is exemplified in Fig. 5.2. In the other case the ants, which reach quantum efficiencies over 90 % or the ones with efficiencies above the average of all ants in the actual iteration, contribute to the pheromone trail. The red line in Fig. 5.2 is the convergence of the ACO run, where the ants reaching efficiencies higher than 90 % take part in the construction of the probability function. Here, after 16 iterations a quantum yield of 99 % is reached. As a last case, only the  $\sim 30\%$  best ants deposited pheromone on their paths. This latter variant proved to provide the fastest convergence (99 % after 4 iterations, black line in Fig. 5.2) behavior with the most efficient results, where 30 ants and 1000 iterations were used in the calculation.

For preferably short and simple structured laser fields a choice of the values given in Tab. 5.1 has proven suitable. In Fig. 5.3 a), the average and maximum

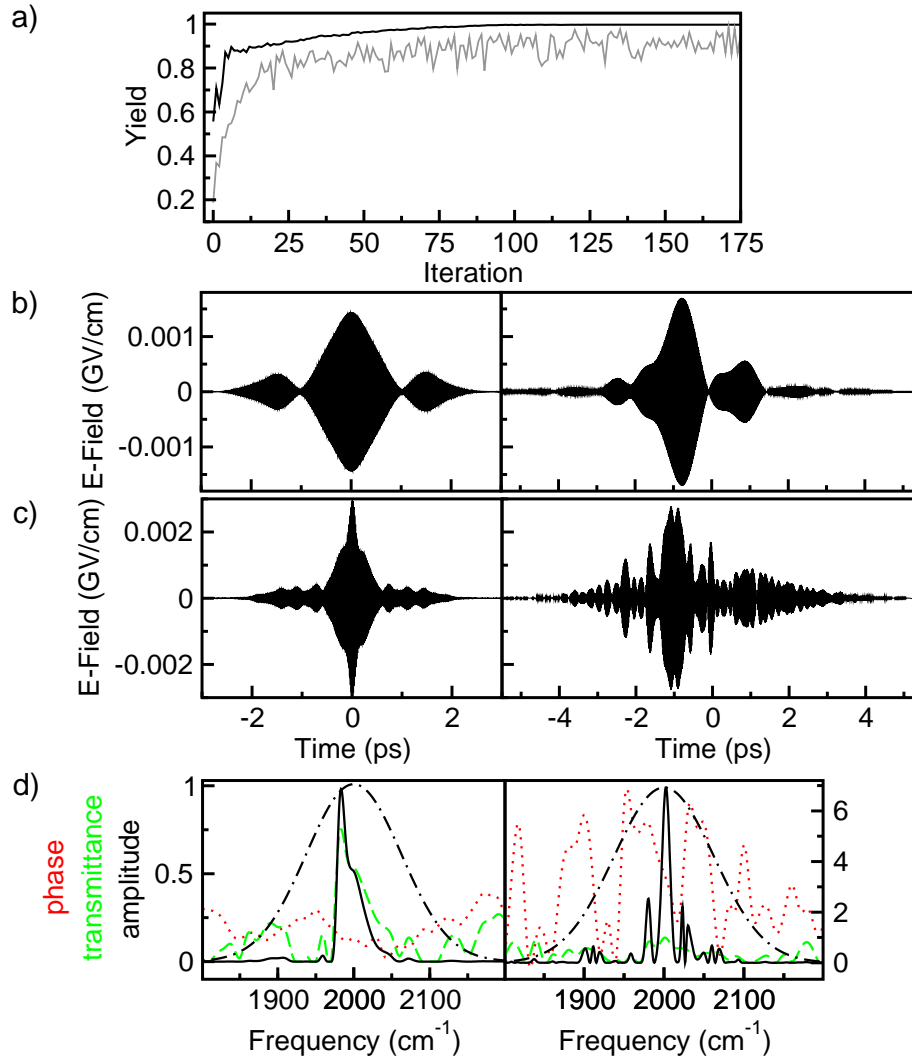


**Figure 5.3:** a) Average (gray) and maximum (black) quantum yields for a NOT gate optimization. b) Best NOT gates (left: ACO, right: GA) after 1000 iterations. The calculations were performed for FL pulses with  $\tau_p = 468$  fs. c) Best NOT gates (left: ACO, right: GA) obtained for  $\tau_p = 100$  fs. d) Scaled spectra of FL pulses (dashed-dotted, black line) and shaped pulses (solid, black line), depicted in c). The transmittance is marked in green (dashed) and the phase in red (dotted).

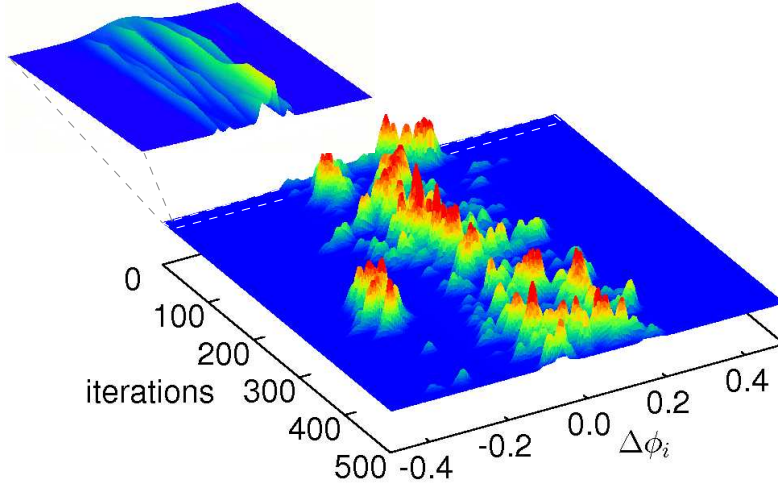


**Figure 5.4:** Evolution of the phase probability function for  $\Delta\phi_i$ , the phase jump between the two neighboring pixels, associated with the most intense spectral component of the FL pulse. The first five iterations are additionally enlarged for better visibility of the initial Gaussian distribution.

$\beta$	$\rho$	$\sigma$	$\sigma_\eta^T$	$\sigma_\eta^\phi$
0.05	0.1	0.01	0.5	0.1

**Table 5.1:** ACO-parameters used in the NOT gate optimization.

quantum yields are displayed for this set of parameters. The most efficient NOT gate is depicted in Fig. 5.3 b), left. For comparison of GA and ACO results, a GA run as in Chapter 3 is performed for the same FL pulse and with a population size of 30 and 1000 generations. The structure of the resulting GA laser field [Fig. 5.3 b), right] is more complex and the pulse duration doubles. The elongated pulse duration together with the slightly increased intermediate overtone excitation (not shown here) will become crucial in the presence of dissipation. When shorter FL pulses are applied ( $\omega_c = 2000 \text{ cm}^{-1}$ ,  $\tau_p = 100 \text{ fs}$ ,  $\varepsilon_0 = 0.003 \text{ au} \approx 0.015 \text{ GV/cm}$ ) as often used in the experiments, the complexity of the GA-optimized fields significantly increases [Fig. 5.3 c), right]. The strong

phase and transmittance modulations [Fig. 5.3 d), right] cause the high complexity and longer pulse duration in comparison to the ACO solution [Fig. 5.3 c), left]. For the ACO calculation the same optimization parameters (changing only  $\sigma_\eta^T = 0.05$ ,  $\sigma_\eta^\phi = 0.01$ ) were used. The corresponding laser field stays short and comparably simple with small mask function modulations [Fig. 5.3 d), left]. Such simple mask functions are seldom reached in GA runs, since there is no bias on small variations between the pixels. Due to the simple transmittance function of the ACO solution [Fig. 5.3 d), left], the shaped spectrum exhibits only the minimum necessary peak for the transition process and the phase is almost constant. The GA-optimized amplitude function [Fig. 5.3 d), right] generates several frequency components with different phase relations, which do not enable a straightforward extraction of the mechanism.

With the convergence scheme based on the 10 best ants contributing pheromone, the dependence of the control parameters on the algorithm was studied. These calculations were performed for 30 ants and 100 iterations and each control parameter was scanned while keeping the others constant, as given in Tab. 5.1. The parameters  $\beta$ , balancing trail attractiveness and visibility, and  $\rho$ , the trail persistence can be chosen in the range from 0 to 1. The algorithm seems to be very robust, particularly with regard to the quantum yield of the best individuals, which are all above 98%. The higher the impact of the visibility function is chosen, the lower is the average reached yield in the ACO runs. In principle, the contribution of the visibility selected can be rather small, since in the beginning the probability function is completely defined by the visibility and the character is preserved by selection of high  $\rho$  values. The dependence on  $\rho$  is equally robust and the average value of the ants in different iterations converges to  $\sim 90\%$ , for  $\rho = 0.0 - 0.8$ . Above  $\rho = 0.8$  only low learning effects, according to Eqs. 5.10 and 5.11 take place, which hinder or even preclude convergence. Scanning the influence of the parameters  $\sigma_\eta^\phi$ ,  $\sigma_\eta^T$  shows that the best quantum yields are all above 98% for values exceeding 0.02. Smaller values for  $\sigma_\eta^T$  constitute too strict limitations on the amplitude modulation. In general, narrower normal distributions can be applied for the phase functions. The average yield values rise significantly faster for  $\sigma \leq 0.25$  than for larger ones. The pulse complexities are not affected by the choice of the parameters  $\beta$  and  $\rho$ . Here, a significant effect is observed for the parameter  $\sigma$ , consequently small values should be selected.

The evolution of the probability function during the optimization is illus-

trated in Fig. 5.4 along the phase deviation  $\Delta\phi_i$  for a pair of neighboring pixels, associated with the most intense spectral component of the FL pulse. In the first iteration the probability function equals the Gaussian distribution of the visibility function  $\eta^\phi$  (enlarged part in Fig. 5.4). During the optimization, the ants, reaching high quantum yields ( $\geq 90\%$ ), are significantly involved in the construction of the pheromone trail. In combination with the small  $\sigma$  value, this leads to the rather narrow trail widths, which still remain located close to  $\Delta\phi_i = 0$ , guaranteeing simple phase functions, despite of the fact that the contribution  $\beta$  of the visibility function is chosen low. However, the presence and significance of the visibility with a rather broad distribution can still be traced. For the iterations 200 – 300, probability maxima arise at  $\Delta\phi_i = -0.2$  from a statistical selection out of the trailing edges of the visibility, contributing slightly to the probability function. This is in some sense similar to the effect of the mutation operator in GAs, providing new features for the pool of individuals and it demonstrates the flexibility of the algorithm. On the one hand, the initial probability function, determined by the pure visibility function, steers the optimization towards low phase deviations, but on the other hand the algorithm stays flexible and in principle, phase jumps are possible. If such a phase jump turns out to be essential or favorable for high quantum yields, this feature will survive, until potentially better properties are found, as in case of the probability maxima, which arises at iteration  $t \sim 200$  and completely vanishes after  $t \sim 300$ .

### 5.3 Conclusion

An optimization scheme for modulated laser pulses, controlling vibrational processes, based on ACO is presented [143]. This idea combines the advantages from previous control studies [134], using GAs as optimization routines. In the GA approach, parametrized and pixelated mask functions were applied, each variant exhibiting its own advantages and shortcomings. Learning from both concepts, a tunable correlation of the pixel values is introduced with the ACO method. The variant is flexible enough to tolerate necessary phase jumps, but to avoid strong phase fluctuations. Strong modulations will lead to unnecessarily long and complex pulses and can be suppressed in GA optimizations only for parametrized phase forms. Such a parametrized approach, however, cannot be applied for all control tasks [134]. The use of pixelated mask functions in

GA is contrarily most universal, but here only the magnitude of phase jumps can be reduced, the pixel values stay uncorrelated. Restrictions on the transmittance modulation are not reasonable at all, as they would lead to a loss in optimization flexibility. With the ACO method simple structured pulses, especially exhibiting significantly shorter pulse durations, are obtained, which is of high importance when efficient quantum gate operations or state-to-state transitions are optimized in the presence of dissipation. In addition, the information on the mechanism can already be deduced from the corresponding mask functions [Fig. 5.3 d), left]. The presented ACO scheme is directly transferable to quantum control experiments and it is suggested as an alternative to GAs [143].



# 6 Vibrational quantum gates under the influence of dissipation

A crucial factor for the maximum possible efficiency of vibrational quantum gate operations in condensed phase is the impact of dissipative effects. Vibrational relaxation within the qubit modes can take place and couplings to other vibrational degrees of freedom might occur. In this section the implementation prospects of mid-IR quantum gates in transition metal carbonyl complexes are studied in condensed phase based on experimental vibrational decay time scales. Corresponding control techniques are presented for the quantum gate optimizations in a dissipative environment. The robustness against vibrational relaxation of quantum gates optimized previously (Sec. 3.2.1) is studied. Additionally, quantum gates are optimized in the presence of dissipation, and the concept of precompiled quantum computing is presented and discussed.

## 6.1 Optimization under the influence of dissipation

The control calculations are performed with OCT operating in the time domain and with GAs in the frequency domain. The differences, which arise from the implementation of the density matrix formalism in the quantum dynamical calculations are briefly presented.

### 6.1.1 Optimization with OCT

For the density matrix formalism, the MTOCT functional in the eigenstate representation based on the dissipative Liouville-von Neumann equation (Eq. 1.25)

takes the form:

$$\begin{aligned}
 J(\boldsymbol{\rho}_{ik}(t), \boldsymbol{\sigma}_k(t), \varepsilon(t)) = & \sum_{k=1}^N \left\{ \langle\langle \boldsymbol{\rho}_{ik}(T) | \boldsymbol{\rho}_{fk} \rangle\rangle \right. \\
 & \left. - \int_0^T \left\langle \left\langle \boldsymbol{\sigma}_k(t) \left| \frac{\partial}{\partial t} + i[\mathcal{L}_H + \mathcal{L}_D] \right| \boldsymbol{\rho}_{ik}(t) \right\rangle \right\rangle dt \right\} \\
 & - \alpha_0 \int_0^T \frac{|\varepsilon(t)|^2}{s(t)} dt.
 \end{aligned} \tag{6.1}$$

The double-space notation  $\langle\langle \hat{A} | \hat{B} \rangle\rangle$  corresponds to the scalar product in Liouville space, which is equivalent to  $\text{Tr}(\hat{A}^\dagger \hat{B})$  in Hilbert space. The dissipative OCT functional (Eq. 6.1) is related to the form in the wave function representation (Eq. 1.60).  $\boldsymbol{\rho}_{ik}(t)$ ,  $\boldsymbol{\rho}_{fk}(t)$  are the initial and final states and  $\boldsymbol{\sigma}_k(t)$  are the Lagrange multipliers which correspond to the target states  $\boldsymbol{\rho}_{fk}(T)$  at the time  $t = T$ . The second term of Eq. 6.1 includes the dissipative Liouville-von Neumann equation (Eq. 1.25), with the two Liouvillian superoperators  $\mathcal{L}_H$  for the Hamiltonian part and  $\mathcal{L}_D$  for the dissipative part. The last term restricts the pulse fluence of the electric field  $\varepsilon(t)$  with the shape function  $s(t)$  and the penalty factor  $\alpha_0$ . For the shape function, the form:

$$s(t) = \sin^2\left(\frac{t}{T}\pi\right), \tag{6.2}$$

is used, with the time  $t$  running from 0 to  $T$ . By variational calculus the equations of motion of the initial and final states as well as the construction of the laser fields can be derived (Eqs. 6.3, 6.4 and 6.5).

$$i \frac{\partial}{\partial t} \boldsymbol{\rho}_{ik}(t) = (\mathcal{L}_H + \mathcal{L}_D) \boldsymbol{\rho}_{ik}(t) \tag{6.3}$$

$$i \frac{\partial}{\partial t} \boldsymbol{\sigma}_k(t) = (\mathcal{L}_H + \mathcal{L}_D)^\dagger \boldsymbol{\sigma}_k(t) \tag{6.4}$$

$$\varepsilon(t) = \frac{s(t)}{\alpha_0} \Im \langle\langle \boldsymbol{\sigma}_k(t) | \boldsymbol{\mu} | \boldsymbol{\rho}_{ik}(t) \rangle\rangle \tag{6.5}$$

These equations are solved iteratively, according to the scheme introduced in Sec. 1.3.3. For all dissipative OCT calculations in this chapter, the propagations are performed with the Faber propagator, presented in Sec. 1.1.4.

### 6.1.2 Optimization with genetic algorithms

The GA optimization strategy of quantum processes including dissipative effects is equal to the method used in Chapter 3. The only difference is the dissipative Liouville-von Neumann equation (Eq. 1.25) instead of the time-dependent Schrödinger equation (Eq. 1.5). In contrast to the OCT calculations, where the Faber propagator is applied, here a different propagation scheme is used, since significantly more propagations have to be performed when using GA-based optimization strategies.

In case of OCT calculations, the number of propagations  $n(p)$  is equal to  $n(p) = 3 \cdot n(T) \cdot n(I)$ , where  $n(T)$  is the number of transitions to be optimized and  $n(I)$  corresponds to the number of iterations (which is normally on the order of 100). The factor 3 results from the approach used to solve the coupled differential equations (Eqs. 6.3, 6.4 and 6.5). For GA calculations the number of propagations is  $n(p) = n(T) \cdot n(G) \cdot n(P)$ , scaling with the chosen population size  $n(P)$  and the number of generations  $n(G)$ . The quantity  $n(G) \cdot n(P)$  is usually applied on the order of  $3 \cdot 10^4 - 1 \cdot 10^5$ . Consequently, a fast propagation scheme is needed and as in case of the wave packet propagation, a SPO propagation scheme is introduced. Similar approaches have been applied for the grid basis [144, 145, 146].

In the eigenstate representation, the coherent propagation of a density matrix can be performed in the Hilbert space ( $\mathcal{H}$ ) according to Eq. 1.14:

$$\boldsymbol{\rho}(t_j) = |\Psi(t_j)\rangle\langle\Psi(t_j)| \quad (6.6)$$

$$= \mathbf{U}(\Delta t)|\Psi(t_i)\rangle\langle\Psi(t_i)|\mathbf{U}(\Delta t)^\dagger \quad (6.7)$$

$$= \mathbf{U}(\Delta t)\boldsymbol{\rho}(t_i)\mathbf{U}(\Delta t)^\dagger \quad (6.8)$$

$$= \mathbf{U}_{\text{sys}} \mathbf{U}_{\text{int}} \mathbf{U}_{\text{sys}} \boldsymbol{\rho}(t_i) \mathbf{U}_{\text{sys}}^\dagger \mathbf{U}_{\text{int}}^\dagger \mathbf{U}_{\text{sys}}^\dagger \quad (6.9)$$

$$= \mathbf{U}_{\text{coh}} \boldsymbol{\rho}(t_i) \mathbf{U}_{\text{coh}}^\dagger, \quad (6.10)$$

with the propagator for the molecular part:

$$\mathbf{U}_{\text{sys}} = e^{-i\mathbf{H}_0 \frac{\Delta t}{2}}, \quad (6.11)$$

and for the laser-molecule interaction part:

$$\mathbf{U}_{\text{int}} = \mathbf{X}^\dagger e^{i\boldsymbol{\mu}^{\text{diag}}_{\varepsilon(t_i)} \Delta t} \mathbf{X}. \quad (6.12)$$

When dissipative effects are to be treated explicitly, these parts have to be propagated, according to:

$$(\dot{\rho}(t))_D = \mathcal{L}_D \rho(t), \quad (6.13)$$

$$\rho(t_j) = \mathbf{U}_{\text{diss}} \rho(t_i) = e^{\mathcal{L}_D \Delta t} \rho(t_i), \quad (6.14)$$

which is performed in the Liouville space here and is denoted by the label ( $\mathcal{L}$ ) in the following. The Liouville space is a unitary vector space, where each linear operator from the Hilbert space corresponds to a vector. A dissipative propagation step is evaluated according to:

$$\rho(t_j) = \mathbf{U}_{\text{coh}}^{(\mathcal{H})} \mathbf{T}^{\mathcal{H} \rightarrow \mathcal{L}} \left( \mathbf{V}^{(\mathcal{L})} e^{\mathcal{L}_D^{\text{diag}(\mathcal{L})} \Delta t} \mathbf{V}^{-1(\mathcal{L})} \rho^{(\mathcal{L})}(t_i) \right) \mathbf{T}^{\mathcal{L} \rightarrow \mathcal{H}} \mathbf{U}_{\text{coh}}^{\dagger(\mathcal{H})}, \quad (6.15)$$

with the superscript index denoting either the Hilbert ( $\mathcal{H}$ ) or the Liouville ( $\mathcal{L}$ ) spaces, respectively. The coherent propagators are composed of the molecular Hamiltonian part ( $\mathbf{U}_{\text{sys}}$ ) and laser-molecule interaction ( $\mathbf{U}_{\text{int}}$ ) part:  $\mathbf{U}_{\text{coh}}^{(\mathcal{H})} = \mathbf{U}_{\text{sys}} \mathbf{U}_{\text{int}} \mathbf{U}_{\text{sys}}$  (Eqs. 6.9 and 6.10). The transformation matrices  $\mathbf{T}^{\mathcal{H} \rightarrow \mathcal{L}}$  and  $\mathbf{T}^{\mathcal{L} \rightarrow \mathcal{H}}$  are necessary to transform the density matrix from the Hilbert to the Liouville space and back, since  $\rho$  is a vector in the Liouville space. The matrices  $\mathbf{V}^{(\mathcal{L})}$  and its inverse  $\mathbf{V}^{-1(\mathcal{L})}$  diagonalize the dissipative part  $\mathcal{L}_D$  and transform it back. In this case the inverse matrix is explicitly calculated, since  $\mathbf{V}^{(\mathcal{L})}$  is not a unitary matrix and the transposed form does not equal the inverse matrix. The dissipative part  $\mathcal{L}_D(\rho(t))$  is constructed according to the Lindblad expression (Eq. 1.26) in the Hilbert space and is transferred to the Liouville space to obtain  $\mathcal{L}_D$ , which corresponds to a real, non-symmetric matrix.

## 6.2 Results and discussion

As a first study, the robustness of the quantum gate operations, optimized in the absence of dissipative effects, are investigated and discussed. A further question is, how efficient the gates can be implemented in the condensed phase with the help of optimization techniques. The last part introduces the concept of pre-compiled quantum computing, which might become necessary in the condensed phase for the realization of efficient quantum algorithms based on vibrational qubits.

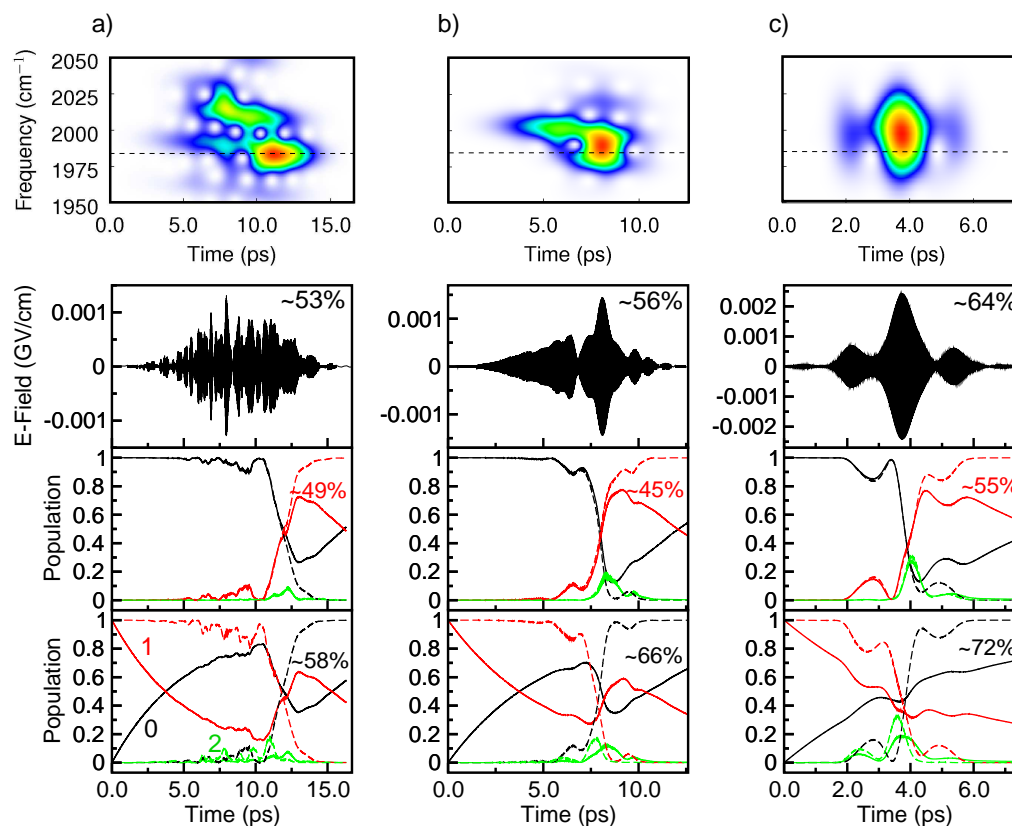


**Figure 6.1:** Vibrational NOT gates operating on the  $T_{1u}$  mode of  $W(CO)_6$ , calculated with GAs in Sec. 3.2.1 [a) corresponds to Fig. 3.3 a), b) to Fig. 3.3 b) and c) to Fig. 3.3 c)]. The upper panels show the FROG representation of the electric fields depicted in the second row. In the last two rows the induced mechanisms are shown, where the solid lines refer to the propagation in a dissipative environment and the dashed lines to the non-dissipative case for comparison. The black lines indicate the population of the vibrational ground state, the red lines refer to the first excited state and the green lines to the second overtone.

### 6.2.1 Robustness of quantum gates against dissipation

From an experimental study on the vibrational excitation of  $W(CO)_6$  [70] in *n*-hexane the vibrational life time of the  $T_{1u}$  mode is known. It consists of a long-time component corresponding to the vibrational relaxation of the  $T_{1u}$  mode

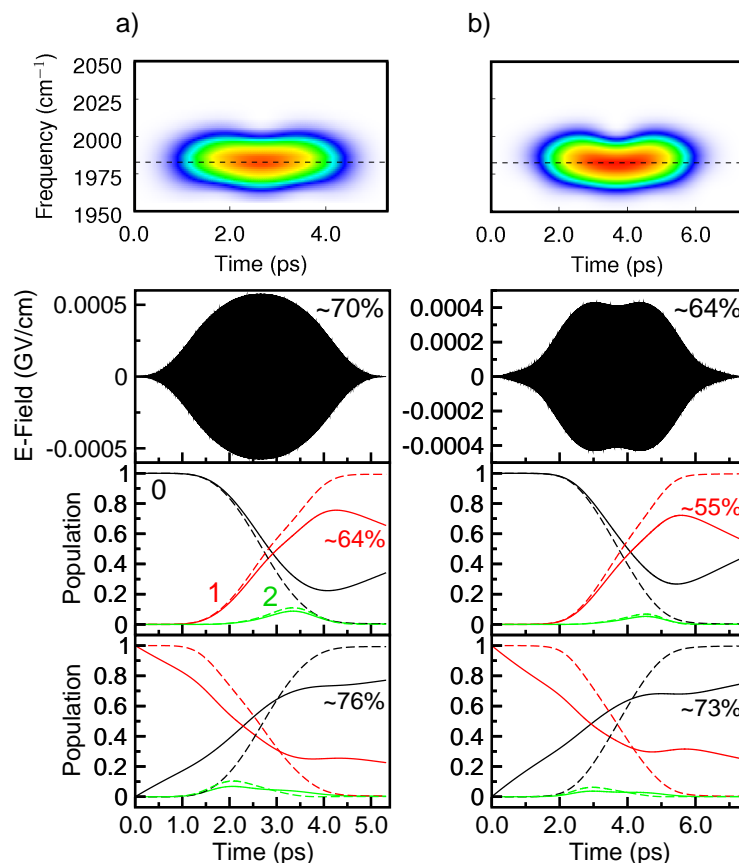


**Figure 6.2:** Vibrational NOT gates operating on the  $T_{1u}$  mode of  $W(CO)_6$ , calculated with OCT for a non-dissipative environment. The upper panels show the FROG representation of the electric fields depicted in the second row with pulse durations of a) 5.3 ps and b) 7.4 ps. In the last two rows the induced mechanisms are shown, where the solid lines refer to the propagation in condensed phase and the dashed lines to a non-dissipative environment. The black lines indicate the population of the vibrational ground state, the red lines refer to the first excited state and the green lines to the second overtone.

and a fast decay component. Earlier studies suggest that the fast component can be referred to an intermode energy transfer from the probed  $T_{1u}$  mode to the Raman active  $E_g$  mode [129]. From a biexponential fit of the vibrational decay, the two  $T_1$  times:  $T_1 = 152$  ps and  $T_1 = 5.6$  ps can be deduced for the  $T_{1u}$  mode in condensed phase and are applied in this theoretical study. As indicated in the experimental work [70], the  $T_1$  times scale nearly harmonically, i.e. they scale with the vibrational quantum number. Such a progression is used to set up the Lindblad operators (Eq. 1.27) for the dissipative matrix ( $\mathcal{L}_D$ ). The  $T_2$  times can be retrieved from homogeneous linewidths of excitation spectra and the corresponding pure dephasing time scales can be calculated according to the equation:  $\frac{1}{T_2} = \frac{1}{2T_1} + \frac{1}{T_2^*}$ . For the presented calculations, the pure dephasing time scale were not taken into account, but their influence on quantum information processing will be discussed.

The robustness of different laser fields acting as vibrational NOT gates in the  $T_{1u}$  mode of  $W(CO)_6$  are investigated. The quantum system is propagated using the Faber scheme (Sec. 1.1.4), with the three laser pulses, optimized as NOT gates for a non-dissipative environment [Fig. 3.3 a), b) and c)]. These fields are also shown in Fig. 6.1 together with their FROG representations. The induced mechanisms in condensed phase (solid lines) are compared to the ones without dissipation (dashed lines) in the lower two rows, where the pulse is operating on the vibrational ground state (black line, last but one row) and on the first vibrational excited state (red line, last row). The population of the overtone state  $v = 2$  is indicated by the green line. The dissipation strongly reduces the efficiency of the quantum gate operations in all three cases. The efficiency refers here to the population transfer yield and is not meant as the purity of the quantum state. The dissipative quantum yields of the single processes are given in the respective mechanism panels (in red for the excitation process  $|0\rangle \rightarrow |1\rangle$  and black for  $|1\rangle \rightarrow |0\rangle$ ). The NOT gate efficiency in condensed phase is calculated as the average yield of both single excitation processes and given in the panels depicting the laser fields.

Due to the strong impact of the dissipation, the robustness of the laser fields against the vibrational decay can be clearly traced, and which pulse features play the major role for the robustness can be studied. In general, quantum gate solutions can differ in the amount of intermediate overtone excitation, the pulse duration and the complexity of the envelope functions.

The amount of overtone excitation is relatively low in all three cases and is

here obviously independent of the spectral widths of the pulses. This can be understood from the FROG representations (upper panels of Fig. 6.1). The dashed lines indicate the energy of the fundamental transition  $|0\rangle \rightarrow |1\rangle$  of the  $T_{1u}$  mode at  $1983\text{ cm}^{-1}$ . The major spectral part is shifted to higher frequencies and in contrast the overtone transitions  $|1\rangle \rightarrow 2, 2 \rightarrow 3 \dots$  have lower frequencies, which is the reason for the low degree of intermediate population transfer to higher lying vibrational states.

Fig.	6.1 a)	6.1 b)	6.1 c)	6.2 a)	6.2 b)
pulse duration [ps]	16.4	12.6	7.4	5.3	7.4
$ 0\rangle \rightarrow  1\rangle$ [%]	48.5	45.0	55.4	64.7	55.5
$ 1\rangle \rightarrow  0\rangle$ [%]	57.6	66.0	72.2	76.0	73.9
NOT [%]	53.0	55.5	63.8	70.4	64.7
$t_{\text{switch}}$ [ps]	4.2	4.6	3.5	2.4	3.3

**Table 6.1:** Pulse parameters and quantum efficiencies for the NOT gates depicted in Fig. 6.1 and Fig. 6.2.

The three depicted NOT gate solutions (Fig. 6.1) mainly differ in the pulse duration (given in Tab. 6.1) and in the complexity. The overall NOT gate efficiency (shown in the panels of the laser pulses) increases from case a) to c) with decreasing pulse duration [from a) 16.2 ps to c) 7.3 ps] and decreasing pulse complexity. Also the efficiencies of the single excitation processes  $|0\rangle \rightarrow |1\rangle$  and  $|1\rangle \rightarrow |0\rangle$  are higher in case c) compared to a). But, for the  $|0\rangle \rightarrow |1\rangle$  excitation referring to the pulse depicted in Fig. 6.1 b) the efficiency is lower than for the longer and more complex pulse shown in Fig. 6.1 a). The explanation can be given by analyzing the period of time between the qubit basis switching process, which corresponds to the crossing point of the populations in the qubit basis states  $|0\rangle$  and  $|1\rangle$  and the end of the laser-molecule interaction. This duration is determined for the three pulses in Fig. 6.1 and given as the time  $t_{\text{switch}}$  in Tab. 6.1. It is longer in case of the NOT gate shown in Fig. 6.1 b) than for a) and explains the reduced efficiency of the  $|0\rangle \rightarrow |1\rangle$  transition in case of the laser field b). In general, one of the most intense subpulses induces the population inversion from the initial to the target state and when strong dissipative effects are present, then the pulse decay from this point in time has to be preferably fast. Usually this means that the total pulse duration is short.

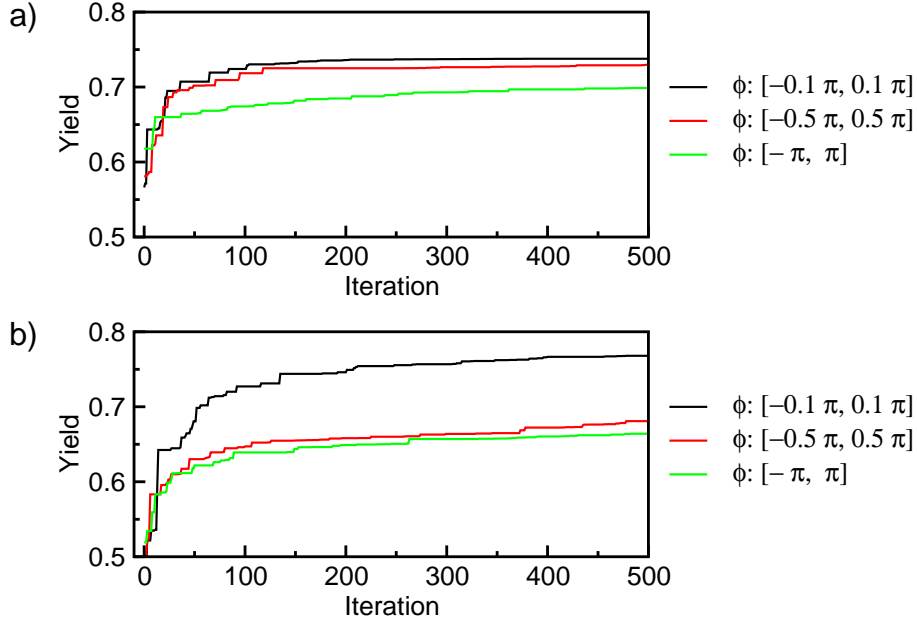


**Figure 6.3:** Quantum efficiencies of the pixel-based GA optimization of a NOT gate operation. a) The FL pulse durations were chosen in the range from 300 fs to 3000 fs and b) from 50 fs to 100 fs. In both cases the phase range  $[-\pi, \pi]$  was limited by a factor  $f$ , where the quantum yields for  $f = 0.1$  are indicated by the black lines, for  $f = 0.5$  by the red lines and for  $f = 1.0$  by the green lines.

This finding is compared to a simple structured OCT result shown in Fig. 6.2 a). The NOT gate is optimized using MTOCT (Eq. 1.60, efficiency  $> 99\%$ ,  $\alpha_0 = 200$ ) without taking into account dissipative effects and afterwards the system is propagated in the presence of dissipation. The pulse duration of the almost Gaussian-shaped laser field is 5.3 ps, which is  $\sim 2$  ps shorter than the shortest NOT gate shown in Fig. 6.1 c). Again, the FROG representation is displayed [Fig. 6.2 a)], which indicates a narrower spectral range than for the previously discussed NOT gates (Fig. 6.1). The pulse action is not as sensitive to dissipation as observed in the previous cases, and the efficiency decreases only to 70.4%. The short duration  $t_{\text{switch}} \sim 2.4$  ps is the reason for the lower impact of the vibrational decay on the population transfer mechanisms.

Furthermore, it needs to be clarified, if only the pulse duration is decisive for

the efficiency reached in the presence of vibrational dissipation or if additionally the pulse complexity plays a role. To answer this question, a NOT gate with a pulse duration of 7.4 ps, the same duration as the GA result in Fig. 6.1 c), is optimized with OCT ( $\alpha_0 = 200$ ) in a non-dissipative environment. Afterwards the OCT solution is propagated with dissipation. The resulting pulse, the FROG representation and the induced mechanisms are depicted in Fig. 6.2 b). The relevant data are also given in Tab. 6.1. The structures of the OCT and GA fields [Fig. 6.1 c) and Fig. 6.2 b)] with the same pulse duration differ significantly. Besides the pulse duration, also the  $t_{\text{switch}}$  time is almost the same, i.e. 3.3 ps in the case of the OCT calculation. Accordingly, the  $|0\rangle \rightarrow |1\rangle$  excitation processes are equally efficient. The total quantum yield of the NOT gate operation amounts to 64.7%, which is only  $\sim 0.9\%$  better than the NOT gate presented in Fig. 6.1 c).

In conclusion, when the amount of intermediate overtone excitation is low, especially for the transition  $|0\rangle \rightarrow |1\rangle$ , the pulse duration and particularly the  $t_{\text{switch}}$  duration determines the strength of the dissipative impact. The example presented demonstrates that the actual structure of the laser field envelopes and their complexities play only a minor role.

### 6.2.2 Quantum gate optimization in a dissipative environment

A further important point is whether the efficiencies, reached by the pulses in Sec. 6.2.1, can be enhanced by optimization techniques in the presence of dissipation. In a previous theoretical work such a question has been investigated, based on optimal control of dissipative dynamics in the context of molecular quantum computing with OCT [63]. The authors optimized quantum gate operations in the presence of dissipation and compared them to laser fields optimized without dissipation but propagated afterwards in the presence of dissipation. They could conclude that dissipative OCT basically does not improve the results gained from non-dissipative optimization. Similar OCT investigations have been performed on the vibrational excitation of CO molecules adsorbed on metal surfaces [147, 148, 149]. In contrast, this study focuses on dissipative OCT and GA optimizations. Here, the role of the pulse durations and penalty factors as well as of the incident laser pulses is investigated to obtain as efficient laser fields as possible, driving the quantum gate operations in condensed phase.

With the pixel-based GA approach, introduced in Chapter 3 and the SPO propagation scheme, presented in Sec. 6.1.2, NOT gate optimizations were performed in the condensed phase (with  $T_1$  and  $T_2 = 2 \cdot T_1$ ). In all calculations a spectral pixel width of  $10 \text{ cm}^{-1}$  was assumed.

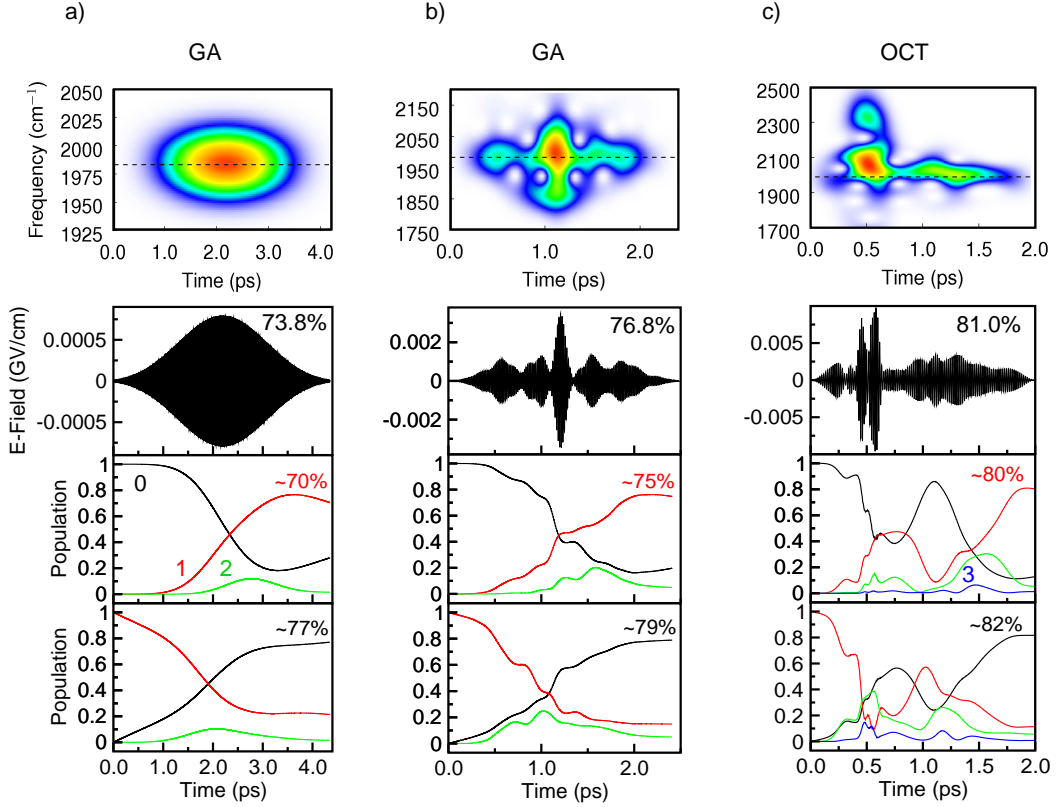


**Figure 6.4:** Optimized NOT gates in condensed phase. In the optimization the dissipative environment is explicitly taken into account. The laser fields in a) and b) are optimized with a GA and in case of c) with OCT. The panels show the FROG representations, the electric laser fields and the induced population transfer mechanisms (from top to bottom).

The number of generations is 500 and the size of population 60. As already discussed in Chapter 3, the genome of the GA comprises the mask function pixels and the FL pulse parameters. The maximum FL pulse energy  $\varepsilon_0$  is chosen to be below  $0.01 \text{ au} \approx 0.05 \text{ GV/cm}$  and the carrier frequency  $\omega_c$  is in the range

from  $1970\text{ cm}^{-1}$  to  $1990\text{ cm}^{-1}$ . The phase range  $[-\pi, \pi] \cdot f$  was varied in the calculations with the factor  $f$  and additionally two different ranges for the FL pulse durations were applied and compared. In the first set of calculations, the FWHM of the FL pulses were chosen between 300 fs and 3000 fs (similar to the ranges used in Chapters 3 and 4). In the second case, the durations were shortened to 50 fs to 100 fs (similar FL pulse durations are frequently used in the experiment, e.g. in [70]). The obtained maximum quantum yields are displayed in Fig. 6.3, where the panel a) shows the results for longer FL pulse durations and b) for the shorter ones.

Again, the choice of limited phase ranges very obviously benefits the GA search. For the smallest range used [ $f = 0.1$ , black line in Fig. 6.3 a)], a maximum efficiency of 73.8% is reached for a NOT gate with a duration of 4.3 ps. The pulse is depicted in Fig. 6.4 a), together with the FROG representation and the induced mechanisms. The quantum efficiency is slightly better than for the initially non-dissipative OCT-optimized NOT gate [Fig. 6.2 a)], this is mainly due to the fact that the pulse duration is 1 ps shorter. When optimizing the vibrational quantum processes in the presence of dissipation with GAs, the differing possible pulse durations, in contrast to OCT, is an advantage of the GA approach. The pulse durations are not chosen manually, as in case of OCT, but determined indirectly by the FL pulse and mask function properties, which are optimized by the algorithm.

If shorter FL pulse durations [50 fs-100 fs, Fig. 6.3 b)] are selected for the dissipative GA optimizations, two differences to the previous calculations with longer FL pulses [300 fs-3000 fs, Fig. 6.3 a)] can be observed. The quantum efficiencies increase to 76.8% [Fig. 6.3 b)] in comparison to a maximum of 73.7% [Fig. 6.3 a)] and the influence of the phase limitation by the factor  $f$  is higher. The latter point can be understood as follows. In all calculations the same pixel width of  $10\text{ cm}^{-1}$  is applied. Since the spectra of shorter FL pulses are broader, more pixels are needed for the mask functions. The variations in the phase and transmittance functions can consequently affect the pulse complexities and durations stronger. Thus, strictly confined phase ranges facilitate lower phase variations over the broad pixel masks and benefit the GA search even more than for longer FL pulse durations.

From the GA calculation [Fig. 6.3 b)], it can be traced that despite the broad spectrum, short FL pulses are equally suited as longer FL pulses for the quantum gate calculations (in this case even slightly better), but the restriction of the

phase domain is now even more relevant. The best GA solution for the short FL pulse range with  $f = 0.1$  is depicted in Fig. 6.4 b) with the FROG and the mechanisms. However, it needs to be mentioned that the strategy of the usage of short FL pulses cannot be pursued for every qubit system. It is possible if there are few IR active normal modes, as for  $W(\text{CO})_6$ , or if the modes are still resolvable by the pulse.

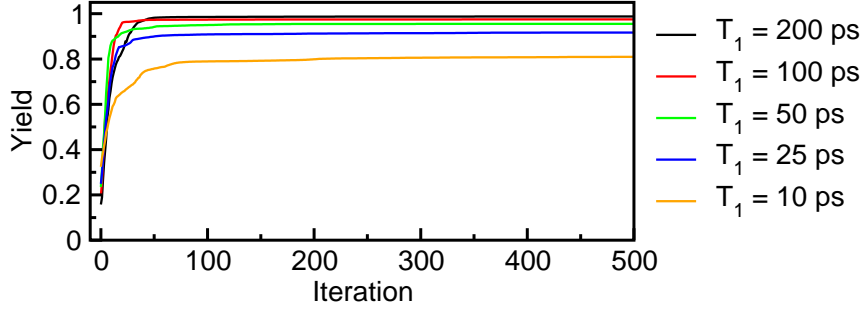


**Figure 6.5:** A scan of  $T_1$  times is performed for the NOT gate implementation with the aim to find the minimum decay time scale, which still allows for an efficient implementation of a NOT gate operation.

$\alpha_0$	100	50	10	5	3	2
quantum yield [%]	66.7	73.6	79.9	80.6	80.7	81.0

**Table 6.2:** Resulting quantum yields of the OCT optimized NOT gates in condensed phase, depending on the penalty factor  $\alpha_0$ .

For corresponding dissipative OCT calculations, the laser-molecule interaction time has to be defined explicitly and cannot be altered or optimized by the OCT formalism. Based on the best GA result [Fig. 6.4 b] with a pulse duration of 2.4 ps, the OCT pulse duration is limited to 2.0 ps to find out if further enhancements are possible by decreasing the duration. In addition the penalty factor  $\alpha_0$  has to be determined. It is scanned in these calculations from 2 to 100 and the results are given in Tab. 6.2. Below the value  $\alpha_0 = 2$  the resulting laser fields are physically not meaningful, i.e. not realizable in the experiment. Starting with larger  $\alpha_0$  values, the solutions are simple structured, but with low

efficiencies. For the penalty factor  $\alpha_0 = 2$ , the highest efficiency is reached and the result is depicted in Fig. 6.4c). Since the pulse duration is slightly shorter than in case of the best GA solution, the OCT result is more complex, but also more efficient with 81%. The spectrum is very broad and as can be deduced from the mask function calculations, a FL pulse with a FWHM below 50 fs is required. From the mechanisms and the FROG representation the high efficiency of the quantum gate can be attributed to the fact that the predominant switching process occurs only  $\sim 570$  fs before the laser-molecule interaction is over.

From the calculations presented in this section, it can be concluded that for the given dissipative time scales, comprising also a fast component of 5.6 ps, a vibrational NOT gate could be implemented in condensed phase still with acceptable population transfer efficiencies for an experimental proof of principle. Additionally, it was found that the results gained from GA and OCT optimizations conform very well, with respect to the efficiencies, the pulse durations and the complexities.

Now, a further question arises on how long the  $T_1$  time scales need to be for the implementation of highly efficient quantum gates in the condensed phase. Corresponding calculations were performed with the pixel-based GA approach for a NOT gate. The phase range was again limited to  $[-0.1\pi, 0.1\pi]$  to accelerate the GA search. The vibrational decay was assumed to be monoexponential with  $T_1$  times reaching from 10 ps to 200 ps. The quantum yields reached in the GA runs are depicted in Fig. 6.5, and it can clearly be traced that for  $T_1 \geq 200$  ps highly efficient vibrational quantum gates can be implemented, even in condensed phase. This seems to be very realistic, as the vibrational decay time e.g. of the  $A_1$  symmetric mode in  $\text{MnBr}(\text{CO})_5$  is monoexponential with  $T_1 \sim 200$  ps [150].

As already indicated, the  $T_2^*$  time scales can be deduced from homogeneous linewidths and incorporated in the theoretical study. The decay rate associated with  $T_2$  then changes from  $\frac{1}{T_2} = \frac{1}{2T_1}$  to  $\frac{1}{T_2} = \frac{1}{2T_1} + \frac{1}{T_2^*}$ . From Eq. 1.30 the influence of the  $T_2^*$  time and the corresponding rate  $\gamma^*$  can be seen. It diminishes the size of the off-diagonal elements  $\rho_{nm}$  ( $n \neq m$ ) of the density matrix, i.e. it reduces the coherence of the quantum state additionally to the  $T_1$  relaxation. The amount of coherence can be determined by the purity of the state ( $\text{Tr}(\rho^2)$ ). As an effective laser-molecule interaction is only possible with the coherent part of the quantum system, long  $T_2^*$  times are favorable for the implementation of quantum gates.

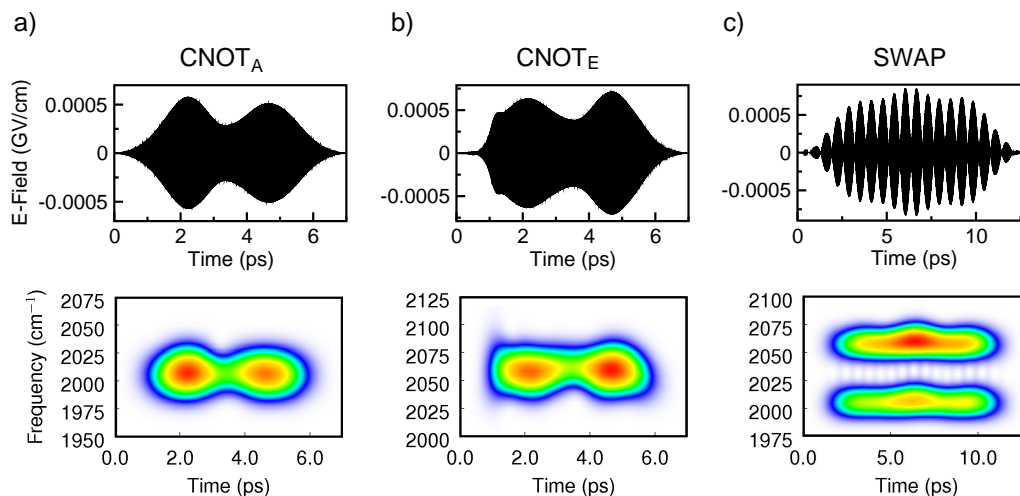


**Figure 6.6:** Optimized CNOT laser fields in dissipative environment operating a) on the  $A_1$  mode, b) on the E mode of  $\text{MnBr}(\text{CO})_5$  and c) a respective SWAP operation. The upper row shows the laser fields and the corresponding FROGs are depicted in the lower row.

### 6.2.3 Precompiled quantum computing

The notion of precompiled quantum computing means that quantum algorithms are not composed of universal quantum operations (as done in universal quantum computing), instead either the complete algorithm or a part of it (e.g. a QFT or a SWAP operation) is implemented as one unitary operation [67]. This idea has been proposed e.g. for molecular quantum computing with vibronic superpositions in electronically excited states [67, 151, 152, 153].

If molecular quantum computing with vibrational qubits is realized in gas phase experiments, the  $T_1$  and  $T_2$  time scales will be longer than they are in condensed phase. To demonstrate the advantage of the precompiled concept, the time  $T_1 = 200$  ps is used in the calculations, where the effect will be stronger than for the longer gas phase time scales. As an example, a SWAP gate operation, which is composed of three CNOT gates in universal quantum

computing, is discussed:

$$\text{SWAP} = \text{CNOT}_1 \cdot \text{CNOT}_2 \cdot \text{CNOT}_1 \quad (6.16)$$

$$= \begin{pmatrix} 1 & 0 & 0 & 0 \\ 0 & 1 & 0 & 0 \\ 0 & 0 & 0 & 1 \\ 0 & 0 & 1 & 0 \end{pmatrix} \cdot \begin{pmatrix} 1 & 0 & 0 & 0 \\ 0 & 0 & 0 & 1 \\ 0 & 0 & 1 & 0 \\ 0 & 1 & 0 & 0 \end{pmatrix} \cdot \begin{pmatrix} 1 & 0 & 0 & 0 \\ 0 & 1 & 0 & 0 \\ 0 & 0 & 0 & 1 \\ 0 & 0 & 1 & 0 \end{pmatrix} \quad (6.17)$$

$$= \begin{pmatrix} 1 & 0 & 0 & 0 \\ 0 & 0 & 1 & 0 \\ 0 & 1 & 0 & 0 \\ 0 & 0 & 0 & 1 \end{pmatrix}. \quad (6.18)$$

For the qubit basis  $\{|00\rangle, |01\rangle, |10\rangle, |11\rangle\}$ , it interchanges the qubits states  $|01\rangle$  and  $|10\rangle$ :

$$\begin{pmatrix} 1 & 0 & 0 & 0 \\ 0 & 0 & 1 & 0 \\ 0 & 1 & 0 & 0 \\ 0 & 0 & 0 & 1 \end{pmatrix} \cdot \begin{pmatrix} \psi_{00} \\ \psi_{01} \\ \psi_{10} \\ \psi_{11} \end{pmatrix} = \begin{pmatrix} \psi_{00} \\ \psi_{10} \\ \psi_{01} \\ \psi_{11} \end{pmatrix}. \quad (6.19)$$

With dissipative OCT (Eq. 6.1) two CNOT gates, one operating on the  $A_1$  symmetric mode and the other one on an E symmetric mode of  $\text{MnBr}(\text{CO})_5$  were optimized with pulse durations of 7 ps. In addition, a direct SWAP operation according to Eq. 6.18 was calculated, where a total duration of 13 ps was used. The quantum operations are displayed in Fig. 6.6. The CNOT gates [Fig. 6.6 a) and b)] can basically be realized by two subpulses, overlapping in time, with the same carrier frequency  $\omega_c$ . For the  $\text{CNOT}_A$  gate the carrier frequency is  $\omega_c \sim 2005 \text{ cm}^{-1}$  and  $\omega_c \sim 2060 \text{ cm}^{-1}$  for the  $\text{CNOT}_E$  gate. In contrast, the SWAP laser field [Fig. 6.6 c)] contains both frequency components at the same time as can be seen from the FROG (lower panel). This is the reason for the beat structure of the pulse envelope function (upper panel). The average efficiency of the precompiled SWAP operations is 94.3% and the corresponding induced population transfer mechanisms are depicted in Fig. 6.7 b). For the universal SWAP, composed of the CNOT gates, the system is propagated with the CNOT gate laser fields, which are delayed in time for phase correctness [49]. After the first  $\text{CNOT}_A$  gate, a delay of 3.4 fs is necessary, then the  $\text{CNOT}_E$  gate is operating, followed by a 3.2 ps time delay and the second  $\text{CNOT}_A$  gate. The average

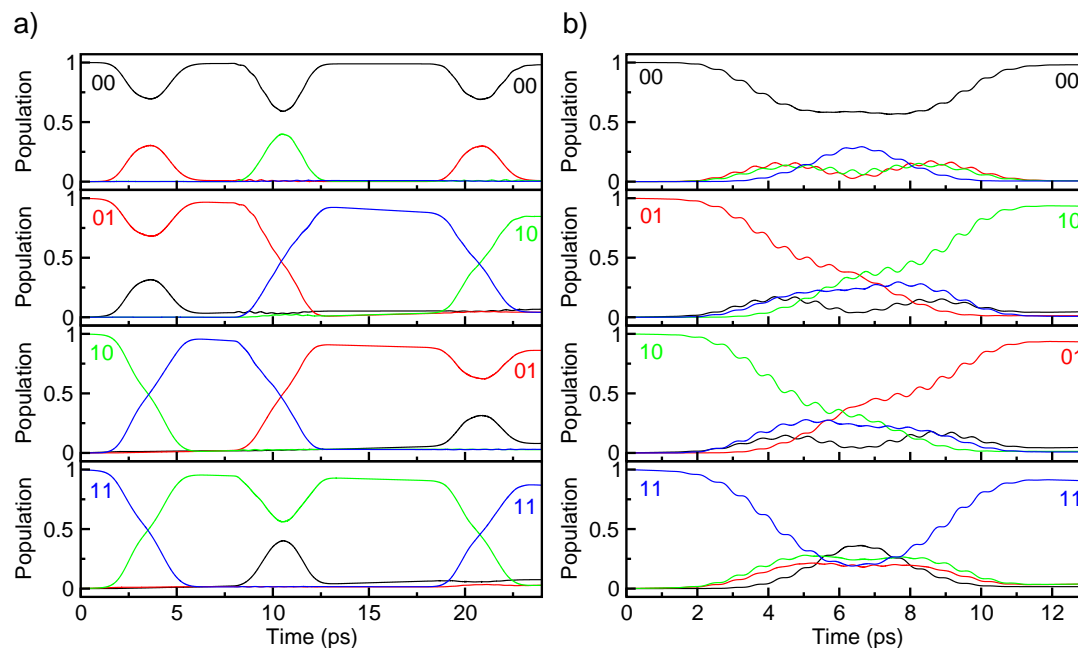


**Figure 6.7:** Mechanism of a) a universal and b) a precompiled SWAP operation, with the two-qubit basis states  $|00\rangle$  (black),  $|01\rangle$  (red),  $|10\rangle$  (green), and  $|11\rangle$  (blue).

quantum efficiency is 88.8% and the mechanism is depicted in Fig. 6.7 a). The interaction of the distinct CNOT gates with the qubit system and the corresponding switching processes at the times  $t \sim 3.5$  ps, 10.5 ps and 21.0 ps [Fig. 6.7 a)] can be clearly observed. The precompiled SWAP operation is directly driven, and the qubit basis states  $|00\rangle$  and  $|11\rangle$  are here intermediately used as transition pathways. The higher efficiency of the precompiled operation ( $\sim 5.5\%$ ) has to be attributed mainly to the short pulse duration, which is roughly half as long as for the universal SWAP gate. Since in gas phase the vibrational life times will be longer, the effect of precompiled quantum computing will be reduced, but it will still help to enhance the quantum efficiencies.

## 6.3 Conclusion

In this study, the efficiency of logic operation in the mid-IR regime on vibrational qubits were investigated in the presence of dissipation. The vibrational relaxation time scales were directly taken from the experiment. The implementation prospects of NOT gates for  $\text{W}(\text{CO})_6$  in the condensed phase were studied to get an idea on the maximum efficiency of future quantum control experiments.

The robustness of laser fields, which were optimized in the absence of vibrational relaxation, were explored by propagation in a dissipative environment. It can be concluded that predominantly the pulse duration accounts for the strength of the dissipative impact. From dissipative GA optimizations, it can be learned that a broad range of FL pulse properties will be suited for the quantum control experiments. The phase limitation, however, is still a very important issue, especially, when short FL pulse durations are chosen. The best solutions for shorter FL pulses are not inherently found by the GA, but the search is still promoted significantly by the limitation of the phase range.

A scan on required  $T_1$  times showed that a time scale of  $\sim 200$  ps will be sufficient for highly efficient quantum gate implementations and promising experimental results are to be expected for the  $A_1$  mode of  $\text{MnBr}(\text{CO})_5$ . Additionally, the concept of precompiled quantum computing was presented and its advantages were discussed for the example of a SWAP operation.

## 7 Molecular chains for vibrational quantum information processing

Population transfer between vibrational eigenstates is an important process for several phenomena in chemistry and physics. Intramolecular vibrational redistribution (IVR) has been studied in many different systems, such as protein molecules [154, 155], charge transport in molecular wires [156, 157, 158], transport of excitons in macromolecules [159, 160], transport of heat and energy in chain molecules [161, 162, 163, 164] or other molecular systems [165, 166, 167, 168]. A comprehensive review on energy transfer dynamics can be found in [169].

After a local vibrational excitations of molecules, IVR processes can be studied with time-resolved pump probe techniques. Particularly, multi-dimensional IR spectroscopy [170, 171, 172, 173, 174, 175] facilitates an insight into the vibrational dynamics. Besides the time resolution, also technical advances have been reached in the spatial resolution of spectroscopic techniques, e.g. optical nearfield control in nanostructures [176, 116]. On the basis of all these new developments, the precise detection and control of vibrational energy transfer processes in molecules will become possible in future.

For the concept of molecular quantum computing with vibrational qubits an approach to scale the number of qubits is necessary for the construction of quantum registers. One possibility is that more than two normal modes of a molecule are used to define the qubit modes and to set up a multi-qubit system for a single molecule. But as not all normal modes are strongly IR (or Raman) active and resolvable at the same time, the size of the qubit system is generally limited. A different idea is based on the connection of individual qubit systems through molecular chains. This study focuses on a laser-driven vibrational energy transfer across such bridging molecules. The process can then be regarded as information transfer in the context of molecular quantum information processing with vibrational qubits.

The idea is related to one-dimensional spin chains acting as quantum channels [177, 178]. The generation of entanglement and the transport of quantum information has already been investigated in such systems [179]. In this study, the aim is to implement a laser-driven vibrational state transfer from one qubit site to another one across the molecular chain states. A model system is set up based on the linear octatetraene molecule, which is described by ab-initio methods. Two qubit systems are coupled to the chain, and laser fields are calculated with OCT, driving an efficient state transfer. Additionally, vibrational relaxation is incorporated in the study.

## 7.1 Approach for quantum information processing with vibrational qubits

As a first approach to quantum information transfer across an octatetraene chain (Fig. 7.1), a model system is constructed in the basis of stretching local modes. The molecular geometry is optimized quantum chemically using DFT

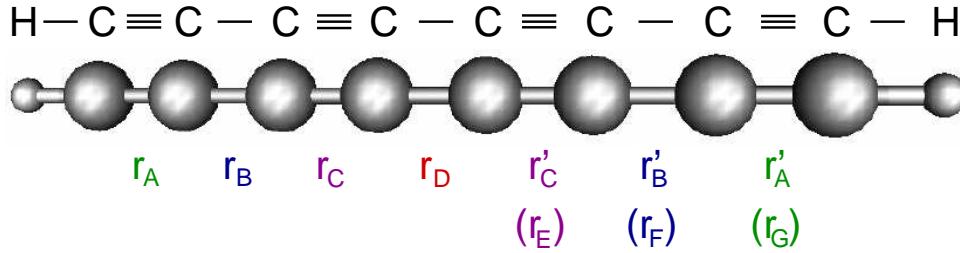


**Figure 7.1:** Octatetraene chain with the local mode coordinates  $q_i$  referring to the displacement of the C-C bondings, with the equilibrium bond lengths  $r_i$ .

(bp86/6-31G(d,p)) [180]. Along each local mode (explicitly for the coordinates  $q_A, q_B, q_C, q_D$ , referring to the bond lengths  $r_A, r_B, r_C, r_D$  in Fig. 7.1) the 1D C-C potentials ( $\hat{V}_C^{1D}$ ) are calculated and the corresponding vibrational eigenfunctions and eigenvalues are evaluated (Sec. 1.1.3) with the kinetic Hamiltonian operator  $\hat{T}_C^{1D}$  and the mass  $m_C$ :

$$\hat{T}_C^{1D} = -\frac{1}{m_C} \frac{\partial}{\partial r_i^2}. \quad (7.1)$$

Additionally, for pairs of local modes ( $q_A q_B$ ,  $q_B q_C$ ,  $q_C q_D$ ,  $q_A q_C$ ,  $q_B q_D$ ,  $q_C q_E$ ) the 2D potentials  $\hat{V}_{C_i C_j}^{2D}$  are set up. For neighboring oscillators ( $q_A q_B$ ,  $q_B q_C$ ,  $q_C q_D$ ), the kinetic coupling has to be accounted for in the kinetic Hamiltonian  $\hat{T}_{C_i C_j}^{2D}$ :

$$\hat{T}_{C_i C_j}^{2D} = -\frac{1}{2} \left( \frac{2}{m_C} \frac{\partial}{\partial r_i^2} + \frac{2}{m_C} \frac{\partial}{\partial r_j^2} - \frac{2}{m_C} \frac{\partial}{\partial r_i} \frac{\partial}{\partial r_j} \right). \quad (7.2)$$

In contrast, for two non-neighboring oscillators (indicated by the label  $C_i X C_j$ ), the Hamiltonian consists of the 2D potential part  $\hat{V}_{C_i X C_j}^{2D}$  and the kinetic Hamiltonian  $\hat{T}_{C_i X C_j}^{2D}$ , which is assumed to be cartesian, i.e. uncoupled:

$$\hat{T}_{C_i X C_j}^{2D} = -\frac{1}{2} \left( \frac{2}{m_C} \frac{\partial}{\partial r_i^2} + \frac{2}{m_C} \frac{\partial}{\partial r_j^2} \right). \quad (7.3)$$

In this case, the only coupling of the oscillators is due to an intermode anharmonicity of the potential energy surfaces ( $\hat{V}_{C_i C_j}^{2D}$  and  $\hat{V}_{C_i X C_j}^{2D}$ ).

The total wave function  $\Psi$ , representing the carbon stretching mode part of the octatetraene molecule, is expanded in the basis of the 1D local mode functions  $\phi_n$ . The number of local wave functions with the vibrational coordinates  $q_n$  is  $n = 7$ . The product function  $\Psi_m$  takes the form:

$$\Psi_m = \Pi_n \phi_n(q_n) = \phi_1 \phi_2 \phi_3 \phi_4 \phi_5 \phi_6 \phi_7. \quad (7.4)$$

The Hamiltonian matrix  $\mathbf{H}$  and the corresponding matrix elements are calculated as follows. The diagonal elements are equal to the sum of the eigenvalues of the corresponding local mode states, which will be shown below. For the  $m$ -th product state (e.g. the total ground state  $\Psi_0 \equiv 0000000$  is assumed as the state  $m = 0$  and the state with one quantum of excitation in the  $q_A$  local mode  $\Psi_1 \equiv 1000000$  corresponds to  $m = 1$ ), the matrix element is calculated according to:

$$H_{mm} = \langle \Psi_m | \sum_n \hat{H}_n^{1D}(q_n) | \Psi_m \rangle \quad (7.5)$$

$$= \langle \Pi_n^{(m)} \phi_n^{(m)}(q_n) | \sum_n \hat{H}_n^{1D}(q_n) | \Pi_n^{(m)} \phi_n^{(m)}(q_n) \rangle \quad (7.6)$$

$$= \sum_n \langle \phi_n^{(m)}(q_n) | \hat{H}_n^{1D}(q_n) | \phi_n^{(m)}(q_n) \rangle. \quad (7.7)$$

$$H_{00} = 2 \cdot \epsilon_A^0 + 2 \cdot \epsilon_B^0 + 2 \cdot \epsilon_C^0 + \epsilon_D^0 \quad (7.8)$$

$$H_{11} = \epsilon_A^1 + \epsilon_A^0 + 2 \cdot \epsilon_B^0 + 2 \cdot \epsilon_C^0 + \epsilon_D^0 \quad (7.9)$$

Inserting the product function Eq. 7.4 into Eq. 7.5 leads to Eq. 7.6. This equation can be further simplified, yielding Eq. 7.7, as the 1D Hamiltonians  $\hat{H}_n^{1D}(q_n)$  depend only on one local coordinate  $q_n$ . Two examples for diagonal matrix elements are given in Eqs. 7.8 and 7.9. Here,  $\epsilon_n^x$  are the eigenenergies of the local modes  $q_n$ , and  $x$  denotes the degree of excitation of these modes. The kinetic coupling of next-neighbor oscillators as well as the intermode anharmonicity of the 2D potential energy surfaces contribute to the off-diagonal elements. The highest dimensionality of couplings taken into account here is 2D. Equivalently, one could also calculate the corresponding 3D or multi-dimensional potential energy surfaces and take the higher dimensional potential couplings into account. However, from test calculations on the smaller butadiyne system, it was found that the importance of these terms are lower and they can be neglected for the octatetraene model system. The off-diagonal elements  $H_{lm}$  ( $l \neq m$ ) of the Hamiltonian matrix  $\mathbf{H}$  are calculated as:

$$H_{lm} = \langle \Psi_l | \sum_k \sum_j \hat{H}_{kj}^{2D}(q_k q_j) | \Psi_m \rangle \quad (7.10)$$

$$= \langle \Pi_n^{(l)} \phi_n^{(l)}(q_n) | \sum_k \sum_j \hat{H}_{kj}^{2D}(q_k q_j) | \Pi_n^{(m)} \phi_n^{(m)}(q_n) \rangle \quad (7.11)$$

$$= \langle \Pi_n^{(l)} \phi_n^{(l)}(q_n) | \sum_k \sum_j (\hat{T}_{kj}^{2D}(q_k q_j) + \hat{V}_{kj}^{2D}(q_k q_j)) | \Pi_n^{(m)} \phi_n^{(m)}(q_n) \rangle. \quad (7.12)$$

The indexes  $k$  and  $j$  refer to all 2D operators, taken into account. In this study they denote the following pairs of local modes:  $q_A q_B$ ,  $q_B q_C$ ,  $q_C q_D$ ,  $q_A q_C$ ,  $q_B q_D$ ,  $q_C q_E$  and the corresponding mirrored parts (e.g.  $q'_A q'_B$  referring to the bond lengths  $r'_A$  and  $q'_B$  in Fig. 7.1). Eq. 7.12 can be further simplified, since the 2D Hamiltonians  $\hat{T}_{kj}^{2D}(q_k q_j)$  and  $\hat{V}_{kj}^{2D}(q_k q_j)$  depend on two coordinates and they only act on the local mode wave functions, referring to these local coordinates  $(q_k q_j)$ , e.g.:

$$H_{01} = \langle 0000000 | \sum_k \sum_j \hat{H}_{kj}^{2D}(q_k q_j) | 1000000 \rangle \quad (7.13)$$

$$= \langle 0000000 | \hat{H}_{AB}^{2D}(q_A q_B) + \hat{H}_{BC}^{2D}(q_B q_C) + \hat{H}_{AC}^{2D}(q_A q_C) + \dots | 1000000 \rangle \quad (7.14)$$

$$= \langle 00 | \hat{H}_{AB}^{2D}(q_A q_B) | 10 \rangle + \langle 00 | \hat{H}_{BC}^{2D}(q_B q_C) | 00 \rangle + \langle 00 | \hat{H}_{AC}^{2D}(q_A q_C) | 10 \rangle + \dots \quad (7.15)$$

Although exclusively 2D couplings are accounted for in this setup of the Hamiltonian matrix  $\mathbf{H}$ , the vibrational normal modes can be well approached,

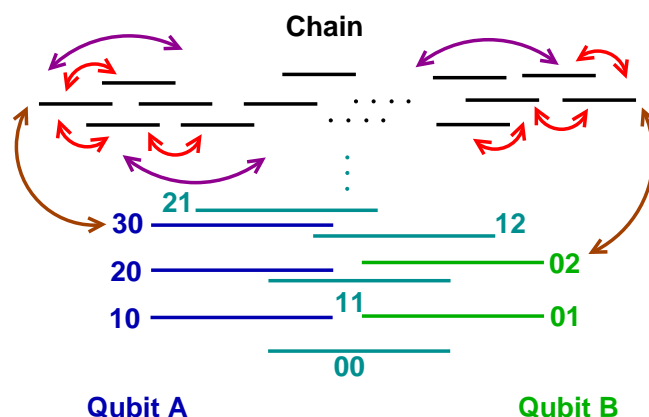


**Figure 7.2:** Model system for two qubits connected by local mode states of a molecular chain (black). As indicated by the green and blue qubit levels, the fundamental frequencies of the qubit modes differ in this setup. The red and magenta arrows indicate the kinetic and potential couplings between the local mode chain states, and additionally a coupling between a qubit overtone state and one chain state at each site is assumed (brown arrows).

since delocalized states as e.g. 1011101 are taken into account. The maximum number of states used in these calculations is on the order of 300.

The octatetraene model, as described above, is extended by vibrational qubit systems, which are assumed to be directly connected to the octatetraene chain. Similar molecular systems, including *sp*-hybridized carbon chains, have been synthesized in the group of J. Gladysz [181, 182]. In these structures, platinum complexes related to the transition metal carbonyl structures, investigated in the previous chapters as qubit systems, are directly linked to both ends of the molecular carbon wire. For the calculations, the product wave function (Eq. 7.4) is expanded by qubit normal mode states, and the system Hamiltonian is extended by the respective matrix elements. The qubit systems are supposed to be connected to the chain ends, instead of the hydrogen atoms in octatetraene (Fig. 7.1). A model setup of this system, composed of a linear carbon chain, described in the local mode basis and two coupled qubit normal modes, is sketched in Fig. 7.2.

For the optimization of a state transfer from one qubit site to the other one across the chain molecule, two different qubit systems linked to the molecular

bridge, were constructed according to Fig. 7.3 a) and b). The qubit mode Q(A) [left side of Fig. 7.2 and Fig. 7.3 a)] is assumed to have a fundamental transition frequency of  $\omega_{Q(A)} = 1400 \text{ cm}^{-1}$  and an anharmonicity of  $\Delta_{Q(A)} = 43 \text{ cm}^{-1}$ , whereas the parameters for the qubit mode Q(B) are  $\omega_{Q(B)} = 2200 \text{ cm}^{-1}$  and  $\Delta_{Q(B)} = 30 \text{ cm}^{-1}$ . The dipole moment of the Q(A) mode is set to  $0.18 \text{ au} = 0.45 \text{ Debye}$  and to  $0.13 \text{ au} = 0.33 \text{ Debye}$  for the Q(B) mode. They are assumed to scale harmonically, i.e. with the square root of the vibrational quantum number.

Additionally, a coupling is introduced between the overtone state  $v = 3$  of the qubit mode Q(A) and a chain state, where the vibrational excitation is located at the Q(A) site of the chain in the local coordinate  $q_A$  [ $\Psi \equiv 2000000$ , Fig. 7.3 b)]. The size of the coupling element is selected to be  $0.0008 \text{ au}$ . Analogously, the second overtone state ( $v = 2$ ) of the Q(B) qubit mode is coupled to the chain state  $\Psi \equiv 0000002$ .

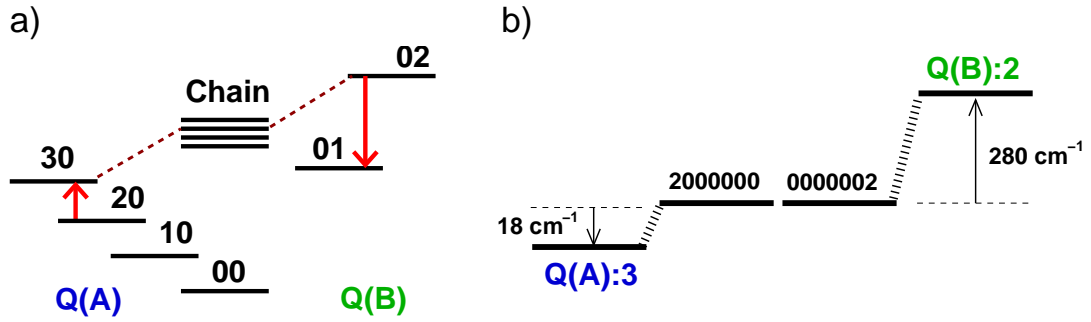


**Figure 7.3:** a) Vibrational state-to-state transfer, which has to be driven from the second excited state of the qubit mode Q(A) to the first excited state of the qubit mode Q(B) by an optimized ultrashort laser field. The overtone and combination states are not shown, for reasons of simplicity, but they are taken into account in the calculations. b) Couplings between the qubit mode and local chain states and energetics of the corresponding levels.

## 7.2 State transfer and quantum channels

In this study, the optimization aim is a vibrational state-to-state transfer from the state  $v_{Q(A)} = 2$  to  $v_{Q(B)} = 1$  as indicated by the red arrows in Fig. 7.3 a).

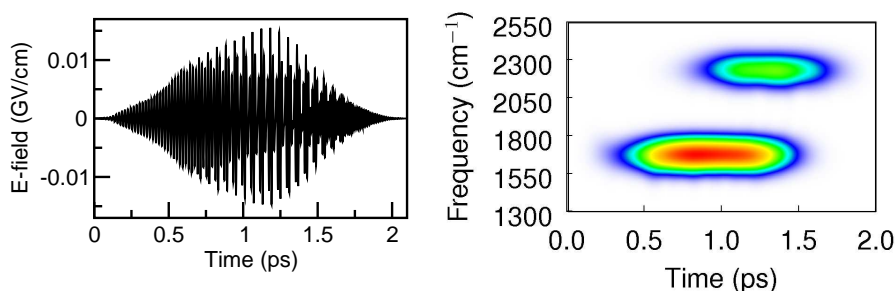


**Figure 7.4:** a) Optimized laser field, driving the state-to-state transfer from  $v = 2$  on the Q(A) qubit mode to  $v = 1$  on the Q(B) qubit mode across the chain states. b) Corresponding FROG representation of the laser pulse.

The initial and target states of interest will be denoted as 20 and 01, only referring to the vibrational degrees of excitation in the qubit modes  $q_{Q(A)}q_{Q(B)}$ , neglecting the chain states. A laser pulse driving the vibrational population transfer  $20 \rightarrow 01$  is optimized with OCT (Eq. 1.60) and an efficiency of 99.2% is reached for a short pulse duration of  $\sim 2.1$  ps. The corresponding laser field is depicted in Fig. 7.4 a), and the FROG representation is shown in Fig. 7.4 b). The FROG diagram reveals a simple pulse structure with two subpulses delayed in frequency and time. It can be traced that the center frequency of the subpulses does not match the transition frequencies  $v_2 \rightarrow v_3$  of  $1314 \text{ cm}^{-1}$  for the qubit mode Q(A) and  $v_2 \rightarrow v_1$  of  $2170 \text{ cm}^{-1}$  for the qubit mode Q(B), as indicated by the red arrows in Fig. 7.3 a).

The mechanism is calculated to understand the vibrational energy transfer process. The evolution of the population in the qubit mode states is shown in Fig. 7.5 a). Initially, the complete population is in the state 20 (blue) and the chain local modes are in the ground state. After 0.5 ps the amount of population in the state 20 starts to decrease and is transferred into the target state 01 (dark-green), but also intermediately to a small extent to the state 02 (light-green), which couples directly to the chain at the qubit site Q(B). The mechanism of the local mode chain states is shown in Fig. 7.5 b). At least 15 local mode states significantly participate in the transfer process and are intermediately populated.

The transition pathway of the population transfer from the initial qubit state

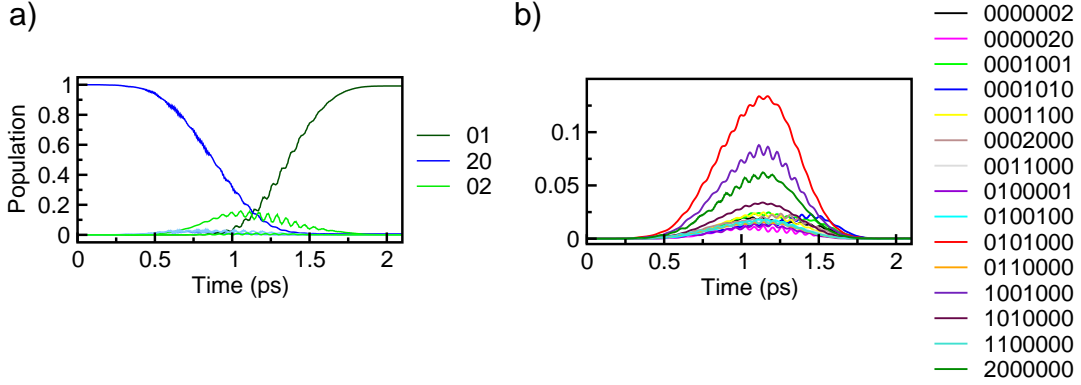


**Figure 7.5:** Mechanism induced by the laser field depicted in Fig. 7.4 a). a) The population in the qubit mode states are depicted, where the vibrational quantum numbers of the local chain states are 0. The blue line refers to the initial state 20 and the dark-green line to the target state 01 of the transfer process. In panel b), the intermediate population of the local chain states is shown. Here, only the vibrational quantum number of the local chain states are given.

20 into the chain states and out of them into the target state 01 has to be clarified. The Hamiltonian, set up in the local mode representation, is diagonalized, and the normal modes of the coupled qubit-chain system are obtained. Certain local mode chain states mix with the qubits mode states 30 and 02, which are directly coupled to the chain, and they are included in the normal modes of the system. The basis of the dipole moment matrix  $\boldsymbol{\mu}$ , referring to qubit mode transitions, is changed to the normal mode basis. This is performed with a transformation matrix  $\mathbf{Y}$  (Eq. 7.16) corresponding to the matrix of the normal mode eigenvectors, which were obtained from the diagonalization of the local mode Hamiltonian.

$$\boldsymbol{\mu}^{\text{normal}} = \mathbf{Y} \boldsymbol{\mu}^{\text{local}} \mathbf{Y}^\dagger. \quad (7.16)$$

As a result, different transition pathways connecting the initial and target state of the qubit modes with the normal modes can be detected. These pathways can be associated with different transition dipole strengths and are illustrated in Fig. 7.6. The blue lines refer to the transitions from the initial state 20

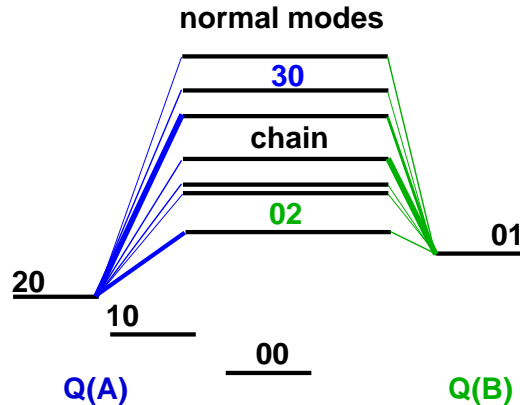


**Figure 7.6:** From the change of the local mode to the normal mode basis, different transition pathways from the initial and target states into the normal mode states can be found. They are indicated by the blue lines for the initial state and by the green lines for the target state. The varying width of the lines indicates that the transition dipole strengths differ.

into the normal mode states and the green lines back into the target state 01. Every blue transition line is related to a green transition path. The differing dipole strengths are indicated by the width of the transition lines. In general the dipole moment matrix elements are larger when the contribution of the coupled local mode states 2000000 and 0000002 to the respective normal mode vectors is higher.

The transition pathways, shown in Fig. 7.6, allow for the identification of the optically accessible normal mode states  $n$  (i.e. the transition matrix elements into these states is  $\mu \neq 0$ ). The possible transitions from the initial (20, blue) and target (01, green) states into these normal mode states  $n$  are depicted in Fig. 7.7 a). They are plotted versus the transition frequencies  $20 \rightarrow n$  (blue) and  $n \rightarrow 01$  (green). Fig. 7.7 b) shows an equivalent graph, but here the size of the corresponding dipole matrix elements for the transitions are indicated by the height of the vertical lines. Each blue line ( $20 \rightarrow n$ ) refers to a corresponding green line ( $n \rightarrow 01$ ), where in both cases the same normal mode state  $n$  is used for the transfer. This can be visualized, by plotting the transition dipole strengths against the number of the respective normal modes states  $n$ , as shown in Fig. 7.7 c).

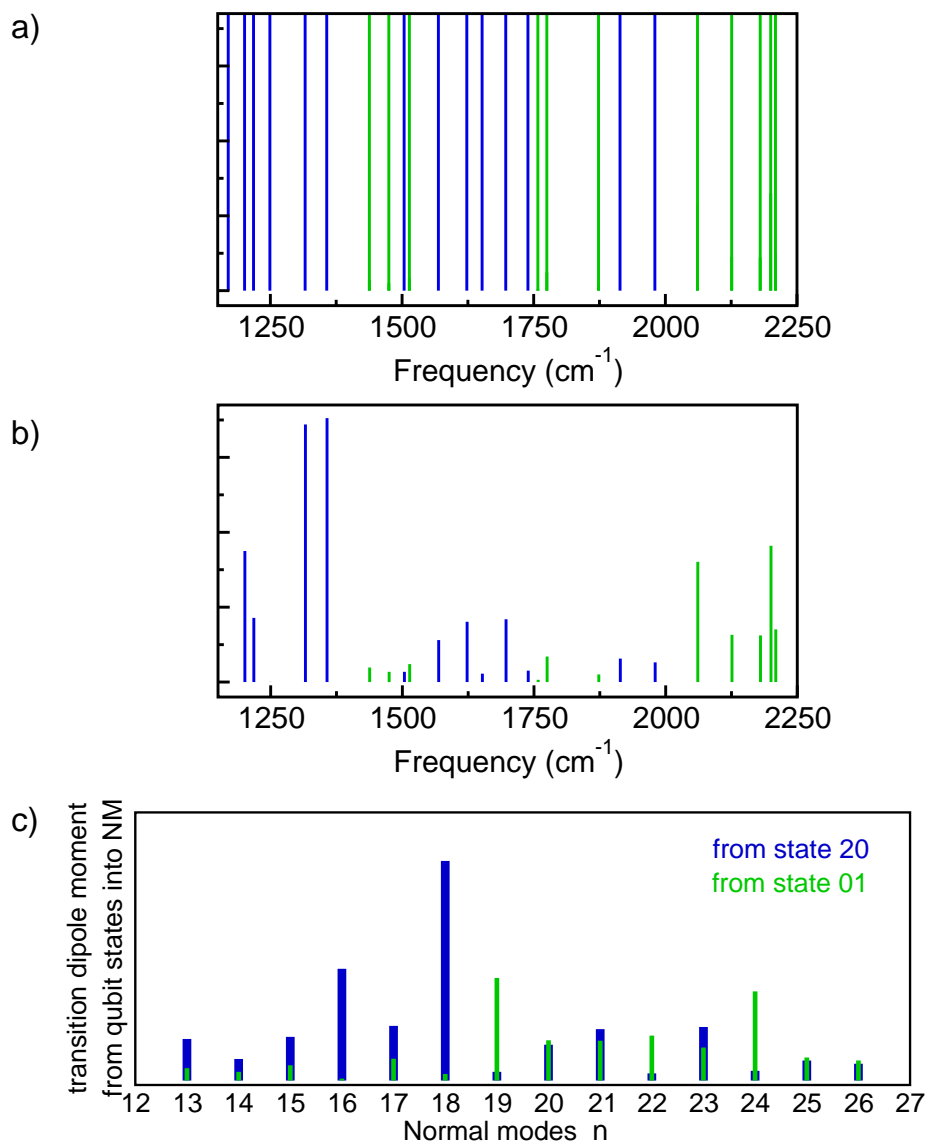


**Figure 7.7:** a) Transition pathways from the initial (20, blue) and target (01, green) states into the normal mode states, plotted as a function of the transition frequency. b) Transition pathways scaled by the size of the respective dipole matrix elements. c) Pathways from both qubit sites, plotted against the normal modes  $n$ .

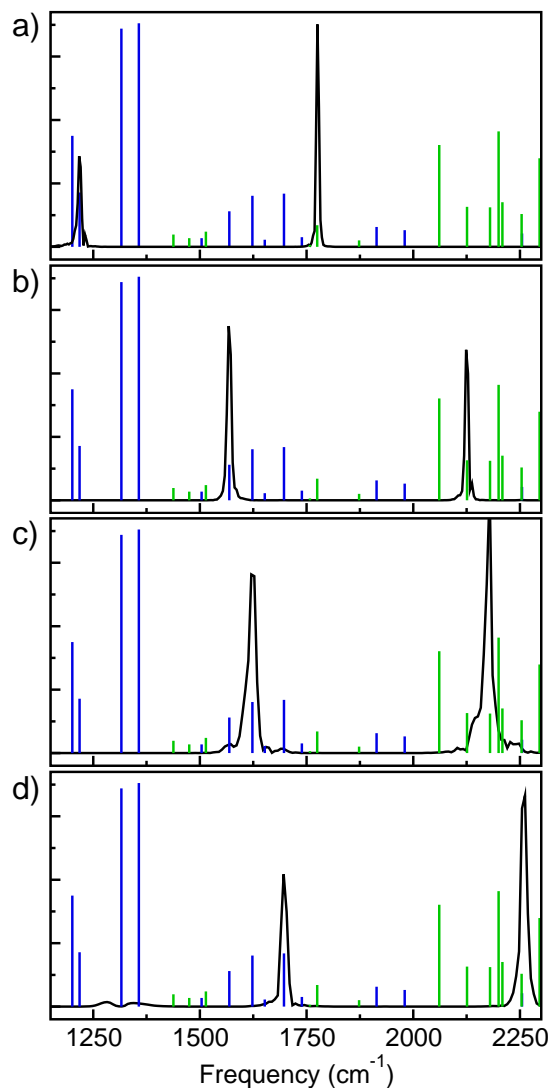


**Figure 7.8:** Transition pathways with spectra of the laser pulses driving the state transfer across the chain molecule through different quantum channels. a)  $n = 17$ , b)  $n = 20$ , c)  $n = 21$  and d)  $n = 23$  [Fig. 7.7 c)].

By means of these plots, the state transfer process induced by the optimized laser pulse [Fig. 7.4 a)] across the molecular chain can be understood. The pulse couples the qubit mode  $Q(A)$  to one or more optically addressable normal mode states  $n$  with the first subpulse and transfers the population from the

state 20 into the local chain states, which form the respective normal modes. The second subpulse draws the population out into the target state 01. The carrier frequencies of the two subpulses [ $1677\text{ cm}^{-1}$  and  $2233\text{ cm}^{-1}$  traced from the FROG representation of the optimized laser field in Fig. 7.4 b)] with respect to the transition pathways [Fig. 7.7b) and c)] reveal that predominantly two normal modes ( $n = 22$  and  $n = 23$ ) are used as transfer channels. As can be deduced from Fig. 7.7 c) several different quantum channels are available for the vibrational population transfer process.

Now a question arises on whether and how the other channels can be used, and if the vibrational energy transfer can be optimized through a single normal mode. For the OCT calculations of the state transfer processes through different normal modes, the initial guess laser fields have to be chosen properly, i.e. a good starting laser field should provide the two frequency components matching the transition frequencies. A desired transfer channel can be selected [Fig. 7.7 c)] and the required frequencies can be extracted from Fig. 7.7 b). A very helpful OCT technique, which assists these kinds of optimizations, is the frequency filtering method presented in Chapter 2 and in [111]. But also the approach based on laser pulses tailored with simple spectral constraints [110] can be used for the calculations. In the population transfer optimizations through distinct quantum channels, only minor parts of the spectrum have to be suppressed, as long as the guess laser field is set into resonance with the normal mode transitions and the penalty factor  $\alpha$  for the optimization is selected high enough. Corresponding optimizations were performed for the normal modes  $n = 17, 20, 21$  and  $23$  [Fig. 7.7 c)] and the results are depicted in Fig. 7.8. The respective laser fields in the time domain are similarly simple as the one depicted in Fig. 7.4 a). The spectra of the calculated laser pulses are mapped onto the available transition pathways and it can be traced that predominantly one normal mode is used as a transfer channel in each case [Fig. 7.8 a)  $n = 17$ , Fig. 7.8 b)  $n = 20$ , Fig. 7.8 c)  $n = 21$  and Fig. 7.8 d)  $n = 23$ ]. The transition frequencies for the excitation processes  $20 \rightarrow n$  and  $n \rightarrow 01$ , with  $n$  referring to the transfer modes (17, 20, 21 and 23), exactly correspond to the carrier frequencies of the single subpulses. The relative size of the dipole matrix elements into and out of the quantum channels account for the differing intensities of the two subpulses. Since the transition dipole moment for the process  $20 \rightarrow n$  is larger in case of  $n = 17, 21, 23$  [blue lines in Fig. 7.7 c)], the spectral intensities of the first subpulses are lower [spectral parts associated with the blue lines in Fig. 7.8 a),

c) and d)]. The situation is reversed for  $n = 20$  [Fig. 7.8 b)]. The presented quantum channels ( $n = 17, 20, 21$  and  $23$ ) turned out to be the most suited ones for the vibrational transfer process and when inspecting the corresponding transition dipole strengths [Fig. 7.7 c)] the reason becomes clear. All of them show similarly sized dipole moment elements for the excitations  $20 \rightarrow n$  and  $n \rightarrow 01$ , i.e. the green and blue lines are equally high. This is particularly the case for the normal mode 20, and accordingly, the spectral intensities of both subpulses in Fig. 7.8 c) are similar.

From these calculations, it is expectable that a transfer of superposition states is possible, where different quantum channels can be used for the process. This result may facilitate quantum information processing with vibrational qubits in future, where after quantum gate operations, the resulting eigenstates or superposition states can be communicated to other qubit units.

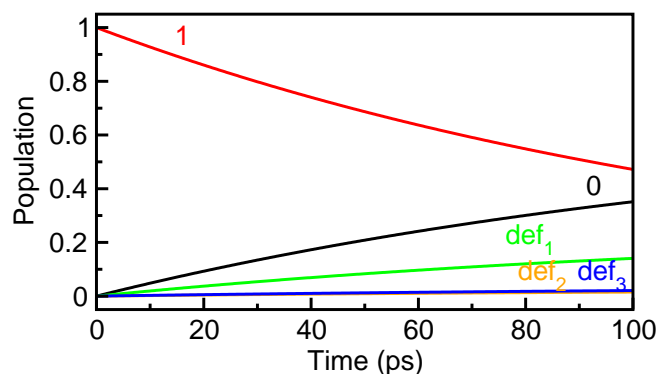


**Figure 7.9:** Mechanism of a dissipative propagation. The vibrational population in the first excited state of the highest energy normal mode of octatetraene (red) relaxes to the ground state (black) and to several resonant deformation mode states (here: green, orange, blue). For short propagation times of  $\sim 2$  ps, as necessary for the vibrational state transfer, the decay of population is negligible.

## 7.3 Investigation of dissipative influence

As already presented for the qubit operations in Chapter 6, dissipative effects are also studied for the vibrational state transfer process across a chain molecule.

For these calculations, a simple IVR model octatetraene is set up in the normal mode representation based on ab-initio data. The complete population is assumed to be in the first vibrational level of the highest energy C-C stretching mode of octatetraene ( $\sim 2300 \text{ cm}^{-1}$ ). As observed in Sec. 7.2, such a state can serve as a transfer channel for the vibrational population. For the dissipation, the vibrational energy relaxation within this normal mode is taken into account as well as a coupling to overtone and combination states of deformation modes, which are in resonance to the initially excited state. To find the resonant states, for each deformation mode an anharmonicity of  $5 \text{ cm}^{-1}$  is assumed and the energy of the overtone and combination states are extrapolated. Overall, 3 resonances were found, with energy differences below  $\Delta E = 5 \text{ cm}^{-1}$  between the deformation states and the initially populated state. Different relaxation rates for the IVR processes into these states and for the relaxation into the ground state are scanned and an example with a relaxation time of  $\sim 200 \text{ ps}$  is shown in Fig. 7.9. The calculations show that the IVR and relaxation time scales need to be on the order of 200 ps to obtain high efficiencies of the vibrational state-to-state transfer processes (with durations of approximately 2 ps, as calculated in Sec. 7.2).

## 7.4 Conclusion

With the idea of a linear, molecular chain connecting individual molecular qubit systems, a first effort towards the scalability of the molecular quantum computing approach with vibrational qubits has been made. In this study, two different qubit systems are assumed to share quantum information with the help of a laser-driven vibrational state-to-state energy transfer. A model system, composed of an octatetraene chain and two qubit modes at each site, was set up, where the bridging molecule was described in the local mode basis. As a first approach, a coupling is assumed between local chain states and an overtone state of each qubit mode. This description may be extended in the future, by incorporating different coupling elements, with the size depending on the energy gap between the coupled states. With OCT as an optimization tool, highly efficient laser fields providing very short pulse durations could be optimized, driving the state transfer processes. From the inspection of the transfer mechanisms, different available transition pathways corresponding to normal mode states could be detected. They can be regarded as quantum channels for the information

transfer, and it was shown that several of these pathways can be used for the transfer. The suitability of the quantum channels depends on the relative size of the transition dipole matrix elements with regard to both qubit sites and the OCT strategy with spectral constraints (Chapter 2, [111]) allows for the control of the transfer through the single channels.



# Summary

The thesis focuses on theoretical control strategies in the context of molecular quantum computing with vibrational qubits. The initially proposed concept [7], based on quantum gates, operating on IR active modes, is extended to Raman active modes. An advantage of this idea is that the stimulated, non-resonant Raman effect can be used for the implementation of quantum logic operations in the experimentally easily accessible 800 nm regime. A universal set of highly efficient quantum gates could be optimized with a newly presented OCT functional. This method allows for the optimization of two laser fields simultaneously, differing in the carrier frequency and driving the non-resonant process. The OCT functional is applied in the Krotov formalism and is extended by frequency filters. The ideas are taken from electrical engineering and allow imposition of strict frequency limitations on the optimized laser fields, while the method operates in the time domain [111]. The frequency filtering OCT scheme is a universal method and facilitates the optimization of ultrashort laser pulses, driving multi-photon, multi-color quantum processes, and it is widely applicable, also in research fields beyond the scope of molecular physics.

The first experimental demonstrations of direct IR shaping techniques on the coherent control of vibrational population transfer in carbonyl complexes [70] open the route towards the first implementation of the molecular quantum computing approach, operating on IR active modes. Inspired by these results, the experimental search strategy with learning loops and genetic algorithms was adapted to theory which allows operating directly in the same search space. Quantum control theory plays a central role here, in predicting and assessing the experimental results. Furthermore, optimizations beyond the boundaries of the experimental setup can be performed and lead to new inputs for the experiments. New search and optimization strategies were investigated, and the theoretical quantum control studies [134] will contribute to better experimental quantum control results.

In quantum control experiments, frequently parametrized phase modulations

are applied because of their advantages to reduce the shaped pulse complexity and to allow for the interpretability of the induced mechanisms. Their application prospects for the implementation of efficient logic operations were studied and by scanning the control landscapes it could be shown that such strict phase forms do not provide enough flexibility for the efficient use in vibrational quantum information processing [134]. On the other hand, results obtained from pixelated mask functions and incident laser pulse properties, applied in the experiment, lead to overly complex solutions and to very long shaped pulse durations.

The reasons for the high complexity could be explained and techniques for the simplification of pulse structures and the decrease of pulse durations were presented. Among those are the usages of longer incident pulse durations, amplitude modulation and limitation of the phase ranges. These approaches are directly transferable to the experiment and should lead to better solutions. As a further step, the advantages of multi-objective genetic algorithms for quantum control tasks were presented for the first time. These algorithms enable the control of several features of the desired outcome simultaneously. In this context, the maximization of the quantum yield, the minimization of pulse durations and energies as well as intermediate overtone excitation were studied. The solutions were gained from the resulting multi-dimensional Pareto fronts [138], and the interplay of the pulse features could be traced.

Also, alternative optimization approaches to genetic algorithms were investigated which can be implemented in the experimental setup in a straightforward way. Learning from the advantages and shortcomings of pixelated and parametrized mask functions in combination with genetic algorithms, the usage of the ant colony optimization algorithm was proposed and demonstrated for the first time [143]. It introduces a tunable correlation between the pixels and provides a high flexibility, since distinct phase and transmittance jumps are tolerated if they are necessary to reach high quantum yields, but they are avoided if possible. As a result strong fluctuations of the mask functions will be suppressed and comparative calculations with genetic algorithms demonstrated the strength of the ant colony method. The algorithm is also directly transferable to the experimental implementation and is supposed to lead to the most promising results in experimental quantum control studies [143].

If a theoretical solution, calculated with optimal control theory, is not realizable due to experimental limitations, it is always possible to find and predict the optimal search strategy, mask functions and shaped laser pulse for an ex-

---

perimentally accessible input pulse with the presented theoretical methods at hand.

The efforts that have been made on quantum control techniques operating in the frequency regime allow for the optimization of simple structured pulses with short pulse durations. This is relevant in the context of quantum computing, where short switching times of the logic operations are favorable. Additionally, dissipative effects reduce the efficiency of the operations in the quantum systems and short, simple structured pulses are assumed to be less sensitive to dissipative effects. To study the influence on vibrational relaxation on the quantum gates, the density matrix formalism was used and the dissipative environment was modeled with the Lindblad approach incorporating experimentally measured vibrational life times in the theoretical calculations. The robustness of quantum gate operations was studied and it could be traced that when intermediate overtone excitations are similarly low, the pulse durations play the dominant role on how strong the dissipation will take place. The pulse complexity is only of minor importance for equally long pulse durations. From optimization studies based on genetic algorithms in the presence of dissipation, it can be learned that also relatively short incident pulses with FWHMs from 50 fs to 100 fs, as frequently employed in the experiments, are suited for the implementation of efficient quantum gates in one-qubit systems, despite their broad spectra. The carrier frequency has to be detuned to higher wave numbers with respect to the fundamental or qubit basis transition. An important point here is the strict limitation of the phase range. For larger molecules, however, the choice of longer FL pulse durations should be favored, since they provide narrower spectra and the shaped pulses will not interact with other vibrational modes of the molecule. The dissipative OCT results conform very well with the GA results. Similarly to the GA solutions they indicate that switching processes towards the end of the laser-molecule interactions are most efficient. It could be shown that  $T_1$  time scales on the order of 200 ps should be sufficient for the experimental demonstration of highly efficient quantum gates in  $\text{MnBr}(\text{CO})_5$ , operating on the  $A_1$  symmetric normal mode in condensed phase. When these experiments will be performed in gas phase, where the dissipative time scales will be significantly longer, multi-qubit gate operations will become realizable. The first experimental realizations are currently performed in the group of M. T. Zanni, and high efficiencies are to be expected. Additionally, the concept of precompiled

quantum computing was demonstrated for vibrational quantum gates and the advantage of a precompiled SWAP gate operation was discussed.

First efforts towards the scalability of the molecular quantum computing approach with vibrational qubits have been made. A quantum network was constructed from two single qubit systems with molecular, linear chains, connecting them. A laser-driven vibrational energy transfer across the bridging chain has been optimized and it can be interpreted as information transfer between the single qubits systems. Different quantum channels for the transfer could be detected, where suited ones can be addressed individually and even the transfer of superposition states between the qubit systems might be possible. Frequency filtering optimal control theory was used for the optimization of the laser fields addressing the single quantum channels.

# Bibliography

- [1] A. H. Zewail, *Femtochemistry: Atomic-Scale Dynamics of the Chemical Bond*, J. Phys. Chem. A **104**, 5660 (2000).
- [2] M. Dantus, M. J. Rosker and A. Zewail, *Real-time femtosecond probing of "transition states" in chemical reactions*, J. Chem. Phys. **87**, 2395 (1987).
- [3] H. Rabitz, R. de Vivie-Riedle, M. Motzkus and K. Kompa, *Whither the Future of Controlling Quantum Phenomena?*, Science **288**, 824 (2000).
- [4] R. S. Judson and H. Rabitz, *Teaching Lasers to Control Molecules*, Phys. Rev. Lett. **68**, 1500 (1992).
- [5] D. J. Tannor, V. Kazakov and V. Orlov, *Time Dependent Quantum Molecular Dynamics*, Plenum, New York (1992).
- [6] W. Zhu, J. Botina and H. Rabitz, *Rapidly convergent iteration methods for quantum optimal control of population*, J. Chem. Phys. **108**, 1953 (1998).
- [7] C. M. Tesch and R. de Vivie-Riedle, *Quantum computation with vibrationally excited molecules*, Phys. Rev. Lett. **89**, 157901 (2002).
- [8] A. Szabo and N. S. Ostlund, *Modern quantum chemistry: introduction to advanced electronic structure theory*, Dover Publications, Inc., Mineola, New York (1996).
- [9] W. Koch and M. C. Holthausen, *A Chemist's Guide to Density Functional Theory*, Wiley-VCH, Weinheim (2001).
- [10] D. J. Tannor, *Introduction to Quantum Mechanics: A Time-Dependent Perspective*, University Science, Sausalito (2007).
- [11] R. Kosloff, *Time-Dependent Quantum-Mechanical Methods for Molecular Dynamics*, J. Phys. Chem. **92**, 2087 (1988).

- [12] C. Leforestier, R. H. Bisseling, C. Cerjan, M. D. Feit, R. Friesner, A. Guldberg, A. Hammerich, G. Jolicard, W. Karrlein, H.-D. Meyer, N. Lipkin, O. Roncero and R. Kosloff, *A Comparison of Different Propagation Schemes for the Time Dependent Schrödinger Equation*, J. Comp. Phys. **94**, 59 (1991).
- [13] K. Sundermann, *Parallele Algorithmen zur Quantendynamik und optimalen Laserpulskontrolle chemischer Reaktionen*, PhD Thesis, Freie Universität Berlin (1998).
- [14] J. Manz, K. Sundermann and R. de Vivie-Riedle, *Quantum Optimal Control Strategies for Photoisomerization via Electronically Excited States*, Chem. Phys. Lett. **290**, 415 (1998).
- [15] K. Blum, *Density Matrix Theory and Applications*, Plenum, New York (1981).
- [16] G. Lindblad, *Entropy, information and quantum measurement*, Comm. Math. Phys. **33**, 305 (1973).
- [17] G. Lindblad, *Expectations and entropy inequalities for finite quantum systems*, Comm. Math. Phys. **39**, 111 (1974).
- [18] G. Lindblad, *On the generators of quantum dynamical semigroups*, Comm. Math. Phys. **48**, 119 (1976).
- [19] L. Pesce, *Dissipative quantum dynamics of elementary chemical processes at metal surfaces*, PhD Thesis, Freie Universität Berlin (1998).
- [20] W. Huisinga, L. Pesce, R. Kosloff and P. Saalfrank, *Faber and Newton polynomial integrators for open-system density matrix propagation*, J. Chem. Phys. **110**, 5538 (1999).
- [21] Y. Huang, D. Kouri and D. Hoffman, *General energy-separable Faber polynomial representation of operator functions: Theory and application in quantum scattering*, J. Chem. Phys. **101**, 10493 (1994).
- [22] M. A. Nielsen and I. L. Chuang, *Quantum Computation and Quantum Information*, Cambridge University Press (2000).

- 
- [23] R. Feynman, *Quantum Mechanical Computers*, Found. Phys. **16**, 507 (1986).
- [24] D. Deutsch, *Quantum-theory, the Church-Turing principle and the universal quantum computer*, Proc. R. Soc. London A **400**, 97 (1985).
- [25] P. W. Shor, *Polynomial-time algorithms for prime factorization and discrete logarithms on a quantum computer*, SIAM J. Comp. **26**, 1484 (1997).
- [26] A. Barenco, C. H. Bennett, R. Cleve, D. P. DiVincenzo, N. Margolus, P. Shor, T. Sleator, J. A. Smolin and H. Weinfurter, *Elementary gates for quantum computation*, Phys. Rev. A **52**, 3457 (1995).
- [27] D. P. diVincenzo, *Quantum Computation*, Science **270**, 255 (1995).
- [28] C. Monroe, D. M. Meekhof, B. E. King, W. M. Itano and D. J. Wineland, *Demonstration of a Fundamental Quantum Logic Gate*, Phys. Rev. Lett. **75**, 4714 (1995).
- [29] J. I. Cirac and P. Zoller, *Quantum Computations with Cold Trapped Ions*, Phys. Rev. Lett. **74**, 4091 (1995).
- [30] D. Kielpinski, C. Monroe and J. Wineland, *Architecture for a large-scale ion-trap quantum computer*, Nature **417**, 709 (2002).
- [31] H. Häffner, W. H. C. F. Roos, J. Benhelm, D. C. al kar, M. Chwalla, T. Körber, U. D. Rapol, M. Riebe, P. O. Schmidt, C. Becher, O. Gühne, W. Dür and R. Blatt, *Scalable multiparticle entanglement of trapped ions*, Nature **438**, 643 (2005).
- [32] D. G. Cory, A. F. Fahmy and T. F. Havel, *Ensemble quantum computing by NMR spectroscopy*, Proc. Natl. Acad. Sci. USA **94**, 1634 (1997).
- [33] J. A. Jones and M. Mosca, *Implementation of a quantum algorithm on a nuclear magnetic resonance quantum computer*, J. Chem. Phys. **109**, 1648 (1998).
- [34] R. Marx, A. F. Fahmy, J. M. Myers, W. Bermel and S. J. Glaser, *Approaching five-bit NMR quantum computing*, Phys. Rev. A **62**, 012310 (2000).

- [35] P. Zanardi and F. Rossi, *Quantum Information in Semiconductors: Noiseless Encoding in a Quantum-Dot-Array*, Phys. Rev. Lett. **81**, 4752 (1998).
- [36] E. Biolatti, R. C. Iotti, P. Zanardi and F. Rossi, *Quantum Information Processing with Semiconductor Macroatoms*, Phys. Rev. Lett. **85**, 5647 (2000).
- [37] I. D'Amico, E. Biolatti, E. Pazy, P. Zanardi and F. Rossi, *All-optical quantum dot implementation for quantum computing*, Physica E **13**, 620 (2002).
- [38] G. Burkard, H.-A. Engel and D. Loss, *Spintronics and Quantum Dots for Quantum Computing and Quantum Communication*, Fortschr. Phys. **48**, 965 (2000).
- [39] V. Cerletti, W. A. Coish, O. Gywat and D. Loss, *Recipes for spin-based quantum computing*, Nanotechnology **16**, R27 (2005).
- [40] Y. Makhlin, G. Schön and A. Shnirman, *Josephson-junction qubits with controlled couplings*, Nature **398**, 305 (1999).
- [41] C. H. van der Wal, F. K. Wilhelm, C. J. P. M. Harmans and J. E. Mooij, *Engineering decoherence in Josephson persistent-current qubits*, Eur. Phys. J. B **31**, 111 (2003).
- [42] F. Helmer, M. Mariani, A. G. Fowler, J. von Delft, E. Solano and F. Marquardt, *Two-dimensional cavity grid for scalable quantum computation with superconducting circuits*, arXiv:0706.3625v1 [cond-mat.mes-hall] (2008).
- [43] A. Rauschenbeutel, G. Nogues, S. Osnaghi, P. Bertet, M. Brune, J. M. Raimond and S. Haroche, *Coherent Operation of a Tunable Quantum Phase Gate in Cavity QED*, Phys. Rev. Lett. **83**, 5166 (1999).
- [44] J. M. Raimond, M. Brune and S. Haroche, *Manipulating quantum entanglement with atoms and photons in a cavity*, Rev. Mod. Phys. **73**, 565 (2001).
- [45] A. Auffeves, P. Maioli, T. Meunier, S. Gleyzes, G. Nogues, M. Brune, J. M. Raimond and S. Haroche, *Entanglement of a Mesoscopic Field with*

- 
- an Atom Induced by Photon Graininess in a Cavity*, Phys. Rev. Lett. **91**, 230405 (2003).
- [46] C. M. Tesch, L. Kurtz and R. de Vivie-Riedle, *Applying optimal control theory for elements of quantum computation in molecular systems*, Chem. Phys. Lett. **343**, 633 (2001).
- [47] C. M. Tesch, *Entwicklung von Molekularem Quantencomputing*, PhD Thesis, Ludwig-Maximilians-Universität München (2002).
- [48] C. M. Tesch and R. de Vivie-Riedle, *Vibrational molecular quantum computing: Basis set independence and theoretical realization of the Deutsch-Jozsa algorithm*, J. Chem. Phys. **121**, 12158 (2004).
- [49] U. Troppmann, C. Gollub and R. de Vivie-Riedle, *The role of phases and their interplay in molecular vibrational quantum computing with multiple qubits.*, New J. Phys. **8**, 100 (2006).
- [50] B. Korff, U. Troppmann, K. Kompa and R. de Vivie-Riedle, *Manganese-pentacarbonyl-bromide as candidate for a molecular qubit system operated in the infrared regime*, J. Chem. Phys. **123**, 244509 (2005).
- [51] C. Gollub, B. Korff, K. Kompa and R. de Vivie-Riedle, *Chirp-driven vibrational distribution in transition metal carbonyl complexes*, Phys. Chem. Chem. Phys. **9**, 369 (2007).
- [52] B. Schneider, C. Gollub, K. Kompa and R. de Vivie-Riedle, *Robustness of quantum gates operating on the high frequency modes of  $\text{MnBr}(\text{CO})_5$* , Chem. Phys. **338**, 291 (2007).
- [53] C. Gollub, U. Troppmann and R. de Vivie-Riedle, *The role of anharmonicity and coupling in quantum computing based on vibrational qubits*, New J. Phys. **8**, 48 (2006).
- [54] D. Babikov, *Accuracy of gates in a quantum computer based on vibrational eigenstates*, J. Chem. Phys. **121**, 7577 (2004).
- [55] S. Suzuki, K. Mishima and K. Yamashita, *Ab initio study of optimal control of ammonia molecular vibrational wavepackets: Towards molecular quantum computing*, Chem. Phys. Lett. **410**, 358 (2005).

- [56] L. Bomble, D. Lauvergnat, F. Remacle and M. Desouter-Lecomte, *Vibrational computing: Simulation of a full adder by optimal control*, J. Chem. Phys. **128**, 064110 (2008).
- [57] K. Mishima, K. Takumo and K. Yamashita, *Quantum computing using molecular electronic and vibrational states*, Chem. Phys. **343**, 61 (2008).
- [58] M. Ndong, L. Bomble, D. Sugny, Y. Justum and M. Desouter-Lecomte, *NOT gate in a cis-trans photoisomerization model*, Phys. Rev. A **76**, 043424 (2007).
- [59] D. Weidinger and M. Gruebele, *Quantum computation with vibrationally excited polyatomic molecules: effects of rotation, level structure, and field gradients*, Mol. Phys. **105**, 1999 (2007).
- [60] K. Shioya, K. Mishima and K. Yamashita, *Quantum computing using molecular vibrational and rotational modes*, Mol. Phys. **105**, 1283 (2007).
- [61] M. Y. Zhao and D. Babikov, *Anharmonic properties of the vibrational quantum computer*, J. Chem. Phys. **126**, 204102 (2007).
- [62] M. Tsubouchi and T. Momose, *Rovibrational wave-packet manipulation using shaped midinfrared femtosecond pulses toward quantum computation: Optimization of pulse shape by a genetic algorithm*, Phys. Rev. A **77**, 052326 (2008).
- [63] M. Ndong, D. Lauvergnat, X. Chapuisat and M. Desouter-Lecomte, *Optimal control simulation of the Deutsch-Jozsa algorithm in a two-dimensional double well coupled to an environment*, J. Chem. Phys. **126**, 244505 (2007).
- [64] D. Sugny, C. Kontz, M. Ndong, Y. Justum, G. Dive and M. Desouter-Lecomte, *Laser control in a bifurcating region*, Phys. Rev. A **74**, 043419 (2006).
- [65] D. Sugny, M. Ndong, D. Lauvergnat, Y. Justum and M. Desouter-Lecomte, *Laser control in open molecular systems: STIRAP and optimal control*, J. Photochem. Photobiol. A **190**, 359 (2007).

- 
- [66] T. W. Cheng and A. Brown, *Quantum computing based on vibrational eigenstates: Pulse area theorem analysis*, J. Chem. Phys. **124**, 034111 (2006).
- [67] R. de Vivie-Riedle and U. Troppmann, *Femtosecond lasers for quantum information technology*, Chem. Rev. **107**, 5082 (2007).
- [68] S.-H. Shim, D. B. Strasfeld, E. C. Fulmer and M. T. Zanni, *Femtosecond pulse shaping directly in the mid-IR using acousto-optic modulation*, Opt. Lett. **31**, 838 (2006).
- [69] S.-H. Shim, D. B. Strasfeld and M. T. Zanni, *Generation and characterization of phase and amplitude shaped femtosecond mid-IR pulses*, Opt. Exp. **14**, 13120 (2006).
- [70] D. B. Strasfeld, S.-H. Shim and M. T. Zanni, *Controlling vibrational excitation with shaped mid-IR pulses*, Phys. Rev. Lett. **99**, 038102 (2007).
- [71] H. S. Tan and W. S. Warren, *Mid infrared pulse shaping by optical parametric amplification and its application to optical free induction decay measurement*, Opt. Exp. **11**, 1021 (2003).
- [72] M. Tsubouchi and T. Momose, *Femtosecond pulse shaping in the mid-infrared generated by difference-frequency mixing: a simulation and experiment*, J. Opt. Soc. Am. B **24**, 1886 (2007).
- [73] W. Demtröder, *Laser Spectroscopy*, Springer, Berlin (2003).
- [74] D. J. Kane and R. Trebino, *Single-shot measurement of the intensity and phase of an arbitrary ultrashort pulse by using frequency-resolved optical gating*, Opt. Lett. **18**, 823 (1993).
- [75] D. J. Kane, G. Rodriguez, A. J. Taylor and T. S. Clement, *Simultaneous measurement of two ultrashort laser pulses from a single spectrogram in a single shot*, J. Opt. Soc. Am. B **14**, 935 (1997).
- [76] M. E. Anderson, A. Monmayrant, S. P. Gorza, P. Wasylczyk and I. A. Walmsley, *SPIDER: A decade of measuring ultrashort pulses*, Laser Phys. Lett. **5**, 259 (2008).

- [77] G. Stibenz and G. Steinmeyer, *Interferometric frequency-resolved optical gating*, Opt. Exp. **13**, 2617 (2005).
- [78] J.-C. Diels and W. Rudolph, *Ultrashort Laser Pulse Phenomena*, Optics and Photonics, Academic Press, Inc., San Diego (1995).
- [79] W. S. Warren, H. Rabitz and M. Dahleh, *Coherent Control of Quantum Dynamics: The Dream Is Alive*, Science **259**, 1581 (1993).
- [80] P. Brumer and M. Shapiro, *Laser Control of Chemical Reactions*, Scientific American **3**, 34 (1995).
- [81] A. Assion, T. Baumert, M. Bergt, T. Brixner, B. Kiefer, V. Seyfried, M. Strehle and G. Gerber, *Control of Chemical Reactions by feedback-optimized Phase-Shaped Femtosecond Laser Pulses*, Science **282**, 919 (1998).
- [82] T. Chem, Y. Vierheilig, P. Waltner, M. Heid, W. Kiefer and A. Materny, *Femtosecond laser-controlled selective excitation of vibrational modes on a multidimensional ground state potential energy surface*, Chem. Phys. Lett. **326**, 375 (2000).
- [83] T. Brixner, N. H. Damrauer, P. Niklaus and G. Gerber, *Photoselective adaptive femtosecond quantum control in the liquid phase*, Nature **414**, 57 (2001).
- [84] R. J. Levis, G. M. Menkir and H. Rabitz, *Selective bond dissociation and rearrangement with optimally tailored, strong-field laser pulses*, Science **292**, 709 (2001).
- [85] D. Zeidler, S. Frey, K.-L. Kompa and M. Motzkus, *Evolutionary algorithms and their application to optimal control studies*, Phys. Rev. A **64**, 023420 (2001).
- [86] D. Zeidler, S. Frey, W. Whlleben, M. Mozkus, F. Busch, T. Chen, W. Kiefer and A. Materny, *Optimal Control of ground-state dynamics in polymers*, J. Chem. Phys. **116**, 5231 (2002).
- [87] P. Nürnbergger, G. Vogt, T. Brixner and G. Gerber, *Femtosecond quantum control of molecular dynamics in the condensed phase*, Phys. Chem. Chem. Phys. **9**, 2470 (2007).

- 
- [88] C. Daniel, J. Full, L. Gonzalez, C. Lupulescu, J. Manz, A. Merli, S. Vajda and L. Wöste, *Deciphering the Reaction Dynamics Underlying Optimal Control Laser Fields*, *Science* **299**, 536 (2003).
- [89] A. M. Weiner, *Femtosecond optical pulse shaping and processing*, *Prog. Quant. Electr.* **19**, 161 (1995).
- [90] A. M. Weiner, D. E. Leaird, J. S. Patel and J. R. W. II, *Programmable shaping of femtosecond optical pulses by use of 128-element liquid crystal phase modulator*, *IEEE Journal of Quantum Electronics* **28**, 908 (1992).
- [91] T. Witte, D. Zeidler, D. Proch, K.-L. Kompa and M. Motzkus, *Programmable amplitude and phase modulated fs laser pulses in the mid-infrared*, *Opt. Lett.* **27**, 131 (2002).
- [92] T. Hornung, M. Motzkus and R. de Vivie-Riedle, *Adapting optimal control theory and using learning loops to provide experimentally feasible shaping mask patterns*, *J. Chem. Phys.* **115**, 3105 (2001).
- [93] T. Witte, *Über molekulare Grundzustandskontrolle durch modulierte Femtosekundenpulse im mittleren Infrarot*, PhD Thesis, Ludwig-Maximilians-Universität München, 2003.
- [94] D. E. Goldberg, *Genetic Algorithms in Search, Optimization, and Machine Learning*, Addison-Wesley, Massachusetts (2005).
- [95] GALIB genetic algorithm package: Matthew Wall, Massachusetts Institute of Technology.
- [96] W. Zhu and H. Rabitz, *A rapid monotonically convergent iteration algorithm for quantum optimal control over the expectation value of a positive definite operator*, *J. Chem. Phys.* **109**, 385 (1998).
- [97] D. Tannor and S. A. Rice, *Control of selectivity of chemical reaction via control of wave packet evolution*, *J. Chem. Phys.* **83**, 5013 (1985).
- [98] J. P. Palao and R. Kosloff, *Quantum Computing by an Optimal Control Algorithm for Unitary Transformations*, *Phys. Rev. Lett.* **89**, 188301 (2002).

- [99] J. P. Palao and R. Kosloff, *Optimal control theory for unitary transformations*, Phys. Rev. A **68**, 062308 (2003).
- [100] K. Sundermann and R. de Vivie-Riedle, *Extensions to quantum control algorithms and applications to special problems in state selective molecular dynamics*, J. Chem. Phys. **110**, 1896 (1999).
- [101] P. Gross, D. Neuhauser and H. Rabitz, *Optimal control of curve crossing systems*, J. Chem. Phys **96**, 2834 (1992).
- [102] S. Shi, A. Woody and H. Rabitz, *Optimal control of selective vibrational excitation in harmonic linear chain molecules*, J. Chem. Phys **88**, 6870 (1988).
- [103] J. Somloi, V. A. Kazakov and D. J. Tannor, *Controlled dissociation of  $I_2$  via optical transitions between  $X$  and  $B$  electronic states*, Chem. Phys **172**, 85 (1993).
- [104] C. P. Koch, J. P. Palao, R. Kosloff and F. Masnou-Seeuws, *Stabilization of ultracold molecules using optimal control theory*, Phys. Rev. A **70**, 013402 (2004).
- [105] V. V. Lozovoy, X. Zhu, T. C. Gunaratne, D. A. Harris, J. C. Shane and M. Dantus, *Control of Molecular Fragmentation Using Shaped Femtosecond Pulses*, J. Phys. Chem. A **112**, 3789 (2008).
- [106] R. Selle, P. Nürnbergger, F. Langhojer, F. Dimler, S. Ferchner, G. Gerber and T. Brixner, *Generation of polarization-shaped ultraviolet femtosecond pulses*, Opt. Lett. **33**, 803 (2008).
- [107] D. Wolpert, M. Schade, F. Langhojer, G. Gerber and T. Brixner, *Quantum control of the photoinduced Wolff rearrangement of diazonaphthoquinone in the condensed phase*, J. Phys. B: At. Mol. Opt. Phys. **41**, 074025 (2008).
- [108] M. J. Frisch, G. W. Trucks, H. B. Schlegel, G. E. Scuseria, M. A. Robb, J. R. Cheeseman, J. A. Montgomery, Jr., T. Vreven, K. N. Kudin, J. C. Burant, J. M. Millam, S. S. Iyengar, J. Tomasi, V. Barone, B. Mennucci, M. Cossi, G. Scalmani, N. Rega, G. A. Petersson, H. Nakatsuji, M. Hada, M. Ehara, K. Toyota, R. Fukuda, J. Hasegawa, M. Ishida, T. Nakajima, Y. Honda, O. Kitao, H. Nakai, M. Klene, X. Li, J. E. Knox, H. P.

- Hratchian, J. B. Cross, C. Adamo, J. Jaramillo, R. Gomperts, R. E. Stratmann, O. Yazyev, A. J. Austin, R. Cammi, C. Pomelli, J. W. Ochterski, P. Y. Ayala, K. Morokuma, G. A. Voth, P. Salvador, J. J. Dannenberg, V. G. Zakrzewski, S. Dapprich, A. D. Daniels, M. C. Strain, O. Farkas, D. K. Malick, A. D. Rabuck, K. Raghavachari, J. B. Foresman, J. V. Ortiz, Q. Cui, A. G. Baboul, S. Clifford, J. Cioslowski, B. B. Stefanov, G. Liu, A. Liashenko, P. Piskorz, I. Komaromi, R. L. Martin, D. J. Fox, T. Keith, M. A. Al-Laham, C. Y. Peng, A. Nanayakkara, M. Challacombe, P. M. W. Gill, B. Johnson, W. Chen, M. W. Wong, C. Gonzalez and J. A. Pople, *Gaussian 03, Revision D.01*, Gaussian, Inc., Pittsburgh PA (2003).
- [109] M. Artamonov, T.-S. Ho and H. Rabitz, *Quantum optimal control of ozone isomerization*, Chem. Phys. **305**, 213 (2004).
- [110] J. Werschnik and E. Gross, *Tailoring laser pulses with spectral and fluence constraints using optimal control theory*, J. Opt. B: Quantum Semiclass. Opt. **7**, S300 (2005).
- [111] C. Gollub, M. Kowalewski and R. de Vivie-Riedle, *Monotonic convergent optimal control theory with strict limitations on the spectrum of optimized laser fields*, Phys. Rev. Lett. **101**, 073002 (2008).
- [112] A. V. Oppenheimer, R. W. Schaffer and J. Buck, *Discrete Time Signal Processing*, Prentice Hall, Upper Saddle River, NJ (1999).
- [113] H. Tal-Ezer and R. Kosloff, *An accurate and efficient scheme for propagating the time dependent Schrödinger equation*, J. Chem. Phys. **81**, 3967 (1984).
- [114] T. Brixner and G. Gerber, *Quantum Control of Gas-Phase and Liquid-Phase Femtochemistry*, ChemPhysChem **4**, 418 (2003).
- [115] R. Levis and H. Rabitz, *Closing the Loop on Bond Selective Chemistry Using Tailored Strong Field Laser Pulses*, J. Phys. Chem. A **106**, 6427 (2002).
- [116] M. Aeschlimann, M. Bauer, D. Bayer, T. Brixner, F. J. G. de Abajo, W. Pfeiffer, M. Rohmer, C. Spindler and F. Steeb, *Adaptive subwavelength control of nano-optical fields*, Nature **446**, 301 (2007).

- [117] J. Gdde, M. Rohleder, T. Meier, S. Koch and U. Hfer, *Time-resolved investigation of coherently controlled electric currents at a metal surface*, Science **318**, 1287 (2007).
- [118] A. Sprl, T. Schulte-Herbrggen, S. J. Glaser, V. Bergholm, M. J. Storcz, J. Ferber and F. K. Wilhelm, *Optimal control of coupled Josephson qubits*, Phys. Rev. A **75**, 012302 (2007).
- [119] U. Dorner, T. Calarco, P. Zoller, A. Browaeys and P. Grangier, *Quantum logic via optimal control in holographic dipole traps*, J. Opt. B: Quantum Semiclass. Opt. **7**, S341 (2005).
- [120] D. J. Tannor and A. Bartana, *On the Interplay of Control Fields and Spontaneous Emission in Laser Cooling*, J. Phys. Chem. A **103**, 10359 (1999).
- [121] G. D. Chiara, T. Calarco, M. Anderlini, S. Montangero, P. J. Lee, B. L. Brown, W. D. Phillips and J. V. Porto, *Optimal control of atom transport for quantum gates in optical lattices*, Phys. Rev. A **77**, 052333 (2008).
- [122] N. Timoney, V. Elman, S. Glaser, C. Weiss, M. Johanning, W. Neuhauser and C. Wunderlich, *Error-resistant single-qubit gates with trapped ions*, Phys. Rev. A **77**, 052334 (2008).
- [123] T. Schulte-Herbrggen, A. Sprl, N. Khaneja and S. Glaser, *Optimal Control for Generating Quantum Gates in Open Dissipative Systems*, quant-ph S. 0609037 (2008).
- [124] S. Schulz, U. Poschinger, K. Singera and F. Schmidt-Kaler, *Optimization of segmented linear Paul traps and transport of stored particles*, Prog. Phys. **54**, 648 (2006).
- [125] N. Belabas, J. P. Likforman, L. Canioni, B. Bousquet and M. Joffre, *Coherent broadband pulse shaping in the mid infrared*, Opt. Lett. **26**, 743 (2001).
- [126] F. Eickemeyer, R. A. Kaindl, M. Woerner, T. Elsaesser and A. M. Weiner, *Controlled shaping of ultrafast electric field transients in the mid-infrared spectral range*, Opt. Lett. **25**, 1472 (2000).

- 
- [127] E. A. Torres, K. L. Kompa, F. Remaille and R. D. Levine, *Ultrafast vibrational spectroscopy and relaxation in polyatomic molecules: Potential for molecular parallel computing*, Chem. Phys. **347**, 531 (2008).
- [128] S. M. Arrivo, T. Dougherty, W. Grubbs and E. Heilweil, *Ultrafast infrared spectroscopy of vibrational CO-stretch up-pumping and relaxation dynamics of  $W(CO)_6$* , Chem. Phys. Lett. **235**, 247 (1995).
- [129] A. Tokmakoff, B. Sauter, A. S. Kwok and M. D. Fayer, *Phonon-induced scattering between vibrations and multiphoton vibrational up-pumping in liquid solution*, Chem. Phys. Lett. **221**, 412 (1994).
- [130] T. Witte, J. Yeston, M. Motzkus, E. Heilweil and K. L. Kompa, *Femtosecond infrared coherent excitation of liquid phase vibrational population distributions ( $v > 5$ )*, Chem. Phys. Lett. **392**, 156 (2004).
- [131] M. Banno, S. Sato, K. Iwata and H. Hamaguchi, *Solvent-dependent intra- and intermolecular vibrational energy transfer of  $W(CO)_6$  probed with sub-picosecond time-resolved infrared spectroscopy*, Chem. Phys. Lett. **412**, 464 (2005).
- [132] J. Herek, W. Wohlleben, R. J. Cogdell, D. Zeidler and M. Motzkus, *Quantum control of energy flow in light harvesting*, Nature **417**, 533 (2002).
- [133] T. Hornung, R. Meier and M. Motzkus, *Optimal control of molecular states in a learning loop with a parameterization in frequency and time domain*, Chem. Phys. Lett. **326**, 445 (2000).
- [134] C. Gollub and R. de Vivie-Riedle, *Theoretical optimization and prediction in the experimental search space for vibrational quantum processes*, Phys. Rev. A **78**, 033424 (2008).
- [135] E. Zitzler and L. Thiele, *Multiobjective Evolutionary Algorithms: A Comparative Case Study and the Strength Pareto Evolutionary Algorithm*, IEEE Trans. Evol. Comput. **3**, 257 (1999).
- [136] K. Deb, A. Pratap, S. Agarwal and T. Meyarivan, *A fast and elitist multi-objective genetic algorithm: NSGA-II*, IEEE Trans. Evol. Comput. **6**, 182 (2002).

- [137] L. Bonacina, J. Extermann, A. Rondi, V. Boutou and J.-P. Wolf, *Multi-Objective Genetic Approach for Optimal Control of Photo-induced Processes*, Phys. Rev. A **76**, 023408 (2007).
- [138] C. Gollub and R. de Vivie-Riedle, *Multi-objective genetic algorithm optimization of 2D- and 3D-Pareto fronts for vibrational quantum processes*, New J. Phys., accepted (2008).
- [139] M. Dorigo, V. Maniezzo and A. Coloni, *The Ant System: Optimization by a colony of cooperating agents*, IEEE Trans. Syst. Man Cybern. B **26**, 29 (1996).
- [140] E. Bonabeau, M. Dorigo and G. Theraulaz, *Inspiration for optimization from social insect behavior*, Nature **406**, 39 (2000).
- [141] A. Shmygelska and H. H. Hoos, *An ant colony optimisation algorithm for the 2D and 3D hydrophobic polar protein folding problem*, Bioinf. **6**, 30 (2005).
- [142] F. Daeyaert, M. de Jonge, L. Koymans and M. Vinkers, *An ant algorithm for the conformational analysis of flexible molecules*, J. Comput. Chem. **28**, 890 (2007).
- [143] C. Gollub and R. de Vivie-Riedle, *A modified Ant Colony Optimization Algorithm as an Alternative to Genetic Algorithms*, submitted.
- [144] B. Hellsing and H. Metiu, *An efficient method for solving the quantum Liouville equation: Applications to electronic absorption spectroscopy*, Chem. Phys. Lett. **127**, 45 (1986).
- [145] I. Burghardt, *Dynamics of Predissociation in the Condensed Phase: Markovian Master Equation*, J. Phys. Chem. **102**, 4192 (1998).
- [146] W. K. Lai, K.-A. Suominen, B. M. Garraway and S. Stenholm, *Dissipation effects on wave packets in level crossings: A comparison between two numerical approaches*, Phys. Rev. A **47**, 4779 (1993).
- [147] S. Beyvers, Y. Ohtsuki and P. Saalfrank, *Optimal control in a dissipative system: Vibrational excitation of CO/Cu(100) by IR pulses*, J. Chem. Phys. **124**, 234706 (2006).

- 
- [148] J. C. Tremblay, S. Beyvers and P. S. P, *Selective excitation of coupled CO vibrations on a dissipative Cu(100) surface by shaped infrared laser pulses*, J. Chem. Phys. **128**, 194709 (2008).
- [149] S. Beyvers and P. Saalfrank, *A hybrid local/global optimal control algorithm for dissipative systems with time-dependent targets*, J. Chem. Phys. **128**, 074104 (2008).
- [150] D. B. Strasfeld and M. T. Zanni, private communication.
- [151] J. Vala, Z. Amitay, B. Zhang, S. R. Leone and R. Kosloff, *Experimental implementation of the Deutsch-Jozsa algorithm for three-qubit functions using pure coherent molecular superpositions*, Phys. Rev. A **66**, 062316 (2002).
- [152] R. Zadoyan, D. Kohen, D. A. Lidar and V. A. Apkarian, *The manipulation of massive ro-vibronic superpositions using time-frequency-resolved coherent anti-Stokes Raman scattering (TFRCARS): from quantum control to quantum computing*, Chem. Phys. **266**, 323 (2001).
- [153] Z. Bihary, D. R. Glenn, D. A. Lidar and V. A. Apkarian, *An implementation of the Deutsch-Jozsa Algorithm on Molecular Vibronic Coherences Through Four-Wave Mixing: A Theoretical Study*, Chem. Phys. Lett. **360**, 459 (2002).
- [154] K. Moritsugu, O. Miyashita and A. Kidera, *Vibrational Energy Transfer in a Protein Molecule*, Phys. Rev. Lett. **85**, 3970 (2000).
- [155] J. Antony, B. Schmidt and C. Schutte, *Nonadiabatic effects on peptide vibrational dynamics induced by conformational changes*, J. Chem. Phys. **122**, 014309 (2005).
- [156] A. Pecchia, M. Gheorghe, A. D. Carlo and P. Lugli, *Role of thermal vibrations in molecular wire conduction*, Phys. Rev. B. **68**, 235321 (2003).
- [157] M. Gheorghe, R. Gutiérrez, N. Ranjan, A. Pecchia, A. D. Carlo and G. Cuniberti, *Vibrational effects in the linear conductance of carbon nanotubes*, Europhys. Lett. **71**, 438 (2005).

- [158] A. Nitzan and M. A. Ratner, *Electron Transport in Molecular Wire Junctions*, Science **300**, 1384 (2003).
- [159] M. Tommasini, G. Zerbi, V. Chernyak and S. Mukamel, *Excited-State Molecular Dynamics Simulations of Conjugated Oligomers Using the Electronic Density Matrix*, J. Phys. Chem. A **105**, 7057 (2001).
- [160] E. Atas, Z. Peng and V. D. Kleiman, *Energy Transfer in Unsymmetrical Phenylene Ethynylene Dendrimers*, J. Phys. Chem. B **109**, 13553 (2005).
- [161] D. Schwarzer, P. Kutne, C. Schröder and J. Troe, *Intramolecular vibrational energy redistribution in bridged azulene-anthracene compounds: Ballistic energy transport through molecular chains*, J. Chem. Phys. **121**, 1754 (2004).
- [162] Z. Wang, A. Pakoulev and D. D. Klott, *Watching Vibrational Energy Transfer in Liquids with Atomic Spatial Resolution*, Science **296**, 2201 (2002).
- [163] D. Schwarzer, C. Hanisch, P. Kutne and J. Troe, *Vibrational Energy Transfer in Highly Excited Bridged Azulene-Aryl Compounds: Direct Observation of Energy Flow through Aliphatic Chains and into the Solvent*, J. Phys. Chem. A **106**, 8019 (2002).
- [164] D. Antoniou and S. D. Schwartz, *Vibrational energy transfer in linear hydrocarbon chains: New quantum results*, J. Chem. Phys. **103**, 7277 (1995).
- [165] A. Zwielly, A. Portnov, C. Levi, S. Rosenwaks and I. Bar, *Rovibrational spectroscopy and intramolecular dynamics of 1,2-trans-d<sub>2</sub>-ethene in the first C-H stretch overtone region*, J. Chem. Phys. **128**, 114305 (2008).
- [166] T. Kim and P. M. Felker, *Vibrational Spectroscopy and Dynamics in the CH-Stretch Region of Fluorene by IVR-Assisted, Ionization-Gain Stimulated Raman Spectroscopy*, J. Phys. Chem. A **111**, 12466 (2007).
- [167] Y. Yamada, Y. Katsumoto and T. Ebata, *Picosecond IR-UV pump probe spectroscopic study on the vibrational energy flow in isolated molecules and clusters*, Phys. Chem. Chem. Phys. **9**, 1170 (2007).

- 
- [168] Y. Pang, J. C. Deak, W. T. Huang, A. Lagutchev, A. Pakoulev, J. E. Patterson, T. D. Sechler, Z. H. Wang and D. D. Klott, *Vibrational energy in molecules probed with high time and space resolution*, Int. Rev. Phys. Chem. **26**, 223 (2007).
- [169] V. May and O. Kühn, *Charge and Energy Transfer Dynamics in Molecular Systems*, Wiley VCH, Berlin (2000).
- [170] P. Hamm, M. Lim, W. F. DeGrado and R. M. Hochstrasser, *The two-dimensional IR nonlinear spectroscopy of a cyclic penta-peptide in relation to its three-dimensional structure*, Proc. Natl. Acad. Sci. USA **96**, 2036 (1999).
- [171] R. M. Hochstrasser, *Two-dimensional IR-spectroscopy: polarization anisotropy effects*, Chem. Phys. **266**, 273 (2001).
- [172] M. T. Zanni and R. M. Hochstrasser, *Two-dimensional infrared spectroscopy: a promising new method for the time resolution of structures*, Curr. Opin. Struct. Biol. **11**, 516 (2001).
- [173] S. Gnanakaran and R. M. Hochstrasser, *Conformational Preferences and Vibrational Frequency Distributions of Short Peptides in Relation to Multidimensional Infrared Spectroscopy*, J. Am. Chem. Soc. **123**, 12886 (2001).
- [174] Y. S. Kim and R. M. Hochstrasser, *The 2D IR responses of amide and carbonyl modes in water cannot be described by Gaussian frequency fluctuations*, J. Phys. Chem. B **111**, 9697 (2007).
- [175] P. Hamm, L. H. Lim and R. M. Hochstrasser, *Structure of the amide I band of peptides measured by femtosecond nonlinear-infrared spectroscopy*, J. Phys. Chem. B **102**, 6123 (1998).
- [176] T. Brixner, F. J. García de Abajo, J. Schneider and W. Pfeiffer, *Nanosopic Ultrafast Space-Time-Resolved Spectroscopy*, Phys. Rev. Lett. **95**, 093901 (2005).
- [177] S. Bose, *Quantum Communication through an Unmodulated Spin Chain*, Phys. Rev. Lett. **91**, 207901 (2003).

- [178] M. Christandl, N. Datta, A. Ekert and A. J. Landahl, *Perfect State Transfer in Quantum Spin Networks*, Phys. Rev. Lett. **92**, 187902 (2004).
- [179] K. Audenaert, J. Eisert, M. B. Plenio and R. F. Werner, *Entanglement properties of the harmonic chain*, Phys. Rev. A **66**, 042327 (2002).
- [180] U. Troppmann, *Studien zur Realisierbarkeit von Molekularem Quantencomputing*, PhD Thesis, Ludwig-Maximilians-Universität München (2006).
- [181] J. Stahl, J. C. Bohling, E. B. Bauer, T. B. Peters, W. Mohr, J. M. Martín-Alvarez, F. Hampel and J. A. Gladysz, *sp Carbon Chains Surrounded by sp<sup>3</sup> Carbon Double Helices: A Class of Molecules that are Accessible by Self-Assembly and Models for insulated Molecular-Scale Devices*, Angew. Chem. Int. Ed. **41**, 1871 (2002).
- [182] L. de Quadras, E. B. Bauer, J. Stahl, F. Zhuravlev, F. Hampel and J. A. Gladysz, *sp Carbon Chains Surrounded by sp<sup>3</sup> Carbon Double Helices: wire-like Pt(C≡C)<sub>n</sub>Pt moieties that are spanned by two α,ω-diphosphines that bear heteroatoms or alkyl substituents*, New J. Chem. **31**, 1594 (2007).

# Curriculum Vitae

Name	Caroline Gollub
Geburtsdatum, Geburtsort	17.04.1981, Mannheim
Familienstand	ledig
Nationalität	deutsch

## Schulische Ausbildung

1991 – 1992	Lessing-Gymnasium, Mannheim
1992 – 1997	Gymnasium, Schrobenhausen
1997 / 1998	Sylvan Hills High School, Little Rock, Arkansas, USA
1998 – 2000	Katharinen-Gymnasium, Ingolstadt
Juni 2000	Abitur, Allgemeine Hochschulreife

## Hochschulausbildung

2000 – 2004	Chemie-Studium an der Ludwig-Maximilians-Universität München
2002	Vordiplom in Chemie
2004	Hauptdiplom in Chemie
Dez. 2004 – Juni 2005	Anfertigung der Diplomarbeit bei Prof. R. de Vivie-Riedle
Aug. 2005 – Okt. 2005	Werkstudentin bei Prof. K.-L. Kompa am Max-Planck-Institut für Quantenoptik, Garching
ab Nov. 2005	Doktorarbeit in der Gruppe von Prof. R. de Vivie-Riedle an der Ludwig-Maximilians-Universität München



# Acknowledgments

An dieser Stelle möchte ich mich bei allen bedanken, die zum Gelingen dieser Arbeit auf unterschiedlichste Weise beigetragen haben.

Frau Prof. Dr. Regina de Vivie-Riedle gilt mein Dank für die Aufnahme in Ihren Arbeitskreis und die Unterstützung meiner Arbeit. Durch die interessante Thematik und den wissenschaftlichen Freiraum konnte ich immer neuen Ideen nachgehen und vieles dazulernen. Auch die Möglichkeit an Konferenzen teilzunehmen und meine Arbeit dort vorzustellen hat mein Vorankommen sehr unterstützt.

Durch eine solche Gelegenheit kam auch die Zusammenarbeit mit Prof. Martin Zanni und David Strasfeld zustande. Ihnen möchte ich hier auch danken: thank you, Marty and Dave, for fruitful discussions in Ringberg and Munich. I'm looking forward to your new experimental results.

Allen Mitgliedern unserer Arbeitsgruppe möchte ich danken für die Diskussionsbereitschaft, die gute Zusammenarbeit und die lustige Zeit: Judith, Benni, Markus, Artur & Philipp. Aber auch den ehemaligen Gruppenmitgliedern: Uli, Doro und Brigitte, sowie Patrick, der seine Bachelorarbeit bei mir angefertigt hat, danke ich. Ein ganz großes Dankeschön geht dabei an Judith für die vielen wichtigen und konstruktiven Diskussionen in den letzten Jahren.

Nicht zuletzt danke ich Roy und Marcus für die viele Arbeit, die sie sich mit dem Korrekturlesen des Manuskripts gemacht haben und meiner Familie & meinem Freund für die Unterstützung.